UNIVERSITY OF CALIFORNIA SAN DIEGO

Exchange Across the Stratified Inner-Shelf

A dissertation submitted in partial satisfaction of the
requirements for the degree
Doctor of Philosophy

in

Oceanography

by

Derek Jeffrey Grimes

Committee in charge:

Falk Feddersen, Chair
Sarah N. Giddings
Mark Merrifield
Eugene Pawlak
Kraig Winters

2020

The dissertation of Derek Jeffrey Grimes is approved, and it is acceptable in quality and form for publication on microfilm and electronically:

_____

_____

_____

_____

_____

Chair

University of California San Diego

2020

DEDICATION

To my wife and son who inspire me.

And to my parents who molded me.

EPIGRAPH

When young Dawn with her rose-red fingers shone once more

I set out down the coast of the wide-ranging sea,

–Menelaus (Homer, The Odyssey: Book 4)

TABLE OF CONTENTS

LIST OF FIGURES

ACKNOWLEDGEMENTS

Thank you to my friend and mentor Dr. Falk Feddersen. I value your insight and candor, both have helped me grow and kept me in check. Your many analogies between research, music, and history never fail to assuage my frustrations and make me smile. Your trust and faith in my capabilities help me trust myself. Your willingness to guide me from afar (to a point) allow me to explore broader academic interests. Your emphasis on balanced research, between observations, theory and modeling, make me a more diversified scientist. Thank you!

I also thank my PhD cohort for sharing in this endeavor; my undergraduate advisor Dylan McNamara for guiding me to physical oceanography; Feddersen lab-mates and Guza group field crew; the SIO diving and small boating program; and the SIO administration.

I am forever indebted to my parents, Charles and Deborah Grimes. The love and support that you bestowed on me has undoubtedly made these pursuits possible. Mom, thank you for the countless hours you invested in my childhood and adult education. Dad, thank you for taking me to the shop at way too young an age and teaching me to recognize when to drop the wrench and grab the torch. I love you both so much.

Sunshine, my best friend, thank you for the cuddles. Charlie, my room-mate, I still don't appreciate your 3am romps.

Lastly, I thank my wife, Anna Elizabeth Grimes. You inspired me to fulfill this quest. I doubt it was possible without your support. I promise to be considerate and minimize the at home physics/oceanography lectures. Thank you for loving me. I never thought I could love someone more than you... that is, until you gave birth to Oliver Zephyr, who stole the show.

Chapter 1, in full, is a reprint of the paper Cross-shore Deformation of a Surf-zone Released Dye Plume by Internal Tide on the Inner-shelf in Journal of Physical Oceanography by D. J. Grimes, F. Feddersen, S. N. Giddings and E Pawlak in 2020. The dissertation author was the primary investigator and author of this paper.

Chapter 2, in full, is a reprint of the paper Tracer Exchange Across the Stratified Inner-

Shelf Driven by Transient Rip-Currents and Diurnal Surface Heat Fluxes in Geophysical Research Letters: Oceans by D. J. Grimes, F. Feddersen and N. Kumar in 2020. The dissertation author was the primary investigator and author of this paper.

Chapter 3, in full, is currently being prepared for submission for publication of the material to Journal of Fluid Mechanics by D. J. Grimes and F. Feddersen. The dissertation author was the primary investigator and author of this paper.

VITA

2014-2020	Graduate Student in Physical Oceanography, SIO, UCSD
2014	Bachelor of Science in Physics *summa cum laude*, University of North Carolina at Wilminton

PUBLICATIONS

Grimes, D. J., Feddersen, F., The self-similar stratified inner-shelf response to transient rip-current induced mixing. In Preparation for *Journal of Fluid Mechanics*.

Grimes, D. J., Feddersen, F., Kumar, N., 2020: Tracer Exchange Across the Stratified Inner-Shelf Driven by Transient Rip-Currents and Diurnal Surface Heat Fluxes. Geophysical Research Letters: Oceans, **47**(10), https://doi.org/10.1029/2019GL086501

Grimes, D. J., Feddersen, F., Giddings, S. N., Pawlak, E., 2020: Cross-shore Deformation of a Surf-zone Released Dye Plume by Internal Tide on the Inner-shelf. Journal of Physical Oceanography, **50**,35-54, https://doi.org/10.1175/JPO-D-19-0046.1

Grimes, D. J., Cortale, N., Baker, K., and McNamara, D. E., 2015: Nonlinear forecasting of intertidal shoreface evolution. Chaos: An Interdisciplinary Journal of Nonlinear Science, **25**, hppts://doi.org/10.1063/1.4931801.

ABSTRACT OF THE DISSERTATION

Exchange Across the Stratified Inner-Shelf

by

Derek Jeffrey Grimes

Doctor of Philosophy in Oceanography

University of California San Diego, 2020

Falk Feddersen, Chair

Tracer Exchange across the inner-shelf is critical in nutrient cycling and larval recruitment, and coastal water quality. Many processes contribute to inner-shelf exchange *e.g.,* rip-currents, internal bores, tides, and winds, with varying time scales from minutes to weeks and alongshore length scales from 100 m to 10 km, but in many conditions a single mechanism dominates and all are affected by stratification. Here, a sub-set of exchange mechanisms are studied using field observations of a surf-zone released tracer on the stratified inner-shelf and a series of idealized coupled surf-zone and stratified inner-shelf model simulations.

The cross-shore deformation of an inner-shelf (IS) dye plume that formed following a 3.84 h early morning surfzone (SZ) dye release off of Imperial Beach, CA is analyzed with in situ

and aerial remotely-sensed observations. After 5 h, the inner-shelf plume was surface intensified, extending to 800 m from shore. Over the next $\approx$ 2 h, the IS-plume deformed (narrowed) cross-shore, deepened, and elongated alongshore. Offshore tracer transport and subsequent IS-plume deformation and deepening is related to advection by two phases of the diurnal internal tide (DIT).

Exchange between SZ and IS is predominately due to rip-currents, strong concentrated offshore flows. On alongshore uniform coasts, directionally spread swell generate transient rip-currents (TRC), that are episodic without preferred formation site. Diurnal heating and cooling can also induce thermally driven exchange. A series of idealized simulations with TRC and diurnal surface heat flux (SHF) forcing (separately and combined) are used to evaluate the relative strength of these two mechanism. Based on multiple exchange definitions, the TRC mechanism is similar with and without SHF, and is dominant out to 1 km offshore, relative to SHF only or thermally driven exchange. Additional idealized simulations with only TRC-forcing and uniform initial thermal stratification $\mathrm{d}T_0/\mathrm{d}z$ [$^\circ\mathrm{C\,m^{-1}}$] (or N_0^2) varying from 0 (unstratified) to 0.75 $^\circ\mathrm{C\,m^{-1}}$ (highly stratified) indicate the inner-shelf response is self-similar and related to mixing modification of background potential energy.

Chapter 1

Cross-shore Deformation of a Surfzone Released Dye Plume by an Internal Tide on the Inner-shelf

Abstract

An inner-shelf (IS) dye plume that formed following a 3.84 h early morning surfzone (SZ) dye release off of Imperial Beach, CA is analyzed with in situ and aerial remotely-sensed observations. Mid morning, 5 h after release start, the IS-plume extended 800 m offshore (or $\approx 8L_{sz}$, where L_{sz} is the surfzone width) and was surface intensified. Over the next ≈ 2 h, the IS-plume deformed (narrowed) cross-shore with the offshore front progressing onshore at $\approx 5\ \mathrm{cm\,s^{-1}}$, deepened by up to 3 m, and elongated alongshore at $\approx 4.5\ \mathrm{cm\,s^{-1}\,km^{-1}}$ (at $\approx 2.5L_{sz}$). Coincident with IS-plume deformation and deepening, IS isotherms also deepened, with relatively stable IS-plume joint dye and temperature statistics. Offshore tracer transport and subsequent IS-plume deformation and deepening likely resulted from two phases of the diurnal internal tide (DIT). During and after deformation, the IS-plume did not re-enter the warm surfzone, which

potentially acted as a thermal barrier. High-frequency internal waves (HF IW) propagated through the IS-plume at $\approx 9\ \mathrm{cm\,s^{-1}}$ and dissipated onshore of $4L_{\mathrm{sz}}$. Surface HF IW signal was elevated in the plume elongation region, suggesting a linkage between plume elongation and either the DIT or HF IW. This IS-plume evolution differs from previous SZ tracer releases, highlighting the effects of release timing relative to the solar cycle or the internal tide.

1.1 Introduction

The cross-shore exchange of tracers across the surfzone (SZ, region of depth limited surface gravity wave breaking) and the inner-shelf (IS, region offshore of surfzone to ≈ 15 m water depth) is integral to coastal human and ecosystem health (*e.g.,* Barbier et al., 2011). For example, the transfer of human pathogens across the SZ onto the IS dilutes SZ concentrations and improves degraded coastal water quality (*e.g.,* Grant et al., 2005). Shoreward larval transport from the shelf to inner-SZ intertidal recruitment sites is critical to coastal ecosystems (*e.g.,* Pineda et al., 2007). Broadly, many different mechanisms are known to contribute to cross-shore exchange of tracers, *i.e.,* across either SZ, IS, or both (*e.g.,* Morgan et al., 2018; Washburn and McPhee-Shaw, 2013; Lentz and Fewings, 2012). However, the interaction and combination of both SZ and IS processes across a range of timescales (such as, rip-currents and internal waves and tides) and their effect on cross-shore tracer exchange is poorly understood.

SZ tracer dispersion is predominantly driven by breaking surface gravity waves. Dissipation of surface gravity waves supplies turbulence (*e.g.,* Feddersen, 2012), vertically mixing both temperature and tracers (*e.g.,* Hally-Rosendahl et al., 2014). Breaking waves also drive SZ alongshore currents (*e.g.,* Longuet-Higgins, 1970a,b) and vertical vorticity (Clark et al., 2012). For alongshore uniform nearshore morphologies (Feddersen and Guza, 2003), tracer exchange does not generally depend on the alongshore location of tracer release, but may be sensitive to the release time. Alongshore uniform cross-SZ tracer dispersion is attributed to SZ vertical

eddy vorticity (Clark et al., 2010). In contrast, for alongshore variable rip-channeled SZs, short timescale (< 90 s) drifter dispersion is attributed to the strong shear in bathymetrically controlled rip currents (Brown et al., 2009).

SZ processes also drive exchange with and across the IS. For example, SZ eddies coalesce to form transient rip-currents (TRC), ephemeral offshore directed flows that eject SZ water onto the IS (*e.g.,* Johnson and Pattiaratchi, 2004), and have been identified as irregular-alongshore dye patches on the IS following a late-morning SZ dye release (Hally-Rosendahl et al., 2014). TRCs brought SZ released dye out to $2L_{sz}$-$3L_{sz}$ (where L_{sz} is the width of the SZ) offshore in about 5 h (Hally-Rosendahl et al., 2015). In barotropic models, TRC driven exchange can be significantly larger than Stokes drift exchange up to several SZ widths from shore, and depends critically on incident wave directional spread (Suanda and Feddersen, 2015). On the stratified IS, TRCs can enhance vertical mixing, generating a baroclinic cross-shore circulation (Kumar and Feddersen, 2017b) that induces a subsurface cross-shore tracer exchange pathway out to $6L_{sz}$-$8L_{sz}$ over 12 h (Kumar and Feddersen, 2017c). On rip-channeled beaches, bathymetrically controlled rip currents can circulate water between the SZ and IS, in some cases with little net cross-shore exchange due to recirculation (*e.g.,* Brown et al., 2015).

In addition to SZ generated TRCs, other processes–spanning a large range of time and space scales–contribute to cross-shore exchange on an alongshore uniform IS (*e.g.,* Lentz and Fewings, 2012). On relatively long subtidal (> 33 h) timescales, alongshore upwelling (downwelling) winds can drive cross-shelf circulation on the mid to outer shelf (*e.g.,* Smith, 1981). On the shallow IS, cross-shore circulation is weaker and may shut down under unstratified conditions, potentially blocking IS tracer exchange (Lentz, 2001; Austin and Lentz, 2002). Cross-shore winds also contribute to cross-shelf circulation with response dependent on initial vertical and cross-shore stratification (Horwitz and Lentz, 2014).

On the mid-shelf, semi-diurnal and diurnal tidal-band internal waves have been inferred to induce cross-shelf nutrient fluxes (Lucas et al., 2011). On the shallow IS, internal waves can

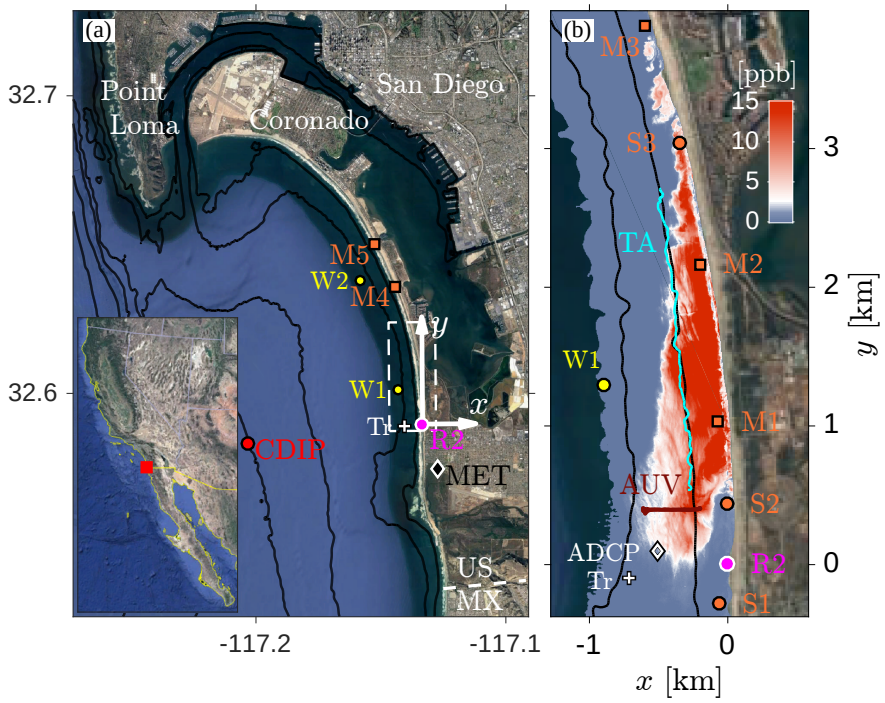

Figure 1.1: (a) Map of San Diego Bight study region, with inset to illustrate location of experiment with respect to the California (US)–Baja California (MX) coast. The dye release location R2 (magenta circle), the local (x,y) coordinate axes with lengths of $(2,4)$ km in white, and white dashed line shows perimeter of panel (b). Indicated are the locations of offshore fixed instrumentation: two wire-walkers (W1 & W2), thermistor mooring (Tr), Coastal Data Information Program (CDIP) wave buoy, and TRNERR meteorological (MET) station. Also shown in (a) are SZ instruments M4 & M5 (orange), north of panel (b). Bathymetry is derived from the 2012 NOAA tsunami DEM and $h = [6, 12, 24, 36, \dots]$ m are contoured in black. (b) Map of surface dye field at 10:20 PDT on Oct. 08, 2015 contoured in parts-per-billion, along with the locations of IS current meter (ADCP), and SZ instrumentation (M1-M3 & S1-S3). Also shown in (b) are the raw trajectories of the towed array (TA) and autonomous-underwater vehicle (AUV) transects.

drive considerable temperature fluctuations, even at $h = 5$ m depth (Winant, 1974), and induce exchange (Pineda, 1999). Near-bed cold bores with timescales 1-4 h have been observed to propagate upslope from 8 m to 2 m depth (outer SZ limit) in a manner consistent with an upslope gravity current (Sinnett et al., 2018). High-frequency internal waves (HF IW, periods ≤ 1 h) in the form of solitary-like waves are often associated with these bores (*e.g.,* Walter et al., 2012; Klymak and Moum, 2003). Instability of large amplitude internal tides (IT) can generate smaller scale (and higher-frequency) IWs (*e.g.,* Holloway et al., 1999) that can contribute to cross-shelf

mass flux (*e.g.,* Lamb, 1997; Shroyer et al., 2010; Zhang et al., 2015). Thus, internal waves at tidal and HF timescales may contribute to exchange across the IS and potentially even across the SZ.

Cross-shore buoyancy gradients can also influence IS exchange. For instance, nearshore diurnal heating and cooling drives exchange (*e.g.,* Monismith et al., 1990; Farrow and Patterson, 1993), with potential to flush the SZ-IS region in roughly a day (Molina et al., 2014). Vertical shear in alongshore flows can also result in Coriolis-driven cross-shore exchange (Ulloa et al., 2018). Alternatively, a strong SZ/IS temperature difference (*e.g.,* mid-day warmer SZ and colder IS, Hally-Rosendahl et al., 2014) may prevent IW propagation into very shallow water (*i.e.,* < 4 m depth, *e.g.,* Omand et al., 2011).

Several previous SZ dye releases observed cross-shore tracer dispersal onto the IS to $2L_{\mathrm{SZ}}$-$3L_{\mathrm{SZ}}$ over 2-5 h (*e.g.,* Grant et al., 2005; Hally-Rosendahl et al., 2014, 2015). However, the mechanism for exchanging tracer farther offshore is not clear and likely involves IS processes across a range of spatiotemporal scales (*e.g.,* HF IW and IT, and diurnal thermal exchange). Furthermore, because these previous SZ dye releases were all mid- to late-morning in either May or September in Southern California (with strong solar heating), the effect of release timing on the cross-shore exchange is not clear. Previous IS tracer release experiments in $6 < h < 12$ m depth have focused on testing relative dispersion scalings (*e.g.,* Stacey et al., 2000; Fong and Stacey, 2003; Jones et al., 2008) and underlying mechanisms, like shear-dispersion (*e.g.,* Sundermeyer and Ledwell, 2001; Moniz et al., 2014).

Under realistic conditions, a combination of IS processes with a range of spatiotemporal scales are likely to contribute to IS tracer exchange, which can make field observations difficult to contextualize. For example, large-scale stratification changes during tracer observations (*e.g.,* Fong and Stacey, 2003) can bias dispersion statistics. Even for nearly stationary conditions, the number of independent realizations often is logistically limited, precluding statistical treatment. Additionally, limited observations can make it difficult to attribute the observed tracer evolution

to physical processes (*e.g.,* Sundermeyer and Ledwell, 2001). Observations of tracer evolution spanning the range of scales (*e.g.,* TRCs to HF IW to IT) are necessary to understand how SZ released tracer is exchanged across the IS.

As part of the Cross–Surfzone/Inner-shelf Dye Exchange (CSIDE) experiment (Imperial Beach, California, Fig. 1.1a), the evolution of an early morning, SZ released tracer is observed on the IS over $\approx$ 10 h and $\approx$ 10 km alongshore where tracer plume width varied from 500-800 m (or $5L_{sz}$-$8L_{sz}$) cross-shore. Dye, temperature, and current observations, as well as averaging methodologies are described in Section 1.2. In Section 1.3, novel IS-plume observations from aerial remote and *in situ* observations are presented. The effect of the internal tide, HF IW, and solar heating on the evolution of the IS tracer plume as well as the potential effect of shoreline tracer release timing relative to internal tide phase and solar cycle are discussed in Section 1.4. The results are summarized in Section 1.5.

1.2 Methods

The CSIDE study consisted of three dye tracer releases, conducted in the southern San Diego Bight near the city of Imperial Beach (IB), California (Fig. 1.1) in fall of 2015. Herein we report on IS observations spanning approximately 11.5 h following the start of the second release (R2) on 8 October 2015. The San Diego Bight region includes San Diego Bay and is bounded by the United States/Mexico border and Tijuana River Estuary to the south, and Point Loma to the north and west, and includes the cities of IB and Coronado. A broad shoal offshore of the estuary focuses incoming swell (see the 6 and 12 m depth contour in Fig. 1.1a) resulting in locally complex wave transformation patterns. Between IB and Coronado is a 9 km isthmus that includes Silver Strand State Beach where the 6 and 12 meter depth contours are approximately parallel to shore. The coastline curves more rapidly near Coronado before terminating at the N/S oriented San Diego Bay Inlet. The local right-handed coordinate system originates at the location of the

second release, R2 in Fig. 1.1a-b, with positive x increasing on-shore and oriented approximately true-east, y oriented along-coast at the origin and toward north, and vertical coordinate z is up relative to mean-sea-level. In addition, a local, shoreline referenced shore-normal coordinate is given by $\tilde{x}$, and $\tilde{z}$ is used to denote vertical measurements relative to the tidally varying sea-surface η.

1.2.1 Moored and Fixed Instrumentation

Fixed instruments were deployed in the study region for approximately one month (15 Sept.–15 Oct. 2015) to provide regional scale physical oceanographic conditions (see Fig. 1.1a). Three moorings provided water column temperature measurements. The southern-most mooring (Tr in Fig. 1.1) was located approximately on the $h = 12$ m isobath and consisted of 6 Sea-Bird 56 thermistors sampling at 0.5 Hz with vertical spacing $\Delta z = 1.5$ m beginning at $z = -2.6$ m below mean-sea-level (MSL). A 1.2 MHz RD Instruments 4-beam acoustic Doppler current profiler (ADCP in Fig. 1.1b) was deployed adjacent to mooring Tr ($\Delta x = 202$ m, $\Delta y = 195$ m) on roughly the 11 m isobath. The ADCP sampled during daytime from 08:00-16:00 PDT with a sample rate of 1 Hz and vertical resolution of 0.5 m. Farther north, two Wirewalker wave powered profilers (Rainville and Pinkel, 2001) outfitted with Sea-Bird-49 conductivity-temperature-depth (CTD) sensors and Wetlab ECO-Triplet fluorometers (W1 & W2 in Fig. 1.1a) were deployed on the $h = 13$ & 14 m bathymetry contour, respectively. These Wirewalkers sampled roughly the upper two-thirds of the water column and under typical conditions repeat profiles took ≈ 90 s. Moorings W1 and W2 were located about 1.4 km and 5.7 km from Tr, respectively with W1 and W2 separated by 4.3 km. Wave data was provided by Coastal Data Information Program (CDIP) IB West buoy number 218 (CDIP in Fig. 1.1a). Wind speed and direction was provided by the Tijuana River Estuary National Research Reserve meteorological station (denoted MET in Fig. 1.1a). Additional instrumentation was deployed offshore and inside the Tijuana River Estuary that are not used in this analysis.

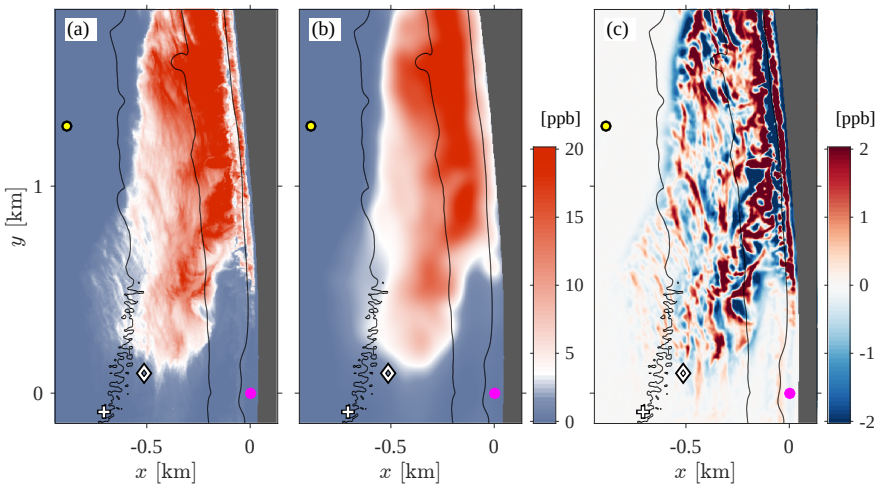

Figure 1.2: Example of spatial filter applied to the IS surface dye field at 1020 h ($t_r = 5.02$ h): (a) surface dye concentration $D(x,y)$ from calibrated MASS hyperspectral imagery; (b) large-scale dye field $\bar{D}$ with cut-off of 150 m; (c) small-scale dye field D' versus x and y. The same color scale (0-12 ppb) is used in (a)-(b), and in (c) the scale is ± 2 ppb. In (a)-(c) gray is land, and black bathymetry contours are $h = [2, 6, 12]$ m, magenta is the release location, and the location of ADCP ($\diamond$) and IS moorings Tr (+) and W1 (yellow) are also indicated.

1.2.2 Surfzone Dye Release

The R2 release period started at 05:18 PDT (hereafter time of day is presented as 0518 h, and time since release start t_r is given in decimal hours) on 8 October 2015 and lasted approximately 3.84 h. A total of 113.6 L of 21.49% Rhodamine WT fluorescent dye solution was pumped via a medical-grade peristaltic pump at a rate of ≈ 0.5 L min^{-1} into the SZ at a fixed cross-shore position where the depth varied from roughly 0.25 m to 0.75 m with the incoming tide over the release duration. Dye release location temperature was measured with a Sea-Bird-56 thermistor at 1 Hz. The release was chosen to coincide with incident south swell (*i.e.,* driving SZ currents to north) and the incoming phase of the surface tide (*i.e.,* during positive along-shore tidal velocity) to maximize the potential for northward transport.

1.2.3 Mobile Instrumentation

Mobile observation began after the start of the dye release with SZ, *in situ* IS, and aerial remote-sensed platforms (symbols and lines in Fig. 1.1b). SZ dye and temperature were measured at 1 Hz for 48 h after release start with Wetlab ECO-Triplet fluorometer + temperature sensors mounted to poles (S1-S3, Fig. 1.1b) and with co-located ECO-Triplet fluorometers + Sea-Bird-39 thermistors mounted to anchored mobile carts (M1-M5, Fig. 1.1). These platforms were deployed mid-SZ. The pole-mounted instruments were not moved once deployed, whereas the carts were moved cross-shore with the tide to maintain roughly mid-SZ position.

In situ IS sampling consisted of vessel towed array (TA) and autonomous-underwater-vehicle (AUV) transects (TA and AUV in Fig. 1.1b). The TA had 5 Wetlab ECO-Triplet fluorometer + temperature sensors sampling at 1-6 m below the surface with a vertical spacing between 1-2 m. The 2.5 km-long south-north TA transect (cyan and TA in Fig. 1.1b) was surveyed at approximately 0.6 $\mathrm{m\,s^{-1}}$ from 1107 h to 1210 h ($t_\mathrm{r} = 5.80$-6.85 h). The AUV was a REMUS-100 (Hydroid Inc.) equipped with a Sea-Bird-49 CTD and Wetlabs ECO-Puck fluorometer. The AUV drove repeated 500-m long cross-shore and vertical transects (red line and AUV in Fig. 1.1b) between 0900-1200 h ($t_\mathrm{r} = 3.69$-6.69 h). Two repeat cross-shore surveys, taking on average ≤ 20 min, were used to generate (x,z) dye and temperature maps. A jet-ski sampled near-surface (20 cm) dye and temperature in a mow-the-lawn pattern (not shown) that was used to calibrate aerial hyperspectral measurements.

Aerial remote sensing with the Modular Aerial Sampling System (MASS, Melville et al., 2016) was used to estimate georeferenced surface dye concentration and relative temperature. The dye plume was imaged 53 times between $1020-1658$ h ($t_\mathrm{r} = 5.02$-11.65 h). Photo-mosaic relative sea surface temperature was measured with an infrared camera (8.0-9.2 μm wavelength band). Push-broom hyperspectral imagery spanning wavelengths of $400-990$ nm in 126 bands was used to estimate surface dye concentration. The raw hyperspectral data has a cross-track resolution of roughly 1.25 m (depending on altitude) and was interpolated to a regular 2×2 m grid

(likewise for temperature). The hyperspectral imagery is converted to surface dye concentrations $D(x,y)$ (Fig. 1.2a), following Clark et al. (2014) by calibrating to coextensive *in situ* near-surface jet-ski dye measurements (not shown). IS remote hyperspectral dye measurements are likely sensitive to dye vertical structure, therefore this calibration ensures MASS dye estimates are representative of the near-surface ($\tilde{z} \approx -20$ cm) dye concentration.

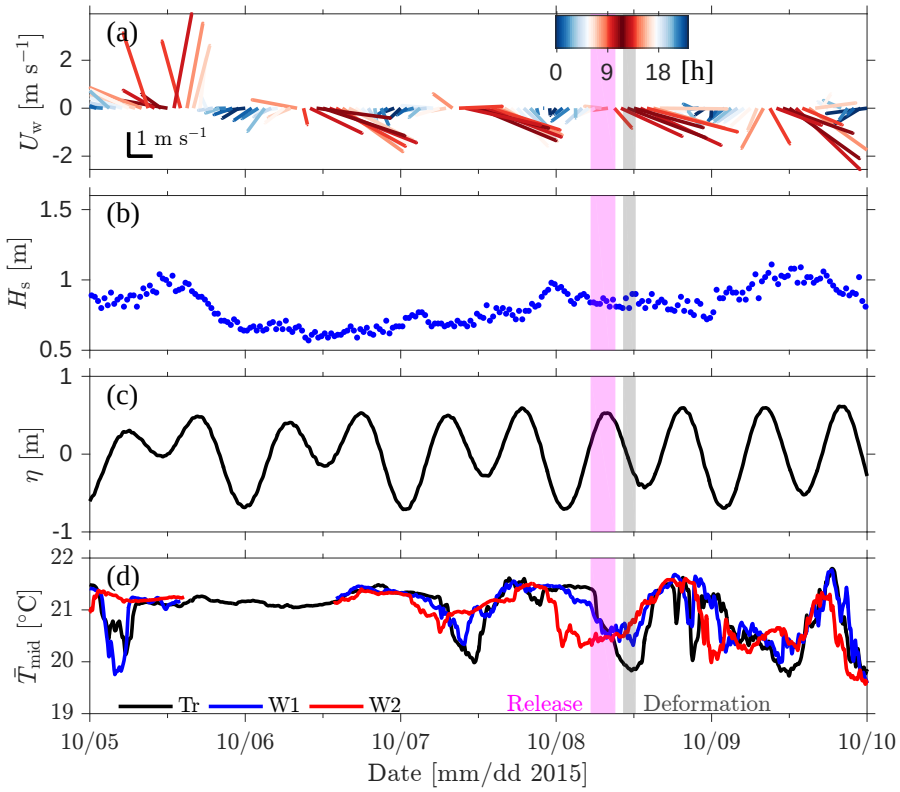

Figure 1.3: Five-day time-series of CSIDE experiment conditions: (a) TRNERR MET station wind vectors (see Fig. 1.1) where the line color represents the hour of day; (b) significant wave height (H_s) from CDIP buoy; (c) sea-surface elevation (η) from ADCP pressure record; (d) band-passed mid-depth temperature $\bar{T}_{mid}$ evolution at Tr (black), W1 (blue), and W2 (red). The time-period spanning the release R2 is denoted with a magenta bar, and the IS plume deformation period with the gray bar.

1.2.4 Definition of Scales and Filtering

The dye and temperature fields varied over a broad range of horizontal length (meters to kilometers) and time (minutes to days) scales, owing to the various processes across the SZ and IS.

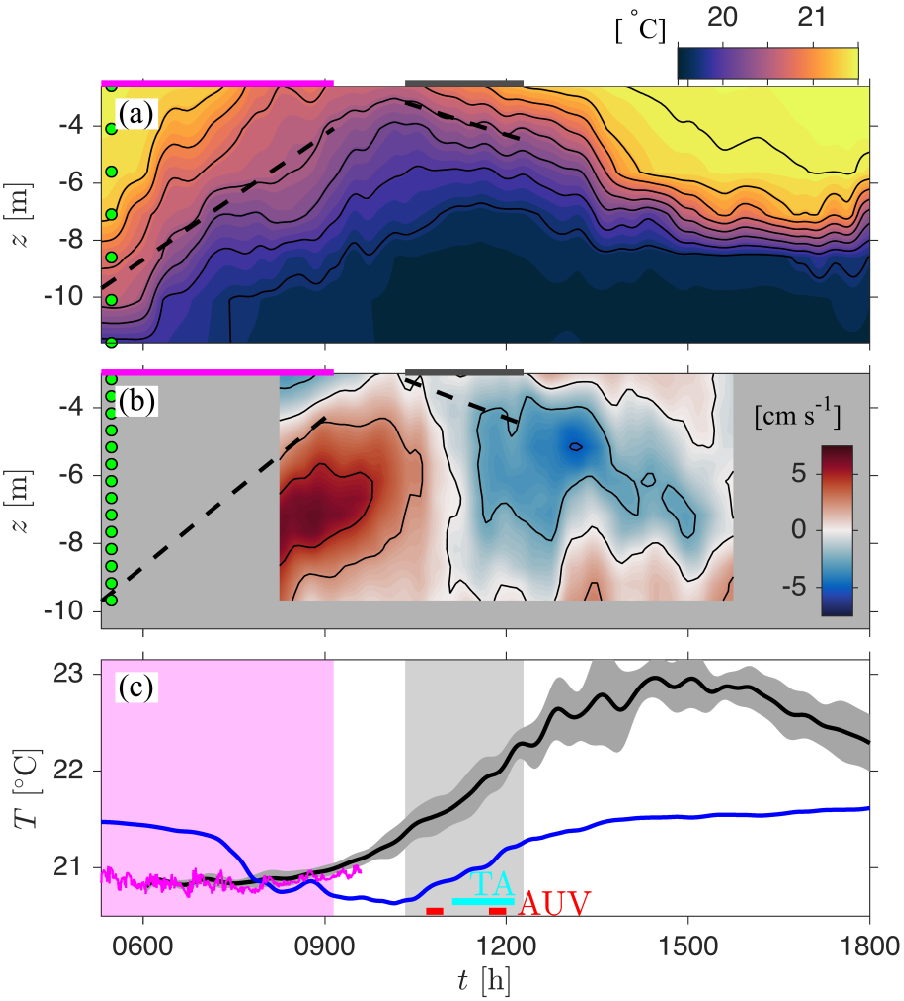

Figure 1.4: Large-scale (a) temperature $\bar{T}$ at mooring Tr (white cross in Figs. 1.1, 1.2-1.6) with contours at 0.25 °C intervals, and (b) cross-shore velocity $\bar{u}$ at ADCP (white diamond in Figs. 1.1 and 1.6) adjacent to Tr, with contours at 2.5 cm s^{-1} intervals. In (a)-(b) green dots indicate approximate instrument sample depths, and the dashed black lines are average $\bar{T} = 20.5$ °C isotherm slopes of 1.5 m h^{-1} and -0.7 m h^{-1} during the release (magenta bar, top) and deformation (gray bar, top) periods, respectively. (c) Raw temperature versus time at the release location (magenta), with low pass-filtered upper Tr thermistor ($z = -2.6$ m, blue); and temperature derived from the large-scale filtered and alongshore average SZ instruments (black curve) $\pm$ the 30 min running rms deviation from the mean (gray shading). In (c) the AUV (red) and TA (cyan) transect times are indicated by horizontal bars.

The range of length scales is seen in the high spatial resolution aerial surface dye measurements (*e.g.,* Fig. 1.2a). Similarly, moored temperature observations vary at a range of timescales, from diurnal and semi-diurnal to periods of approximately 10 min. In the analyses of Section 1.3, dye and temperature fields are decomposed into large- and small-scale fields, denoted by $(\bar{D}, \bar{T})$ and

(D', T'), respectively, using a spatial filter with cut-off of approximately 150 m, and results are presented separately to highlight the dominant processes influencing the dye plume at each scale.

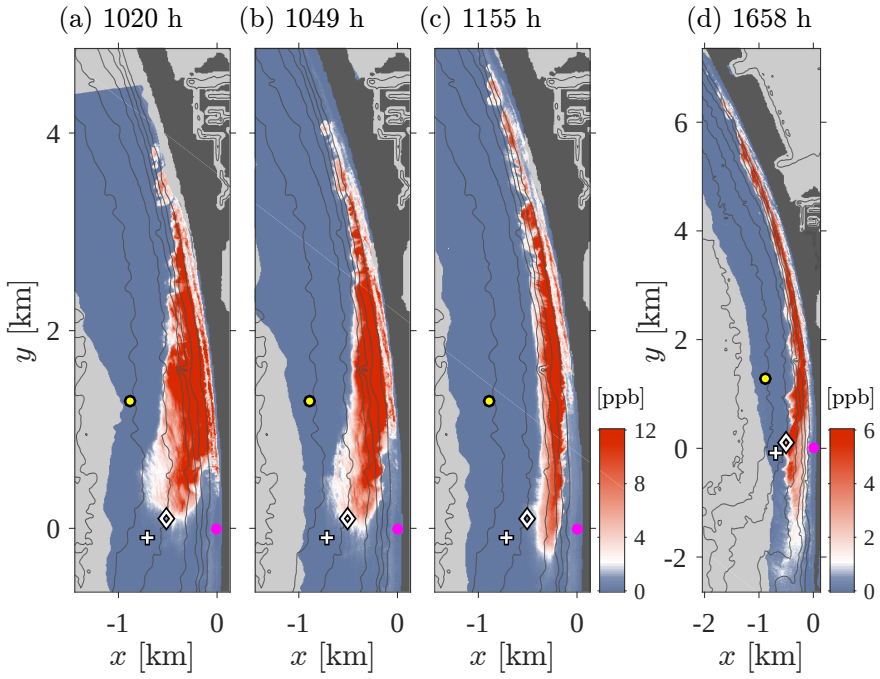

Figure 1.5: Surface dye concentration D versus horizontal coordinates (x,y) during (a)-(c) deformation period; and (d) $\approx$ 12 h after dye release began. Time is indicated above each panel in hhmm relative to Pacific Daylight Time (PDT $\rightarrow$ h), corresponding to $t_r = [5.02, 5.50, 6.60, 11.65]$ h, respectively. Note the difference in scales in panel (d). Release location (magenta dot), IS temperature mooring Tr (+), current meter ADCP ($\diamond$), and wire-walker W1 (yellow) are indicated. Land is dark gray, oceanic regions without data are light gray, and bathymetry contours (black) are drawn at 2 m intervals below mean sea-level.

For a particular observation source, dye and temperature were filtered with the same method. Aerial dye $D(x,y)$ and temperature $T(x,y)$ imagery were convolved with a two-dimensional 150 m $\times$ 150 m Hamming window. The AUV $D(x,z)$ & $T(x,z)$ transects were objectively mapped using horizontal and vertical decorrelation scales of 150 m and 2 m, respectively. The TA $D(y,z)$ & $T(y,z)$ transect was smoothed via convolution with a Hamming window in the time-domain equivalent to an average along-track length scale of approximately 150 m (*i.e.,* 4 min underway at 0.6 m s^{-1}). Mooring $T(t,z)$ and current meter cross-shore velocity $u(t,z)$ were convolved with a 30 min wide Hamming window. Results were not sensitive to the

windowing function.

The linkage between the 150 m spatial scale filter cut-off and the 30 min time domain filter cut-off is based on the shallow water and flat bottom, mode–1 linear internal wave (IW) dispersion relationship,

$$\omega = k\frac{Nh}{\pi}, \tag{1.1}$$

where $N = (-g\rho_o^{-1}\partial\rho/\partial z)^{1/2}$ is the buoyancy frequency, h the local water depth, k is the local wavenumber and ω the frequency of the IW. The vertical temperature time-series at Tr ($h = 12$ m) was used to compute $N(t,z)$, using a constant salinity of 33.4 PSU, resulting in the depth and time (0800–1300 h) averaged $N = 2.3 \times 10^{-2}$ rad s^{-1}, or $2\pi/N = 4.5$ min. Thus, an IW with a wavelength of 150 m has a period of approximately 30 min. By applying a constant 150 m scale spatial filter both HF IWs (periods 4.5–30 min) and TRCs were classified as small scale.

An example surface dye decomposition into large and small scales is shown in Fig. 1.2. The large-scale (*i.e.,* $>$ 150 m) dye field $\bar{D}(x,y)$ (Fig. 1.2b) captures the boundaries and the peak concentration of the plume. Small-scale ($<$ 150 m) dye field $D'(x,y)$ (Fig. 1.2c) variations are roughly ± 2 ppb, with signatures of wave breaking in the SZ, TRCs at the SZ/IS boundary, as well as HF IW-like features on the IS.

1.3 Results

1.3.1 Regional Observations and Dye Release Background Conditions

During the experiment, a diurnal sea-breeze was typical with onshore wind speeds of 5 m s^{-1}, peaking in the afternoon, along with a slight northerly mean of approximately 0.5 m s^{-1} (Fig. 1.3a). On 4 & 5 October 2015 a storm interrupted this pattern with sustained 8 m s^{-1} southerly winds (Fig. 1.3a) and 5 mm of precipitation (not shown). Atmospheric conditions

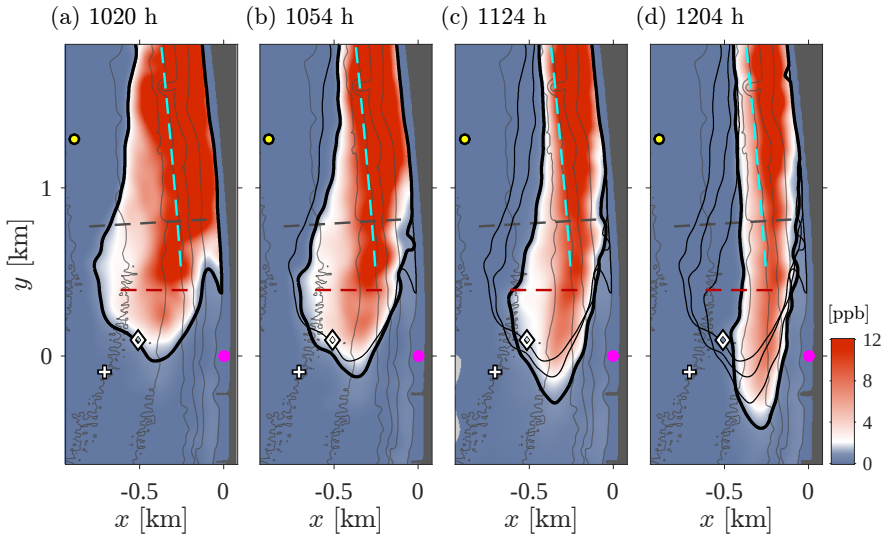

Figure 1.6: (a)-(d) Large-scale IS surface dye $\bar{D}$ evolution during deformation period versus x and y. In each panel time is relative to PDT, corresponding to $t_r = [5.02, 5.59, 6.09, 6.75]$ h, respectively. The 1 ppb contour (thick black) at each time along with all prior contours (thin black) are shown to indicate deformation. The magenta dot $(x, y) = (0, 0)$ is the release location. Also drawn are the average locations of the AUV transect (dashed red line), alongshore TA transect (dashed cyan line), and the gray dashed line is the MASS transect. Dark gray indicates land and the bathymetry is contoured at 2 m intervals below mean sea-level.

returned to normal by 6 October. On 8 October (first day of R2), the CDIP buoy average significant wave height was 0.84 m (Fig. 1.3b), with peak period $\approx$ 14.3 s and peak direction $\approx$ 226 deg true (*i.e.,* from SW and driving northward SZ currents). The maximum tidal range in the San Diego Bight is roughly 2 m. During R2, the tidal range was 1.4 m with a semi-diurnal inequality of approximately 20 cm (Fig. 1.3c).

The mid-depth IS temperature variability had a prominent diurnal internal tidal (DIT) signature (Fig. 1.3d) that was modulated sub-tidally. Over the 1 month, the diurnal mid-depth temperature fluctuations (Fig. 1.3d) were coherent at a level of ≈ 0.8 between the three alongshore temperature moorings (*i.e.,* Tr, W1, and W2), with a north-to-south phase propagation of approximately 40 $\mathrm{cm\,s^{-1}}$ (see Fig. 1.3d). The IS stratification (not shown) was dominated by the vertical temperature gradient, where the average temperature difference was 2.1 °C over a vertical distance of 7.5 m (not shown). During R2, the mid-depth temperature varied by 1.5 °C,

and the dye release (magenta, Fig. 1.3) occurred during the cooling phase of the DIT. Sub-inertial, diurnal internal waves have previously been observed in the Southern California Bight region (*e.g.,* Nam and Send, 2011; Kumar et al., 2016). A diurnal sea-breeze can force diurnal band internal oscillations (*e.g.,* Walter et al., 2017) that are potentially resonant if the effective inertial frequency is decreased due to shear in sub-tidal alongshore currents (*e.g.,* Lerczak et al., 2001).

On the day of R2, the DIT both shoaled and relaxed isotherms at mooring Tr ($h = 12$ m, Fig. 1.4a). Over the release period (magenta bar, top of Fig. 1.4a) the $T = 20.5$ °C isotherm shoaled 5.5 m over 3 h (dashed black line in Fig. 1.4a). Subsequently, the water column warmed, with the $T = 20.5$ °C isotherm deepening about 0.6 m over 2 h (termed deformation period; gray bar, top of Fig. 1.4a). The rapid cooling-then-warming at Tr was associated with a large-scale baroclinic cross-shore velocity observed at ADCP that delivered cold water onshore at depth prior to and during the release period and reversed during the deformation period (Fig. 1.4b). This large-scale temperature fluctuation and velocity signature was observed at all three moorings (Tr, W1, W2). Thermally driven exchange has diurnal temperature and cross-shore flow signals (Molina et al., 2014), however it does not set up an alongshore propagating wave motion (Fig. 1.3d) nor does it have the observed mode-1 structure and phasing (Fig. 1.4b), thus is not a likely mechanism for the observed diurnal signal.

The large-scale (> 30 min) and along-shore averaged SZ temperature, estimated from 9 thermistors spanning 7 km alongshore (R2, S1-S3, and M1-M5 in Fig. 1.1), was dominated by the diurnal heating/cooling cycle (Fig. 1.4c). The SZ root-mean-square (rms) deviations from the alongshore average (gray shading, Fig. 1.4c) were small (< 0.2 °C) prior to the deformation period. During the first half of the release period, the R2 location temperature (T_{rel}, magenta in Fig. 1.4c) was on average ≈ 0.5 °C colder than the Tr mooring $z = -2.7$ m thermistor (blue, Fig. 1.4c). This is likely a lower bound for the cross-shore temperature difference between the SZ and Tr , because for a well-mixed SZ with an average depth of 1 m, a thermistor at this z-level for a stably-stratified IS would likely be warmer than that observed at $z = -2.7$ m. By 0800 h, the

SZ was rapidly warming from solar radiation, whereas the IS temperature dropped as the DIT approached its maximum cold phase at approximately 1000 h. Thus, alongshore gradients were weak relative to the 0.5 °C cross-shore difference.

1.3.2 General Tracer Observations

By 1020 h ($t_r = 5.02$ h), the beginning of the deformation period, the dye plume extended approximately 4 km alongshore (Fig. 1.5a). The northern portion of the dye plume ($y > 2.5$ km, denoted SZ-plume) was narrow (< 200 m, or $< 2L_{sz}$) and shoreline attached with northward tracer transport over the day (Fig. 1.5a-c), consistent with SZ currents driven by obliquely incident south-swell (Longuet-Higgins, 1970a,b). In contrast, at the same time the southern portion of the plume ($y < 2$ km, hereafter the IS-plume) was up to 800 m (or $8L_{sz}$) wide, extending into almost $h = 12$ m depth and was shoreline detached to the south ($y < 400$ m). This implies that some transport mechanism brought the SZ released tracer out to $8L_{sz}$ over 3-5 h. Between 1020 h and 1230 h (denoted deformation period, gray bar in Fig. 1.3 and 1.4) tracer in the IS-plume deformed onshore to $5L_{sz}$ and was transported south, while a dye free SZ intrusion advected from the south, further detaching the IS-plume from the shoreline (Fig. 1.5a-c). The northward advection of the SZ-plume and the southward advection of the IS-plume resulted in a 9 km alongshore extent by 1658 h ($t_r = 11.65$ h). At this time (≈ 6.5 h after the deformation period ended), the plume still remained within $8L_{sz}$ from shore at the surface (Fig. 1.5d). Here, we focus on the deformation period evolution of the IS-plume.

1.3.3 Deformation Period Large-Scale Inner-Shelf Plume Evolution

During the deformation period (gray bar in Fig. 1.3), the offshore plume boundary (thick black $\bar{D} = 1$ ppb contour in Fig. 1.6) propagated onshore at up to 5 $\mathrm{cm\,s^{-1}}$, deforming the plume. Concurrently, the IS-plume elongated alongshore with the southern front moving past the release

point at approximately 7 cm s^{-1}. Meanwhile, a dye free region within the SZ moved north at a similar rate, detaching the IS-plume from shore (dark gray in Fig. 1.6).

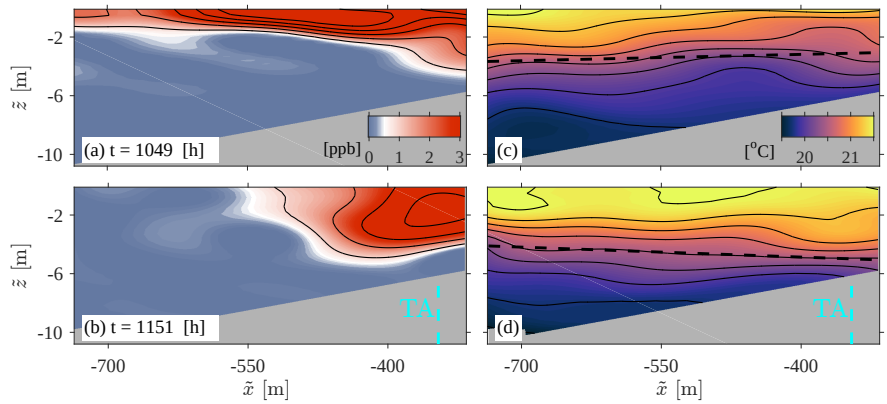

Figure 1.7: AUV transect large-scale (left, (a)-(b)) dye concentration $\bar{D}$ with contours at 1 ppb intervals, and (right, (c)-(d)) temperature $\bar{T}$ with contours at 0.25 °C intervals versus local cross-shore coordinate $\tilde{x}$ and vertical coordinate $\tilde{z}$ at (top, (a) & (c)) $t = 1049$ h ($t_r = 5.50$ h) and (bottom, (b) & (d)) $t = 1151$ h ($t_r = 6.54$ h). The AUV transect line is shown as red dashed line in Fig. 1.6 and each transect took approximately 20 min. In (c) and (d) the dashed lines are the average $T = 20.5$ °C isotherm slopes with values (c) 1.44 m km^{-1} and (d) -2.3 m km^{-1}. The approximate cross-shore location of TA (cyan, Fig. 1.8) is indicated in (b) & (d).

The large-scale vertical and cross-shore structure of the IS temperature and plume deformation can be seen along the AUV transect ($y = 395$, dashed red line in Fig. 1.6). Toward the beginning of the deformation period at 1049 h (first red bar, Fig. 1.4c), the IS-plume was surface trapped ($\tilde{z} \geq -3$ m) and extended offshore of $\tilde{x} = -700$ m (Fig. 1.7a), with isotherms sloping upward toward shore (*e.g.,* $\bar{T} = 20.5$ °C isotherm slope, dashed in Fig. 1.7c). At this time, the SZ temperature was ≈ 21.75 °C, about 0.25 °C greater than the maximum observed AUV temperature, indicating that the isotherm slope changed sign between the SZ and $\tilde{x} = -400$ m (or $\approx 4L_{sz}$). Additionally, the dye plume was largely confined to $T \geq 20.25$ °C, about 0.45 °C below the minimum of T_{rel} (magenta, Fig. 1.4c), indicating mixing with colder water prior to the deformation period.

Consistent with the aerial dye observations (Fig. 1.6), later in the deformation period at 1151 h (second red bar, Fig. 1.4c), the offshore dye front moved onshore to $\tilde{x} \approx -500$ m

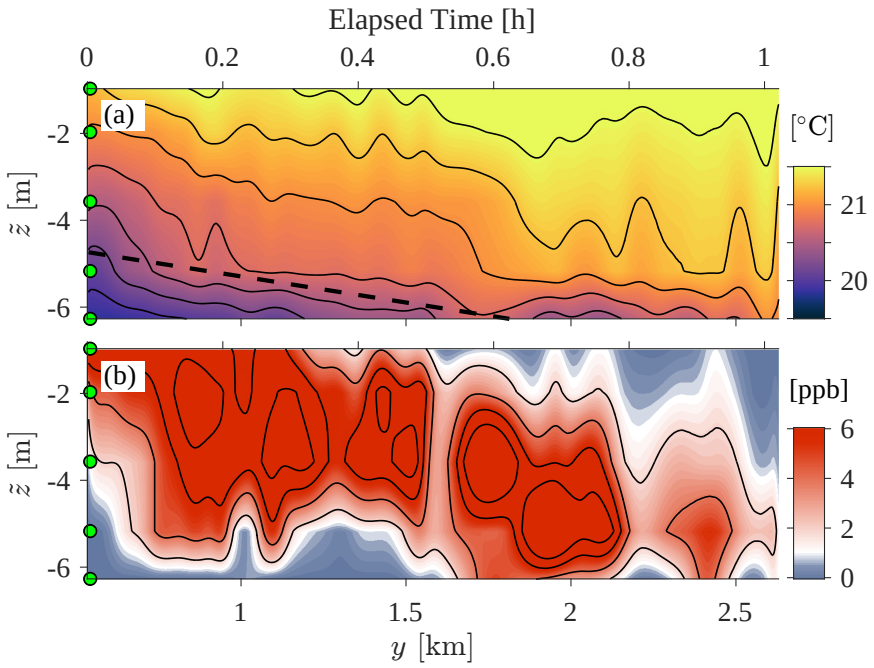

Figure 1.8: TA transect Large-scale (a) temperature $\bar{T}$ with contours at 0.25 °C and (b) dye $\bar{D}$ with contours at 2 ppb versus depth $\tilde{z}$ and alongshore coordinate y. TA transect line is shown in Figs. 1.1a & 1.6. The transect began at $t = 1107$ h ($t_r = 5.80$ h) and the elapsed time is marked on top. Instrument locations are indicated by green circles on left axis, and the black dashed line in (a) is the slope of the $\bar{T} = 20.5$ °C contour, -1.20 m km^{-1} or -2.82 m h^{-1}.

(Fig. 1.7b) and deepened ($\tilde{z} \geq -6$ m). At this time, the AUV $\bar{T} = 20.5$ °C isotherm deepened, consistent with the deepening Tr isotherms (dashed line below gray bar in Fig. 1.4a) and the isotherm slope changed sign (sloping upward offshore). The deepening AUV isotherms and dye plume suggest that the cross-shore plume narrowing was partially balanced by vertical thickening. The observed relaxation of the cross-shore temperature gradient over the deformation period is also consistent with baroclinic flow associated with the DIT (Fig. 1.4b).

Deformation period warming and IS-plume deepening were also observed along TA transect ($\tilde{x} \approx -350$ m and $h \approx 6.5$ m, cyan in Figs. 1.1 and 1.6), which captures both alongshore and temporal variations in the large-scale temperature and dye fields. Between 1107 h and 1208 h (cyan bar, Fig. 1.4c; and $0.54 \lessapprox y \lessapprox 2.7$ km, Fig. 1.8) the TA temperature increased with time (or y) at all depths, with the greatest increase of ≈ 1 °C below $\tilde{z} = -5$ m. The isotherms sloped

downward roughly 1.2 m km^{-1} or 2.82 m h^{-1} relative to space or time, respectively.

The TA dye plume deepened at a rate similar to the isotherms and eventually detached from the surface (Fig. 1.8b). Initially, at $y = 0.54$ km (1107 h) the dye was confined to $\tilde{z} > -4$ m (Fig. 1.8b) and the $\bar{T} = 20.5$ °C isotherm was at roughly $\tilde{z} = -4.5$ m. The dye reached $\tilde{z} = -6$ m by about $y = 0.8$ km (or 1115 h), and by $y = 1.5$ km dye was capped by a warmer $O(21.5$ °C) layer. The dye then remained subsurface as the TA extended north, beyond the IS-plume region (*i.e.,* $y > 2$ km). Similar to AUV, the dye was largely confined to $20.25 \leq \bar{T} \leq 21.5$ °C as both isotherms and iso-dye deepened.

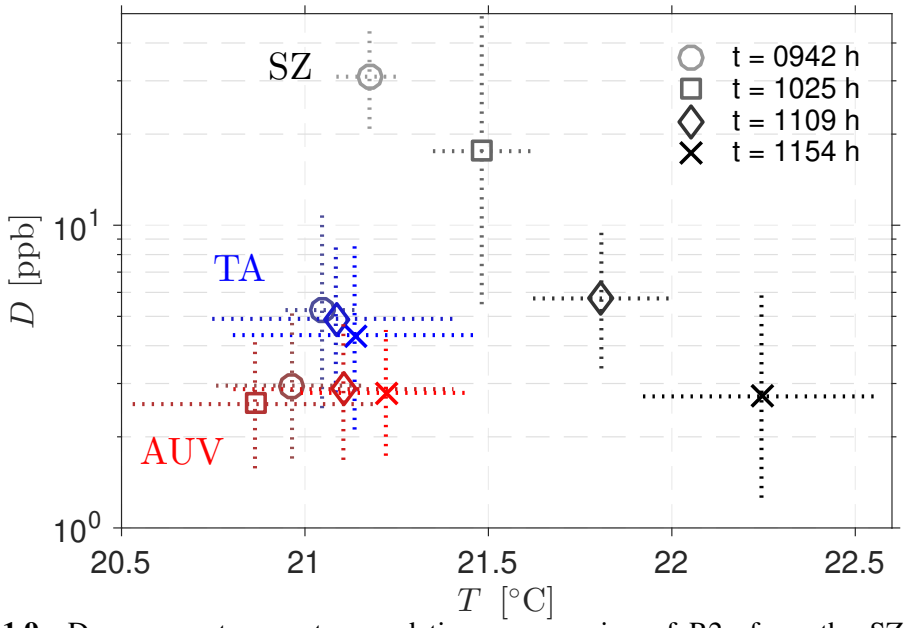

Figure 1.9: Dye versus temperature and time on morning of R2 from the SZ (black), at TA (blue), and AUV (red). Thick markers represent arithmetic mean temperature (*i.e.,* $E[T]$, where $E[]$ is the averaging operator) and logarithmic mean dye (*i.e.,* $\exp(E[\log(D)])$) of observations where $D \geq 1$ ppb, evaluated at approximately 44 min intervals ($t_r = [4.39, 5.10, 5.84, 6.59]$ h), and the dashes represent ± 1 standard-deviation over the same interval. TA and AUV transect data from 0942 h ($t_r = 4.39$ h, red and blue circles) prior the deformation period and before aerial sampling began are included here for comparison with SZ observations.

1.3.4 Release & Deformation Period Statistical Plume Evolution

To examine temporal evolution of joint (D,T) statistics and evaluate the role of mixing in observed IS-plume evolution, arithmetic temperature and logarithmic dye means and standard deviations were calculated over 3-4 approximately 44 min time intervals from all raw (*i.e.,* unfiltered and not interpolated) SZ, AUV, and TA observations where $D \geq 1$ ppb. The average SZ-plume (predominantly from instruments S2-S3 & M1-M4 in Fig. 1.1) temperature increased > 1 °C from 0942–1154 h due to solar heating. The standard deviation of SZ-plume temperature also increased with time from approximately 0.1-0.25 °C (horizontal black dotted lines, Fig. 1.9) due to an increase in SZ temperature anomalies during the deformation period (gray shading, Fig. 1.4c). Meanwhile, average SZ dye concentration decreased by an order of magnitude, with the standard deviation in concentration (vertical black dotted lines, Fig. 1.9) increasing. The large standard deviation in SZ-plume dye concentration at $t = 1025$ h was due to an ≈ 30 ppb concentration difference between instruments M1 & M2 and instruments S2, S3 & M3 (see Fig. 1.1b). The SZ-plume joint dye/temperature evolution indicates a fast response to solar forcing and vigorous lateral mixing.

In contrast, the IS-plume joint dye and temperature statistics were relatively stable in time. The average observed temperature of the IS-dye plume increased slightly (≈ 0.25 °C) during the deformation period (Fig. 1.9), less than half that of the SZ-plume, consistent with a depth dependent response to solar heating. The standard deviation of temperature in the IS-plume (*i.e.,* at both TA and AUV) remained roughly 0.25 °C throughout the deformation. The IS-plume dye concentration was much lower than the SZ and did not decrease considerably over the morning, varying between 2.5–6 ppb, with a standard deviation around 1.8 ppb (red and blue vertical dotted lines in Fig. 1.9). The broader $t = 0942$ h temperature distribution on the IS illustrates that the IS-plume was vertically stratified prior to deformation. The consistent IS-plume temperature span and dye concentration suggests vertical mixing was not responsible for the observed IS-plume deepening during the deformation period.

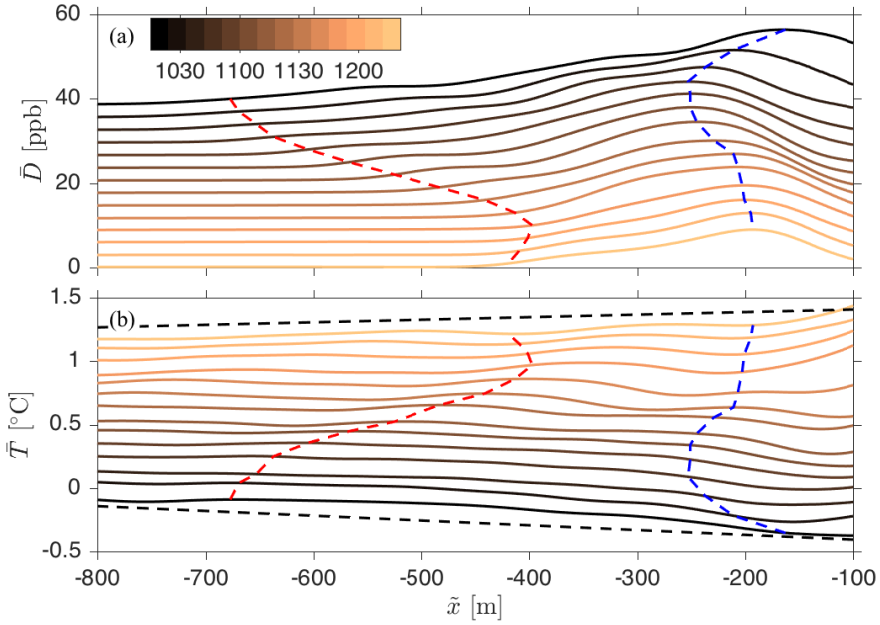

Figure 1.10: Surface (a) dye concentration and (b) relative temperature versus local cross-shore coordinate $\tilde{x}$ at multiple times (see colorbar in (a)) during the deformation period. In (a) the surface dye concentration (measured in parts-per-billion (ppb)) of each curve is offset by -3 ppb (earliest observation is upper-most curve), in (b) the surface temperature is relative to 1 km offshore and each curve is offset by 0.1 °C, in (a)-(b) the red dashed curve is the offshore location of $\bar{D} = 1$ ppb (see black contour in Fig. 1.6) and the blue dashed curve is the location of $\bar{D}_{\max}$. The dashed black lines have $\partial\bar{T}/\partial\tilde{x} = -0.38$ & 0.2 °C km^{-1} between $\tilde{x} = -800$ m and -100 m and correspond to $t = 1020$ h & 1217 h, respectively.

1.3.5 Large-scale Cross-shore Convergence & Alongshore Elongation of Inner-Shelf Plume

The deformation period MASS surface dye and temperature measurements suggest that the IS-plume narrowing and elongation (Fig. 1.6) was largely driven by advection. Here measurements are examined on a cross-shore line at $y = 818$ m within the IS-plume (gray dashed line Fig. 1.6). Prior to deformation at 1020 h, the offshore $\bar{D} = 1$ ppb contour (Fig. 1.6a) was roughly 700 m from shore on the MASS cross-shore line. At this time, there was an IS surface temperature gradient $\partial\bar{T}/\partial\tilde{x}$ (calculated between $\tilde{x} = -800$ and -100 m) of -0.38 °C km^{-1} (*i.e.,* colder onshore, lower black curve, Fig. 1.10b). Between 1020 and 1137 h the $\bar{D} = 1$ ppb front (red dashed line,

Fig. 1.10a) moved on-shore about 275 m, and remained < 500 m offshore until 1217 h (lower yellow curve, Fig. 1.10a). The onshore speed u_f was approximately 5 cm s^{-1} and was estimated as, $u_f = \Delta x_f/\Delta t + v(\delta x_f/\delta y_f)$, where $\Delta x_f/\Delta t$ is the shore-ward progression of the $\bar{D} = 1$ ppb contour along the MASS line and $v(\delta x_f/\delta y_f)$ accounts for the southward advection of the sloped contour where it intersects the MASS line. Meanwhile, the MASS cross-shore temperature gradient continuously increased, switching sign, and reaching approximately 0.2 °C km^{-1} at 1217 h, consistent with the relaxation of shoaled isotherms observed at Tr (Fig. 1.4a) and the reversal of the cross-shore temperature gradient at AUV (Fig. 1.7c-d).

In contrast to the onshore progression of the $\bar{D} = 1$ ppb contour, between 1020 h and 1036 h the cross-shore location of the peak dye concentration $\bar{D}_{\max}$ (blue dashed Fig.1.10a) moved offshore ≈ 100 m to $\tilde{x} \approx -250$ m, as the dye-free intrusion progressed north in the SZ and crossed the MASS transect (see Fig. 1.6a-b). The dye maximum then moved onshore ≈ 60 m at roughly 1 cm s^{-1}. Additionally, the $\bar{D}_{\max}$ decrease in time was relatively small. As such, the average $\partial\bar{D}/\partial\tilde{x}$, calculated as the slope of $\bar{D}(x)$ between $\bar{D} = 1$ ppb and $\bar{D}_{\max}$ (*i.e.,* red and blue curves in Fig. 1.10a), increased from 28 ppb km^{-1} at 1020 h to 66 ppb km^{-1} at 1137 h (not shown). The steepening offshore dye gradient indicates convergent onshore advection (consistent with the DIT) as opposed to a diffusive advancement of the $\bar{D} = 1$ ppb contour, which would require an up-gradient diffusive flux and an inferred negative cross-shore diffusivity between -8 m^2 s^{-1} and -2 m^2 s^{-1}. Thus, shoreward advancement of the $\bar{D} = 1$ ppb contour was largely due to advection.

Coincident with the cross-shore deformation, the IS-plume elongated (strained) in the alongshore direction (Figs. 1.6 & 1.7). This elongation is also evident in the alongshore y evolution of the cross-shore maximum dye concentration $\bar{D}_{\max}(y)$ (Fig. 1.11). At 1020 h (black curve, Fig. 1.11) the southern edge of the IS-plume was just north of the release location ($y = 0$ in Figs. 1.6 & 1.11) and farther to the north there were several prominent ≈ 5 ppb magnitude and ≈ 250 m wide features (*e.g.,* tail of arrows in Fig. 1.11). Between 1020 h and 1217 h the southern

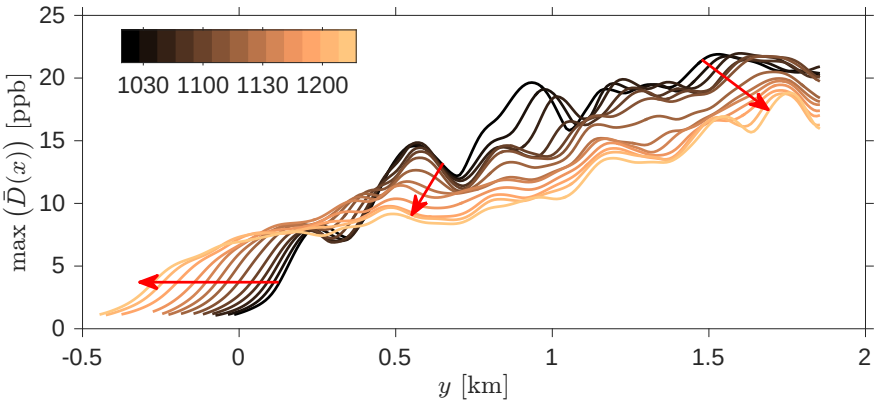

Figure 1.11: Cross-shore maximum of the mean surface dye concentration $\bar{D}$ versus y during the deformation period, where the color of each curve indicates time of observation shown in the legend, red arrows indicate (left-to-right) -6.5, -1.5, and 3 $\mathrm{cm\,s^{-1}}$, illustrating an alongshore plume strain rate of approximately 5 $\mathrm{cm\,s^{-1}\,km^{-1}}$.

dye front advected southward at ≈ 6.5 $\mathrm{cm\,s^{-1}}$, approaching $y = -500$ m (left arrow, Fig. 1.11). Coherent $D_{\max}$ features at $y \leq 750$ m also propagated to the south at ≈ 1.5 $\mathrm{cm\,s^{-1}}$ (middle arrow, Fig. 1.11). At $y \approx 1.5$ km, features advected northward at ≈ 3 $\mathrm{cm\,s^{-1}}$ (right arrow, Fig. 1.11). The differential advection of plume features implies an average alongshore plume straining of 4.5 $\mathrm{cm\,s^{-1}\,km^{-1}}$.

The IS-plume centerline (cross-shore position of $\bar{D}_{\max}$) was tilted slightly from shore parallel south of MASS transect (Fig. 1.6), resulting in some aliasing of cross-shore sheared alongshore transport into observed elongation. The bathymetry also varies slightly alongshore (Fig. 1.6). However, the alongshore elongation apparent in $D_{\max}$ (Fig. 1.11) is also apparent using $\bar{D}$ at a fixed cross-shore distance (*e.g.,* 200-400 m) or along a given bathymetry contour (*e.g.,* 4-8 m), yielding similar strain rates. This suggests that potential aliasing due to cross-shore plume structure was weak. During the deformation period, the IS-plume centerline tilt (relative to the shoreline) south of the MASS transect decreased from 0.15 to 0.05 (not shown) predominantly due to the onshore advection of $\bar{D}_{\max}$, rather than due to the southward propagating front. Combined with the presence of straining between $\bar{D}_{\max}$ features north of MASS transect ($y > 800$ m, Fig 1.11), where the centerline was nearly shore parallel, indicates that the alongshore

plume elongation was not driven by alongshore uniform shear, *i.e.,* $\partial v/\partial x$.

1.3.6 Small-Scale and High-Frequency Inner-Shelf Plume Evolution

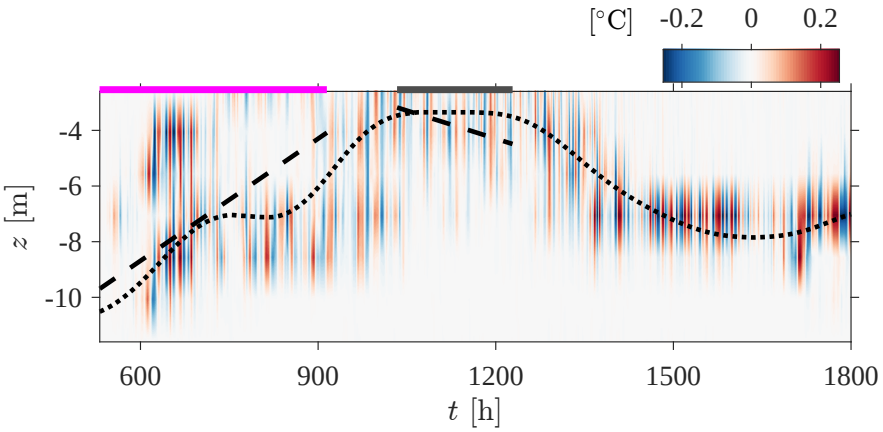

Figure 1.12: Small-scale temperature T' at thermistor string Tr (white cross in Figs. 1.1, 1.2–1.6) as a function of depth and time. The horizontal magenta, and gray bars span the release and deformation periods, respectively, and the dashed black line is the average slope of the $\bar{T} = 20.5$ °C isotherm (see Fig. 1.4). The dotted black line is the 3h large-scale filtered vertical location of maximum temperature stratification.

In addition to large-scale dye $\bar{D}$ and temperature $\bar{T}$, the small-scale D' and T' fields had rich structure and evolution (*e.g.,* D' in Fig. 1.2c). At mooring Tr, high frequency (HF, see Section 1.2.4) temperature fluctuations were approximately ± 0.25 °C with timescales of roughly 10 min (Fig. 1.12), longer than the depth- and time-averaged buoyancy period of roughly 4.5 min. HF IW fluctuations with similar timescale were observed at ADCP with u' magnitude of ≈ 1 cm s^{-1} (not shown).

The T' fluctuations were near-surface intensified (*i.e.,* the maximum $T'(z)$ was at $z \geq -6$ m) just prior to and throughout the deformation period, coincident with the maximum of the DIT cold phase (Fig. 1.12). Largest T' fluctuations occurred near the depth of the maximum 3 h large-scale filtered vertical temperature gradient (dotted line in Fig. 1.12) as expected from WKB theory (*e.g.,* Hendershott, 1981), indicating that the large-scale DIT modulated the vertical structure of the HF IWs, potentially enabling HF IWs to propagate into shallower water and

contribute to nearshore mixing and exchange. HF IWs are often linked to internal tide (*e.g.,* Zhang et al., 2015).

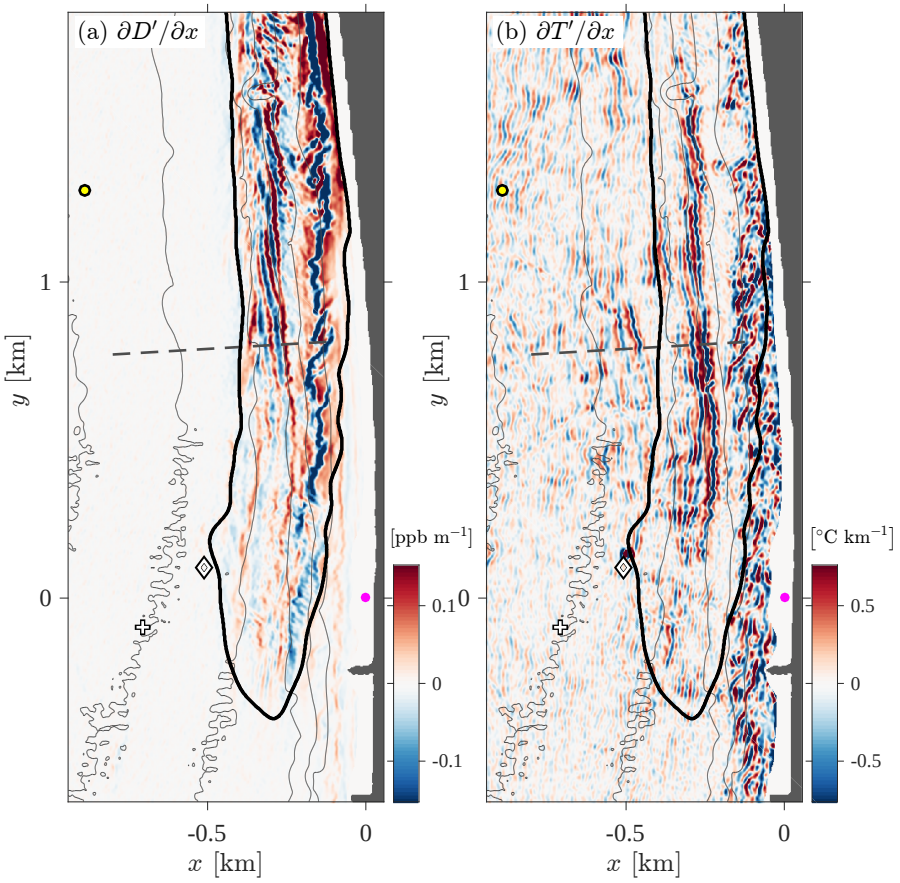

Figure 1.13: Snap-shot of (a) small-scale dye gradient $\partial D'/\partial x$ and (b) small-scale temperature gradient $\partial T'/\partial x$ versus x and y at $t = 1155$ h ($t_r = 6.60$ h). The cross-shore MASS transect is indicated with a gray dashed line and $\bar{D} = 1$ ppb contour shown in black (*e.g.,* see Fig. 1.6). Location of moorings Tr (white, +) and W1 (yellow, o) and dye release (magenta dot) are also indicated.

The signature of HF IWs are also evident in small scale surface temperature and dye fields (Fig. 1.13). HF IWs have been observed previously via aerial LWIR (*e.g.,* Walsh et al., 1998; Marmorino et al., 2004) with the surface T' signal attributed to IW modulation of the surface thermal layer (Farrar et al., 2007). The surface IW dye signal is likely the result of IW horizontal convergence (divergence) that thickened (thinned) the near-surface plume, slightly altering the remotely sensed concentration (*e.g.,* Fig. 1.2c). The cross-shore gradient ($\partial D'/\partial x$ and $\partial T'/\partial x$)

further highlights the small-scale features (Fig. 1.13). For example, at $t = 1155$ h, a packet of HF IW intersected the MASS transect (gray dashed line in Fig. 1.13) at $\tilde{x} \approx -200$ m and within the IS-plume. The packet was roughly alongshore oriented and extended between $200 \lessapprox y \lessapprox 1500$ m in $\partial T'/\partial x$ (Fig. 1.13b). This feature is also present in the $\partial D'/\partial x$ field for $500 < y < 1500$ m (Fig. 1.13a). Other, somewhat weaker, small-scale $\partial T'/\partial x$ features are present outside the plume, but not in the $\partial D'/\partial x$ field as $D = 0$. Onshore of $\tilde{x} = -250$ m, the signature of rip-currents are also present in D' and T', where features have significantly shorter (≈ 100 m) alongshore length scales.

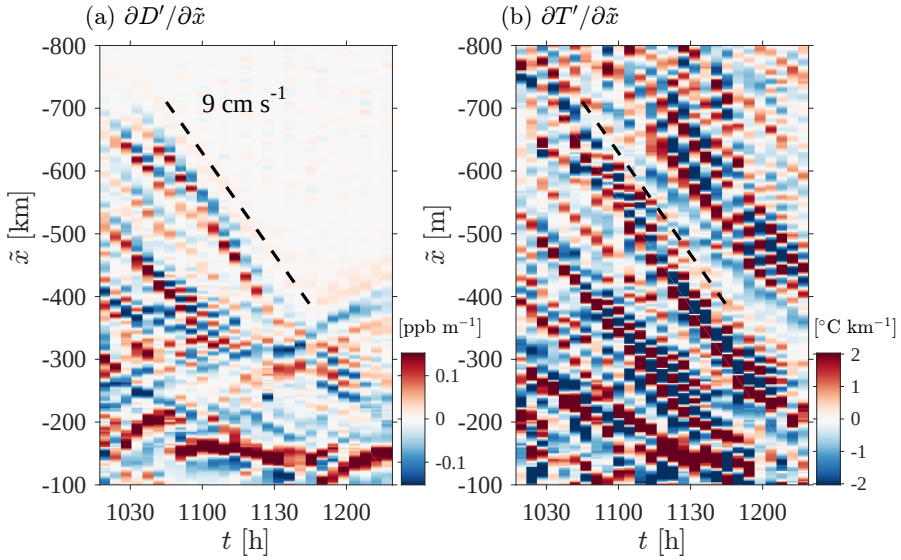

Figure 1.14: Small-scale dye $\partial D'/\partial \tilde{x}$ (a) and temperature $\partial T'/\partial \tilde{x}$ (b) on cross-shore MASS transect (dashed line in Fig. 1.13) versus local, shoreline referenced cross-shore coordinate $\tilde{x}$ and time t during deformation period. The dashed black line indicates an onshore progression of 9 cm s^{-1}.

During the deformation period, HF IWs with a cross-shore length-scale $\lambda_{iw} \approx 60$ m propagated shoreward through the IS-plume, as evidenced in the small-scale $\partial D'/\partial \tilde{x}$ and $\partial T'/\partial \tilde{x}$ Hovmöller plots (Fig. 1.14). The HF IW packet at $\tilde{x} \approx -200$ m in Fig. 1.13 entered the IS-plume along the MASS transect at $t \approx 1040$ h and $\tilde{x} \approx -700$ m (start of dashed line in Fig. 1.14a). The

packet propagated shoreward at roughly 9 $\mathrm{cm\,s^{-1}}$ to $\tilde{x} \approx -400$ m where a steeper trailing front developed (red and blue banding in Fig. 1.14b), consistent with wave steepening, and it rapidly decelerated onshore of $\tilde{x} \approx -300$ m. Several similar features intersected the MASS transect (onshore of TA and AUV) during the deformation period, each separated by approximately 30-45 min (*e.g.,* the front that passed $\tilde{x} = -500$ m at $t = 1030$ h in Fig. 1.14).

The steepening and deceleration of the surface features is qualitatively consistent with weakly nonlinear eKdV solutions on a slope (*e.g.,* Holloway et al., 1999). IW transformation (*i.e.,* steepening, and breaking) primarily results from changes in depth (*e.g.,* Sutherland et al., 2013) or stratification (*e.g.,* Grimshaw et al., 2004). Both mechanisms are possible as HF IW approach the SZ, where $h \to h_{\mathrm{sz}}$ (h_{sz} is the depth of the outer-SZ) and $N \to 0$.

Onshore of $\tilde{x} = -300$ m, the coherence between the HF IW D' and T' signals decreases. The fade in D' HF IW signal is partially due to aliasing near $\bar{D}_{\max}$ between $\tilde{x} = -300$ m and $\tilde{x} = -200$ m. Based on movies of small-scale dye and temperature fields, SZ generated TRCs were also active close to shore ($\tilde{x} \geq -250$ m $\approx -2.5L_{\mathrm{sz}}$, not shown). The TRC variability may be partially responsible for the decoherence of the propagating D' and T' fronts onshore of $\tilde{x} = -250$ m in Fig. 1.14. The eventual disintegration of the HF IW T' signals before reaching the SZ/IS boundary ($\tilde{x} = -L_{\mathrm{sz}} \approx -100$ m) suggests there is IW dissipation in the region $-400 \leq \tilde{x} \leq -100$ m. HF IW dissipation has been linked to vertical mixing on the shelf (*e.g.,* Walter et al., 2012), thus mixing may be enhanced in the region onshore of AUV and TA transects where IS-plume (D, T) statistics were stable. However, in the near-SZ region where surface HF IW signatures disappear, NLIW can still propagate to SZ as near bed cold bores (Sinnett et al., 2018).

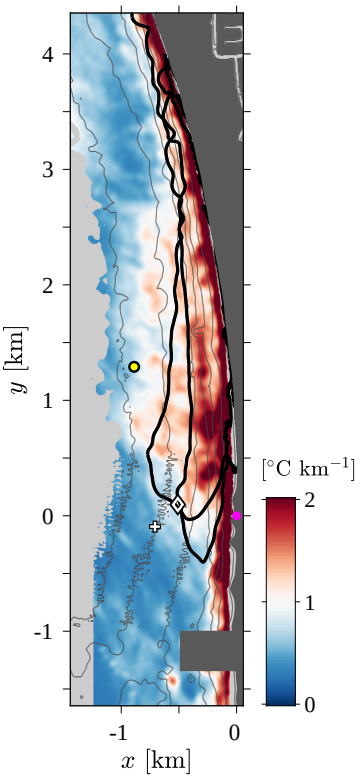

Figure 1.15: Time root-mean-square of the cross-shore, small-scale temperature gradient rms$(\partial T'/\partial x)$ during the deformation period $1020 \leq t \leq 1217$ h. The rms estimate was derived from 27 MASS passes of surface $\partial T'/\partial x$, and regions with fewer than 25 samples were removed prior to applying the large-scale spatial filter described in Section 1.2.4. Light gray are regions without data and the wake of the Imperial Beach pier at $y \approx -1$ km and land has been masked in dark gray.

The LWIR-observed HF IW activity was not alongshore uniform over the study region. The temporal rms$(\partial T'/\partial x)$ between 1020-1230 h was elevated on the IS in the region offshore of $0.5 \leq y \leq 2.5$ km, with magnitudes ≥ 1 °C km^{-1} or $\approx$ 2–3 times greater than to north and south (Fig. 1.15). The persistent small-scale gradients in this region are attributed to the HF IWs shown in Figs. 1.13 & 1.14, whereas the elevated signal onshore of roughly $2.5L_{\text{sz}}$ was due to TRC activity. The alongshore extent of the enhanced IS rms$(\partial T'/\partial x)$ bounds the region of IS-plume elongation (Fig. 1.11), suggesting that either incident HF IWs were intensified in this region or this was where the DIT shoaled the high N^2 region (*e.g.,* Fig. 1.12). The former implies HF IW mass-transport or momentum-flux driven plume elongation, whereas the latter implicates the DIT,

these mechanisms are discussed in Section 1.4.3.

1.4 Discussion

1.4.1 Summary of Results

The 3.84 h early morning dye release evolved for ≈ 5 h before intensive IS *in situ* and aerial remote observations began. Prior to deformation, the IS-plume was advected up to $8L_{sz}$ (800 m) offshore and was confined to the surface, with tracer above $\tilde{z} = -3$ m for $\tilde{x} \leq -400$ m (Fig. 1.7a). As aerial observations began, the IS tracer plume was observed deforming shoreward, elongating in the alongshore and being transported south, while SZ tracer was continuously transported northward (Fig. 1.5a-d). Large-scale Tr temperature and ADCP cross-shore velocity (Fig. 1.4a-b) indicate that the early morning offshore dye transport and mid-late morning deformation occurred during two phases of the DIT.

Over the deformation period, the offshore IS plume $\bar{D} = 1$ ppb front propagated onshore at roughly 5 $\mathrm{cm\,s^{-1}}$ as the IS-plume and its associated isotherms deepened at $\tilde{x} \approx -4L_{sz}$ along AUV (Figs. 1.4 and 1.7). The steepening offshore dye gradient indicates that onshore progression of the IS-plume was due to advection. Similarly, the IS-plume joint dye and temperature distribution was relatively stable offshore of $\tilde{x} = -4L_{sz}$, indicating that the IS-plume deepening was not predominantly due to vertical mixing.

During the deformation period, surface intensified HF IW (≈ 10 min period) were observed at mooring Tr (Fig. 1.12). These HF IW propagated onshore and through the IS-plume at roughly 9 $\mathrm{cm\,s^{-1}}$ for $\tilde{x} \leq -3L_{sz}$, then decelerated in shallower water, breaking up into multiple IWs and presumably steepening (Figs. 1.13 & 1.14). The HF IW variance was enhanced in the 2 km alongshore region of the IS-plume deformation and elongation, and was much weaker just to the north and south (Fig. 1.15).

1.4.2 Mechanism of IS-Plume Deepening

The IS isotherm and plume deepening observed by AUV, TA, and Tr during the deformation period could result from cross-shelf exchange flow or alongshore advection of an alongshore temperature and plume gradient, or a combination of the two. The DIT had both a cross-shore exchange structure (Fig. 1.4a-b) and (north-to-south) alongshore phase propagation (Fig. 1.3d), indicating the presence of an IS alongshore temperature gradient during the release and deformation periods. Here, an idealized two layer cross-shelf exchange model is used to examine whether the observed plume deepening can be due to surface onshore flow associated with the DIT relaxation.

By continuity and assuming alongshore uniformity, a two layer cross-shore exchange flow, with onshore flow at the surface and compensating offshore flow at depth, drives interface deepening. At a given cross-shore location x_0, onshore transport within the surface layer is balanced by an increase in (x,z) cross-sectional area A of the surface layer onshore of x_0, *i.e.,*

$$u_s H = \partial A/\partial t, \tag{1.2}$$

where u_s is the average surface velocity and $H(t)$ is the cross-shore uniform surface layer depth. As the IS-plume remained offshore of the SZ during the deformation (Fig. 1.6), the approximate area onshore of AUV (*i.e.,* with $x_0 = -400$ m) is,

$$A = HL_x - (H - h_{sz})^2(2\beta)^{-1}, \tag{1.3}$$

where $L_x = -(x_0 + L_{sz})$, $L_{sz} \approx 100$ m is the SZ width, and $h_{sz} \approx 2$ m is the depth at $\tilde{x} = -L_{sz}$, and $\beta = 0.017$ is the constant bathymetric slope. Substituting (1.3) into (1.2) and integrating (assuming constant u_s) gives, $u_s \approx \Delta t^{-1}[(L_x + h_{sz}\beta^{-1})\ln(H_f/H_i) - \beta^{-1}\Delta H]$, relating the surface layer deepening $\Delta H = H_f - H_i$ to the exchange velocity u_s. Based on the observed plume

deepening at AUV (initial $H_i = 3$ m and final $H_f = 6$ m at $\tilde{x} = -400$ m over $\Delta t \approx 3720$ s, Fig. 1.7a-b), the two layer exchange model implies a u_s of ≈ 3 cm s^{-1}. This velocity estimate is consistent with both the 5 cm s^{-1} onshore progression of the $\bar{D} = 1$ ppb front observed along MASS (Fig. 1.10a) and is of similar magnitude to the observed large-scale DIT cross-shore velocities below $z = -5$ m at ADCP (Fig. 1.4b).

Alternatively, southward advection of an alongshore gradient can appear as local temporal evolution (*i.e.,* $\partial H/\partial t \sim -\bar{v}\partial H/\partial y$, where $\bar{v}$ is the depth averaged alongshore current). Taking the observed deepening along TA, $\partial H/\partial y \approx 1.2$ m km^{-1}, and using the southward plume front velocity ($|\bar{v}| < 10$ cm s^{-1}), gives a maximum of $\partial H/\partial t \approx 0.43$ m h^{-1} or roughly 25% of the observed deepening at AUV. Additionally, the phase propagation of the DIT from the mooring array was much greater than the observed alongshore currents. Thus, the observed plume deepening and deformation was likely due to a cross-shore exchange flow associated with the DIT.

1.4.3 Mechanisms for IS-Plume Elongation

The IS-plume elongation (Fig. 1.11) suggests a near-surface alongshore straining $\partial v_s/\partial y$ of roughly 4.5 cm s^{-1} km^{-1}. The presence of both northward and southward propagating features in Fig. 1.11 indicates that the straining may be localized to the ≈ 2 km IS-plume elongation region ($0 \leq y \leq 2$ km), which overlaps the region of elevated HF IW surface rms$(\partial T'/\partial x)$ ($0.5 \leq y \leq 2.5$ km), suggesting there may be a relationship between the large-scale alongshore strain (elongation) and the IS HF IW alongshore inhomogeneity (Fig. 1.15).

An imbalance in the large-scale cross-shore 2-layer DIT exchange flow due to excess onshore surface flow in the elongation region, *i.e.,* $u_s(y)$, can support an alongshore strain. Assuming the cross-shore convergence occurs over $L_x \approx 500$ m (the approximate cross-shore width of the IS-plume), an excess onshore $u_s \approx 2.25$ cm s^{-1} is sufficient to support the observed straining. This implies a DIT $u_s \approx 5.25$ cm s^{-1} in the elongation region, slightly larger than the

onshore progression of the $\bar{D} = 1$ ppb front. This would also require the DIT to have a relatively short ≈ 4 km alongshore length scale, either due to direction of propagation or alongshore gradients induced by the geometry of the San Diego Bight.

HF IWs can drive cross-shore mass transport. A single non-dissipative internal solitary wave induces horizontal mass displacement that increases with non-linearity, represented by the ratio of IW fluid velocity u_{iw} to wave celerity c, and with wave-length (*i.e.,* u_{iw}/c and λ_{iw}, *e.g.,* Lamb, 1997). Based on observed IW characteristics ($u_{\mathrm{iw}}/c \approx 0.11$ and $\lambda_{\mathrm{iw}} \approx 60$ m), the individual solitary IW surface displacement was potentially $O(1.5\ \mathrm{m})$ (Lamb, 1997, Eq. A8). In a wave averaged sense, incremental solitary wave displacements lead to mass transport (*e.g.,* Shroyer et al., 2010; Zhang et al., 2015), analogous to surface gravity wave Stokes drift (Henderson, 2016). Over the deformation period the HF IWs potentially account for a net onshore displacement of roughly 15 m (*i.e.,* passage of 10 waves), or an IW induced $u_s \approx 0.2\ \mathrm{cm\,s^{-1}}$. Thus, internal solitary wave Stokes drift was insufficient to support the observed elongation.

In addition to IW Stokes drift, IWs also have a momentum flux, akin to a radiation stress. Wave-dissipation induced divergence of IW momentum flux generates cross-shore pressure gradients (*e.g.,* Wunsch, 1971; Suanda et al., 2017) and, for obliquely incident IWs, alongshore currents (*e.g.,* Thorpe, 1999; Zikanov and Slinn, 2001). In the region $-4L_{\mathrm{sz}} \geq \tilde{x} \geq -2.5L_{\mathrm{sz}}$, observed HF IWs appear to steepen and dissipate (Fig. 1.14) and HF IW activity was concentrated in the elongation region (Fig. 1.15). In analogy to alongshore gradients in surface gravity wave height (and radiation-stress) generating alongshore SZ pressure gradients and circulation cells (Bowen, 1969), an elevated IW energy flux and dissipation in the region of the IS-plume might create a baroclinic pressure driven alongshore elongation. In the context of IWs incident on near-critical slopes, breaking and along-slope flow is generated near the bottom or within a critical layer (*e.g.,* Zikanov and Slinn, 2001), and thus are not likely to cause near-surface currents. However, in the present case of HF low-mode or solitary-like waves dissipating near shore, the vertical structure or velocity scale is unclear.

As the DIT was responsible for the observed large-scale cross-shore exchange flow, and the magnitude of the exchange velocity (inferred from velocities below $z < -5$ m) were of similar magnitude as needed to support both deepening and straining, the DIT was therefore also likely responsible for the IS-plume alongshore elongation. While other possible mechanisms can induce strain, they were not consistent with observations. Although, a contribution from HF IW momentum flux cannot, at present, be discounted. In either case (DIT or HF IW momentum flux), this implies an inhomogeneity of the DIT over the fairly narrow alongshore elongation region. If the HF IWs were generated through an instability of the DIT, then spatial patterns of the DIT would subsequently be reflected in the HF IW field, hence the patterns in Fig. 1.15.

1.4.4 Influence of Tracer Release Timing

Previous SZ dye release experiments released from mid- to late morning and observed alongshore SZ transport over several km and dye confined to within $2L_{sz}$-$3L_{sz}$ (*e.g.,* Grant et al., 2005; Clark et al., 2010; Hally-Rosendahl et al., 2015). These three dye releases took place in Southern California in May, September, or October when solar forcing was strong. A mid-day tidal inlet dye release during strong obliquely incident waves and alongshore wind, had dye transported alongshore in the SZ for about 9 km and also largely confined $2L_{sz}$-$3L_{sz}$ (Feddersen et al., 2016). The observed SZ-IS temperature difference was ≈ 1 °C, due to warm dye-laden ebb tidal-inlet water in the SZ. In contrast, following R2, dye was observed out to $\tilde{x} = -8L_{sz}$, and the subsequent IS-plume shoreward deformation and late morning to afternoon southward transport (Fig. 1.5), is in stark contrast to the more canonical SZ-plume towards the north ($y \geq 3$ km, Fig. 1.5). Here, the influence of the early morning release timing (0518-0908 h) relative to the DIT and solar cycle is examined.

Tracer release began when the SZ was colder than the surface-IS (*i.e.,* $t < 0800$ h, Fig. 1.4c). As such, tracer exchanged onto the IS prior to 0800 h would have been expected to preferentially spread offshore at depth, largely following the tracer release isotherm (*i.e.,* weak

mixing). In a modeling study of TRC SZ-IS exchange without solar forcing, SZ released tracer was transported offshore in an IS sub-surface layer due to the interaction of TRCs and IS stratification (Kumar and Feddersen, 2017c). However, despite the SZ being colder than the near-surface IS during much of the release, the IS plume was surface intensified because the DIT drew even colder water onshore at depth preventing IS-plume subduction. If the DIT had not occurred, the IS-plume may have remained closer to shore with subduction of the dye maximum, as observed farther north at $y = 2.5$ km near the boundary between SZ and IS plumes (Fig. 1.8).

In addition to influencing the vertical structure and cross-shore extent of the IS-plume during the release period, the DIT also modulated the IS-plume thermal evolution. Hally-Rosendahl et al. (2014) observed a SZ and IS (D,T) distribution, with higher average SZ dye and temperature and stronger IS stratification. Here, a similar (D,T) relationship was observed prior to the deformation period (circles, Fig. 1.9), although with some differences. The Hally-Rosendahl et al. (2014) dye was released in $T > 19$ °C and was diapycnally mixed to $T = 18$ °C on the IS within $2L_{\mathrm{sz}}$. Here, the IS-plume tracer was quasi-adiabatically advected to a depth of 6 m at $4L_{\mathrm{sz}}$-$6L_{\mathrm{sz}}$ with cross-isotherm dye mixing limited to ≤ 0.5 °C.

Additionally, the mid-late morning increase in SZ-IS plume temperature separation (Fig. 1.9) resulted from the early morning cross-shore plume advection (*i.e.,* the $8L_{\mathrm{sz}}$ cross-shore extent), and a reduced solar heating in deeper water. As such, by the end of the deformation period, the SZ and IS plumes had a ≈ 1 °C mean temperature difference even though they had similar mean dye concentration (Fig. 1.9). Subsequently, during and after deformation, the warmer SZ may have been a thermal barrier for the IS-plume. Omand et al. (2011) argued a similar mechanism prevented an IS phytoplankton bloom from reaching the warm SZ following a large IW upwelling event.

Shoreline-released tracer released at alternate phases of either the internal tide or the solar cycle would be expected to evolve differently. In particular, tracer released during the deformation period (warm surfzone) would likely not have formed the IS-plume and the overall alongshore

plume extent would have largely followed the northward SZ currents. Alternatively, if tracer had been released even earlier in the DIT cooling phase (*i.e.,* around mid-night) with SZ colder than near-surface IS, even more tracer may have been advected onto the IS with subsequent southward advection over the deformation and elongation period. Thus, release timing relative to the solar cycle and any internal tide events is relevant to the transport and dispersion of shoreline-released tracers (*e.g.,* human pathogens, or larvae) to the IS and also likely for the IS to the SZ.

1.5 Summary & Conclusions

An early-morning SZ tracer release coinciding with the cooling phase of the DIT resulted in, an anomalously large (relative to previously observed SZ dye release experiments) $8L_{sz}$ cross-shore plume width after 3-5 h, extending well onto the IS. During the subsequent DIT warming phase (next $\approx$ 2 h), this IS-plume deformed (narrowed) cross-shore to $5L_{sz}$, vertically thickened by up to 3 m, and strained (elongated) alongshore, yet remained offshore of the SZ. This large-scale IS-plume evolution is consistent with a simple 2-layer cross-shore exchange model.

The DIT-augmented cross-shore tracer transport also coincided with the transition from night-time cooling to solar heating. The shallow SZ warmed more rapidly than the near-surface IS, inducing separate SZ- and IS-plume T evolution. The development of a positive cross-shore temperature gradient may have blocked the IS-plume from entering the SZ. Additionally, a DIT alongshore gradient (over $\approx$ 2 km) could support the observed IS-plume elongation. Small-scale processes, *e.g.,* TRC and HF IW, interacted with the IS-plume, likely contributing to vertical mixing onshore of $4L_{sz}$ and SZ-IS exchange. Coupled with opposing SZ/IS alongshore currents, the release timing relative to both the DIT and solar cycle resulted in the $\approx$ 9 km alongshore plume extent in roughly 12 h (*i.e.,* SZ-plume $\approx$ 7 km north of release and IS-plume $\approx$ 2 km south of the release).

These observations demonstrate that nearshore tracer exchange is influenced by both SZ and IS processes spanning a broad range of scales. Here, we have shown that the interaction and relative phasing of the DIT with solar warming can have a significant effect on the evolution of shoreline released tracer over $\approx$ 5-12 h.

Acknowledgements

Thanks to two anonymous reviewers who greatly helped improve this manuscript. This work was funded under the CSIDE grant by the National Science Foundation (NSF OCE-1459389), and through the NSF Graduate Research Fellowship Program. Data was made available in part by SIO CDIP, and the Tijuana River National Estuary Research Reserve and are available through the CSIDE web-page (https://scripps.ucsd.edu/projects/cside/) or by contacting the corresponding author. The U.S. Navy provided access to Navy property for data collection. We thank Ken Melville, Luc Lenain, Nick Statom, and Stephen Holleman for acquisition and preliminary processing of MASS data. We thank YMCA: Camp Surf for providing a base of operations; the cities of Imperial Beach and Coronado, the US Navy and CA State Parks for accommodating our research activities; and the numerous Imperial Beach lifeguards, UCSD/SIO students, and volunteers for efforts to keep beachgoers safe and monitor surfzone instrumentation. Chapter 1, in full, is a reprint of the paper Cross-shore Deformation of a Surf-zone Released Dye Plume by Internal Tide on the Inner-shelf in Journal of Physical Oceanography by D. J. Grimes, F. Feddersen, S. N. Giddings and E Pawlak in 2020. The dissertation author was the primary investigator and author of this paper.

Chapter 2

Tracer Exchange Across the Stratified Inner-shelf Driven by Transient Rip-Currents and Diurnal Surface Heat Fluxes

Abstract

Exchange across the surf-zone and inner-shelf affects coastal water quality and larval recruitment. Surf-zone generated transient rip-currents (TRC) exchange shoreline released tracers onto and across a stratified inner-shelf. Surface heat fluxes (SHF) modify inner-shelf stratification and surf-zone temperature, relative to the inner-shelf, inducing nearshore thermally driven exchange. The coupled effect of TRC and diurnal SHF forcing on cross-shore exchange is evaluated using idealized model surf-zone tracer releases with TRC-only, SHF-only, and combined SHF+TRC forcing. For conditions representing Fall in Southern California, the TRC mechanism dominates cross-shore exchange, relative to SHF, to $12L_{SZ}$ offshore ($L_{SZ} = 100$ m is

the surf-zone width). Tracer and velocity derived estimates of exchange velocity indicate that the TRC cross–inner-shelf exchange mechanism is due to an alongshore mean baroclinic flow set up by TRC vertical mixing of inner-shelf stratification.

Plain Language Summary

Cross-shore transport (also called exchange) of material, *e.g.,* pollutants, larvae, nutrients, plankton, is important in coastal oceanography. Natural surf-zone wave breaking leads to transient rip-currents (TRC), episodic, offshore flows onto the inner-shelf, which vertically mix stratified waters creating a cross-shore exchange pathway. In many regions, such as Southern California, daily surface heating/cooling, or diurnal surface heat-fluxes (SHF), also drive cross-shore exchange, because thermal response varies with water depth. However, the dominant exchange mechanism is not known. Impacts of combined TRC and SHF forcing on exchange and their relative strength are analyzed using idealized numerical model simulations. Cross-shore transport is quantified using a tracer released within the surf-zone. Tracer transport is strongest for simulations including TRCs, relative to SHF forcing alone, and transport induced by TRCs extends well offshore of the surf-zone. Analyses indicate that enhanced TRC driven inner-shelf exchange is associated with the vertical mixing mechanism.

2.1 Introduction

The cross-shore exchange of tracers (*e.g.,* larvae, pollutants) affects marine population connectivity (*e.g.,* Pineda et al., 2007) and coastal water quality (*e.g.,* Boehm et al., 2017). Various mechanisms contribute to tracer exchange across the nearshore, the region encompassing the inner-shelf (water depths $\lesssim$ 15 m) and surf-zone (region of depth limited wave breaking) (*e.g.,* Morgan et al., 2018). Away from rivers (*e.g.,* Rodriguez et al., 2018) and under weak wind

forcing (*e.g.,* Lentz, 2001; Lentz and Fewings, 2012), nearshore tracer exchange may be driven by surface heat fluxes (*e.g.,* Monismith et al., 2006; Molina et al., 2014) and surf-zone induced rip-currents (*e.g.,* Castelle and Coco, 2013; Hally-Rosendahl et al., 2014; Suanda and Feddersen, 2015). Under natural conditions, these two processes occur simultaneously. Yet, the combined effect of rip-currents and surface heat flux forcing on inner-shelf cross-shore exchange and their relative importance are not known.

Thermally driven cross-shore flows are an important and ubiquitous inner-shelf exchange mechanism (*e.g.,* Monismith et al., 2006; Molina et al., 2014; Herdman et al., 2015; Ulloa et al., 2018), particularly as Ekman transport is shut-down on the shallow inner-shelf (*e.g.,* Lentz and Fewings, 2012). Spatially uniform surface heat-flux (SHF) sets up cross-shore thermally driven inner-shelf circulation owing to depth dependent thermal response, with shallower regions heating/cooling more rapidly (*e.g.,* Farrow and Patterson, 1993). Diurnal (24 h) cycle solar heating/cooling drives diurnal exchange flow, with observed inner-shelf offshore directed flows of ≈ 2 cm s^{-1} near the surface for heating response and at depth for cooling (Monismith et al., 2006; Molina et al., 2014). The heating/cooling cycle also strongly affects stratification. During daytime, most short-wave radiation is distributed within the upper 1-2 m, depending on water properties, increasing near-surface stratification and confining cross-shore thermal gradients to regions onshore of a depth comparable to the absorption length-scale (Lei and Patterson, 2002). In contrast, nighttime surface cooling induced convection erodes stratification, developing a surface mixed layer and an offshore gravity current where convection extends to the bottom (Mao, 2019). Regions conducive for diurnal SHF driven exchange may also be exposed to waves, but the impact of surf-zone processes on thermally driven exchange is not clear (*e.g.,* Molina et al., 2014). Previous thermally driven exchange studies within 1 km of the coast assumed weak wave effects, because inner-shelf moorings were well outside the surf-zone and estimated Stokes drift velocities were small compared to observed Eulerian currents (Monismith et al., 2006; Molina et al., 2014). On a wave exposed reef flat, diurnal thermally driven exchange was relatively

unaffected by wave height (Molina et al., 2014), but wave range was limited and alongshore variability was strong.

Transient rip-currents (TRCs) are strong, episodic offshore directed flows commonly generated within natural surf-zones (*e.g.,* Johnson and Pattiaratchi, 2006) that dominate tracer exchange between the surf-zone and inner-shelf (*e.g.,* Reniers et al., 2010; Clark et al., 2011; Hally-Rosendahl et al., 2014, 2015). Recently, based on idealized simulations, TRC induced mixing on the stratified inner-shelf generated a sub-surface baroclinic exchange pathway that transported surf-zone released tracer across the inner-shelf at $\approx 1.5\ \mathrm{cm\,s^{-1}}$ (Kumar and Feddersen, 2017b,c). This exchange mechanism depends critically on the inner-shelf stratification. However, surface heat flux (SHF) effects, that modulate stratification, were neglected in these simulations. Separate surf-zone tracer release experiments conducted in early Fall in Southern California observed SHF forced thermal gradients, where surf-zone temperature, relative to the inner-shelf was warm midday (Hally-Rosendahl et al., 2014) and cold early-morning (Grimes et al., 2020a). However, SHF effects on exchange were not examined. Whether the TRC driven inner-shelf baroclinic exchange mechanism is maintained with diurnal SHF-forced stratification and circulation effects is unknown, nor is how the magnitude of these exchange mechanisms compare.

Herein, idealized surf-zone tracer release simulations are performed to evaluate exchange across the inner-shelf induced by combined SHF and TRC forcing. Because both SHF- and TRC-induced exchange rely on baroclinic pressure gradients and vertical mixing, simulations are conducted for SHF and TRC forcing both separately and combined with different model initialization times relative to the surface heat flux cycle and different tracer release times relative to model initialization, allowing for an ensemble averaging analysis approach (Section 2.2). The relative strength of SHF and TRC induced exchange mechanisms are evaluated from tracer mass distributions (Section 2.3). Dominant exchange mechanisms and underlying processes are quantified with different exchange velocity definitions (Section 2.4).

2.2 Methods

2.2.1 Model Setup & Forcing

Simulations are performed using the Coupled Ocean Atmosphere Wave and Sediment Transport (COAWST) modeling system (Warner et al., 2010; Kumar et al., 2012) coupling the σ-coordinate Boussinesq and hydrostatic ROMS circulation model (Shchepetkin and McWilliams, 2005) with the SWAN wave model (Booij et al., 1999). SWAN provides ROMS with bulk wave parameters to estimate Stokes drift velocity $u_S(z)$, breaking-wave turbulence source, and phase-averaged wave forcing. TRCs are generated by adding surf-zone barotropic-rotational body forcing via one-way coupling with wave-resolving model funwaveC, as developed and validated by Kumar and Feddersen (2017a).

The 1 km alongshore (y) uniform and periodic domain extends cross-shore (x) 5 km (Figure 2.1a). Alongshore resolution is fixed at $\Delta y = 2$ m. Cross-shore resolution is concentrated nearshore, with constant $\Delta x = 1.25$ m for $-690 < x < 0$ m that increases smoothly offshore to $\Delta x = 200$ m. The Southern California characteristic bathymetry $z = -h(x)$ (black, Figure 2.1a) matches Kumar and Feddersen (2017a,b) for $x > -800$ m. For $x > -200$ m, $h(x)$ has constant slope of 0.025, transitioning offshore to a smaller 0.004 slope, and $h = 28$ m at the offshore boundary. Fifteen vertical σ-layers are used (gray, Figure 2.1a). The extended cross-shore domain, relative to 800 m in Kumar and Feddersen (2017a,b), minimizes offshore boundary conditions influence.

Similar model parameters to Kumar and Feddersen (2017a,b,c) are used including homogeneous quadratic bottom drag coefficient of $C_d = 0.0025$ and Coriolis parameter $f = 7.7 \times 10^{-5}$ s^{-1}. To account for the increased lateral diffusivity associated with surfzone bores (Feddersen, 2007), the momentum and tracer lateral eddy viscosities $K_H = 0.01$ m^2 s^{-1} are increased to $K_H = 0.2$ m^2 s^{-1} within the surf-zone $x > -L_{sz} = -100$ m for simulations with waves, where L_{sz} is the surf-zone width. This background surf-zone eddy viscosity is 5× smaller than tracer/drifter

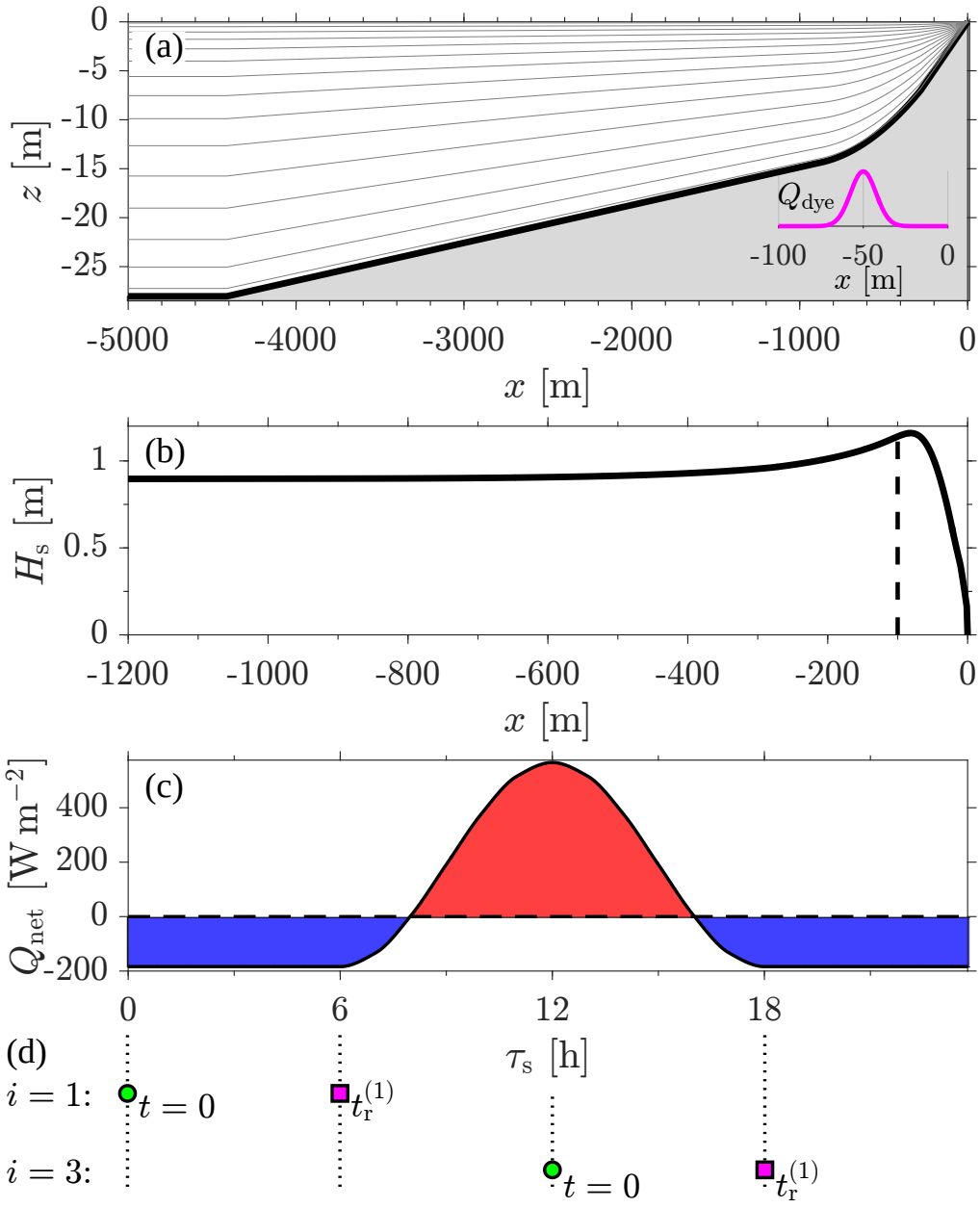

Figure 2.1: (a) Cross-shore bathymetry $z = -h(x)$ (black) with terrain following σ-coordintes (gray) showing the full 5 km cross-shore domain. Inset shows form of surf-zone bottom tracer flux Q_{dye} centered on $x = -50$ m (magenta). (b) SWAN model significant wave height for $x > -1200$ m (H_{s} is roughly constant offshore) with a vertical dashed line at $x = -L_{\text{sz}}$ delimiting the surf-zone boundary. (c) Net surface heat flux Q_{net} cycle with red/blue highlighting heating/cooling phases. In (d) are solar initialization times $t_{\text{s}}^{(i)}$ (green) for $i = \{1,3\}$ and solar time of the first tracer release $t_{\text{r}}^{(1)}$ (red).

derived eddy diffusivity estimates for similar wave height and beach slope as surfzone eddies dominate lateral mixing (Clark et al., 2010, 2011) and are resolved in these simulations. The vertical eddy viscosity K_{V} is given by the $k-\varepsilon$ turbulence closure model (Warner et al., 2005) where (as commonly practiced, *e.g.,* Rodriguez et al., 2018; Kumar et al., 2012) 15% of the wave dissipation is supplied as a surface turbulent kinetic energy flux, consistent with surf-zone turbulence observations (*e.g.,* Feddersen, 2012). The remaining energy dissipation occurs in the surface roller (*e.g.,* Feddersen and Trowbridge, 2005).

The 48 h long simulations are initialized from rest with uniform stratification and $T(z) = 20 + 0.25z$ °C, throughout. The seabed is adiabatic and the offshore boundary temperature is clamped to either the temperature initial condition for runs without SHF or to a 1-D (vertical) $T(z,t)$ evolution for runs that include SHF. The 1-D $T(z,t)$ evolution is estimated via 48 h single-column simulations with offshore boundary depth of 28 m. The $x = 0$ boundary is closed, and the offshore boundary cross-shore Lagrangian velocity u_{L} (Eulerian + Stokes drift) is zero.

Model forcing is representative of Southern California in Fall. Four forcing cases (I-IV) are considered: I) a control case (denoted ø) without external forcing and represents the evolution due to background mixing, *i.e.,* as determined by K_{H}, and K_{V}; II) the wave and rotational-body forced case (denoted TRC), without surface heat fluxes, similar to Kumar and Feddersen (2017c), but with larger cross-shore domain and modified tracer releases (described later); III) is a diurnal SHF forcing case (denoted SHF) without any wave forcing; and IV) the novel combination of diurnal SHF with wave and rotational-body forcing (denoted SHF+TRC). For TRC and SHF+TRC, normally incident waves representing medium sized swell have 10° directional spread, peak period of 10 s and significant wave height of $H_{\mathrm{s}} \approx 1$ m at $x = -L_{\mathrm{sz}}$, where breaking begins (dashed, Figure 2.1b).

For SHF and SHF+TRC simulations, incident short-wave radiation, with maximum $Q_{\mathrm{sw}} = 750\ \mathrm{W\,m^{-2}}$, is distributed over the water column following a double-exponential vertical decay for Jerlov water-type I (Paulson and Simpson, 1977, with 58% over 0.35 m and the

remainder over 23 m). The short-wave cycle follows $\cos^2(2\pi\tau_s/\tau_{day})$ over solar time $\tau_s \in [6, 18\text{ h}]$, with solar day duration $\tau_{day} = 24$ h. Uniform (in space & time) surface longwave outgoing radiation is applied. This results in periodic net surface heat flux Q_{net} (Figure 2.1c) with midday, $\tau_s = 12$ h, maximum of 565 $\mathrm{W\,m^{-2}}$ and midnight minimum of -185 $\mathrm{W\,m^{-2}}$ and zero net daily heat flux. Other surface buoyancy flux sources (sensible heat flux, MacMahan et al., 2018), the effect of wave heating and surf-zone albedo (Sinnett and Feddersen, 2018), and wind stress effects (*e.g.,* Farrow, 2013, 2016) are not considered.

The transient evolution of SHF simulations will vary with the solar forcing phase at model initialization. This transient evolution is evaluated through four independent runs, referenced using superscript $i = \{1,2,3,4\}$, which vary the solar time at initialization, $t_s = \{0, 6, 12, 18\text{ h}\}$ relative to periodic Q_{net}. In so doing, time relative to the solar day $\tau_s^{(i)}$ is given by,

$$\tau_s^{(i)} = t + t_s^{(i)}, \tag{2.1}$$

where t is model time. This is illustrated in Figure 2.1c-d. Run $i = 1$ is initialized at midnight, $t_s^{(1)} = 0$ h, giving solar time $\tau_s^{(1)} = t$ (green dot right of $i = 1$, Figure 2.1d), whereas run $i = 3$ is initialized midday, $t_s^{(3)} = 12$ h, giving solar time $\tau_s^{(3)} = t + 12$ h (green dot right of $i = 3$, Figure 2.1d). Ensemble averages (described in Section 2.2.2) are formed with the staggered $t_s^{(i)}$ to remove variability due to solar initialization time.

Tracer D is released over 15 min from the bed with flux Q_{dye} centered on $x = -50$ m (magenta, Figure 2.1a). The tracer flux Q_{dye} is normalized such that a homogeneous plume confined to the SZ ($x > -L_{sz}$) has unit concentration (Kumar and Feddersen, 2017c), making D a measure of tracer dilution (*e.g.,* $D = 0.02$ indicates a $1/50$ decrease in plume concentration). The 48 h simulations are intrinsically transient due to the initial conditions, forcing, and irreversible mixing. Thus, tracer evolution depends upon tracer release time. To account for this, four separate tracer releases are performed at 6 h intervals following an initial 6 h adjustment period for surf-zone vorticity to equilibrate (Kumar and Feddersen, 2017a) and inner-shelf circulation to

respond to thermal forcing (*e.g.,* Molina et al., 2014; Monismith et al., 1990). Tracer releases are referenced using superscript j, such that $D^{(i,j)}$ represents tracer from the i^{th} SHF run and j^{th} tracer release. The model time of the release is denoted $t_{\text{r}}^{(j)}$, and in Figure 2.1d the first release, at $t_{\text{r}}^{(1)} = 6$ h, is indicated with a red square for SHF runs $i = \{1,3\}$. The elapsed time since tracer release is

$$\tau_{\text{r}}^{(j)} = t - t_{\text{r}}^{(j)}. \tag{2.2}$$

Both solar time $\tau_{\text{s}}^{(i)}$ and time since tracer release $\tau_{\text{r}}^{(j)}$ are used in the analysis.

2.2.2 Averaging Methods

The alongshore average is denoted with an over-bar, *i.e.,* for generic variable $c^{(i)}$,

$$\overline{c}^{(i)} = L_y^{-1} \int_0^{L_y} c^{(i)} \, \mathrm{d}y, \tag{2.3}$$

where $c^{(i)}$ is derived from the i^{th} model run with solar initialization time $t_s^{(i)}$ and $L_y = 1$ km is the alongshore domain length. Alongshore averaged temperature $\bar{T}$, cross-shore Lagrangian velocity $\bar{u}_{\text{L}}$, overturning streamfunction $\bar{\Psi}$, and vertical eddy diffusivity $\langle K_{\text{V}} \rangle$ are also time averaged over the 24 h diurnal time-scale, *i.e.,*

$$\left\langle c^{(i)} \right\rangle^{24\,\text{h}} = (\tau_{\text{day}})^{-1} \int_{6\text{ h}}^{30\text{ h}} c^{(i)} \, \mathrm{d}t, \tag{2.4}$$

where t is model time. Additionally, variables $\left\langle c^{(i)} \right\rangle^{24\text{ h}}$ are ensemble averaged over the (i)-indices, forming an initialization ensemble averaged $\langle c \rangle^{24\text{ h}}$, to average over transient effects associated with t_{s}.

For SHF and SHF+TRC simulations, tracer D evolution depends on both the solar time τ_{s} of the tracer release (see $t_{\text{r}}^{(1)}$ for $i = \{1,3\}$ in Figure 2.1d) and the model spin-up prior to tracer

release, *i.e.,* with $t_{\mathrm{r}}^{(j)}$. As tracer evolution is secular a 24 h time mean is not used. An initialization and release ensemble averaged alongshore mean tracer field $\langle \bar{D} \rangle_{\mathrm{r}}$ is formed by aligning the four tracer releases relative to the time since tracer release $\tau_{\mathrm{r}}^{(j)}$ (2.2) and then ensemble averaging over solar (i) and spin-up (j) times, formally,

$$\langle \bar{D} \rangle_{\mathrm{r}} (x, z, \tau_{\mathrm{r}}) = \frac{1}{16} \sum_{i=1}^{4} \sum_{j=1}^{4} \bar{D}^{(i,j)}(x, z, \tau_{\mathrm{r}}^{(j)}) \tag{2.5}$$

where $\bar{D}^{(i,j)}$ is the alongshore mean tracer concentration field from the i^{th} SHF run and j^{th} tracer release, and $\tau_{\mathrm{r}} \in (0, 24\ \mathrm{h}]$. The ensemble average (2.5) captures the tracer bulk time evolution by averaging over successively longer model spin-up times, *e.g.,* $t_{\mathrm{r}}^{(1)} = 6$ h versus $t_{\mathrm{r}}^{(4)} = 24$ h, and solar cycle timing, *e.g.,* $i = \{1, 3\}$ and $j = 1$ in Figure 2.1d. For ø and TRC simulations (*i.e.,* no SHF) the release ensemble average is only over (j) and also denoted $\langle \bar{D} \rangle_{\mathrm{r}}$.

2.3 Results

2.3.1 Combined Influence of Surface Heat Flux, Wave, and Transient Rip-Current Forcing on Instantaneous Fields

Examples from SHF+TRC forced simulations at solar-times $\tau_{\mathrm{s}} = 0$ h (midnight, Figure 2.2, left) and $\tau_{\mathrm{s}} = 12$ h (midday, Figure 2.2, right) illustrate effects of SHF and TRCs on instantaneous T and D. Midnight temperature $T^{(3)}$ (Figures 2.2a and 2.2c) was extracted from run $i = 3$ at model time $t = 12$ h, giving solar time (2.1) $\tau_{\mathrm{s}}^{(3)} = t + t_{\mathrm{s}}^{(3)} = 24$ h (Figures 2.1c-2.1d). The concurrent tracer $D^{(3,1)}$ (*i.e.,* release $j = 1$, Figure 2.2e and 2.2g) has tracer release time (2.2) $\tau_{\mathrm{r}}^{(1)} = t - t_{\mathrm{r}}^{(1)} = 6$ h. Similarly, midday ($i = 1$) temperature $T^{(1)}$ (Figure 2.2b and 2.2d) has model time $t = 12$ h and tracer $D^{(1,1)}$ (Figure 2.2f and 2.2h) is at $\tau_{\mathrm{r}}^{(1)} = 6$ h. The surface temperature anomaly $\Delta T^{(i)}$ relative to the $x = -150$ m alongshore average surface temperature is used to enhance horizontal thermal structure (Figure 2.2a-2.2b).

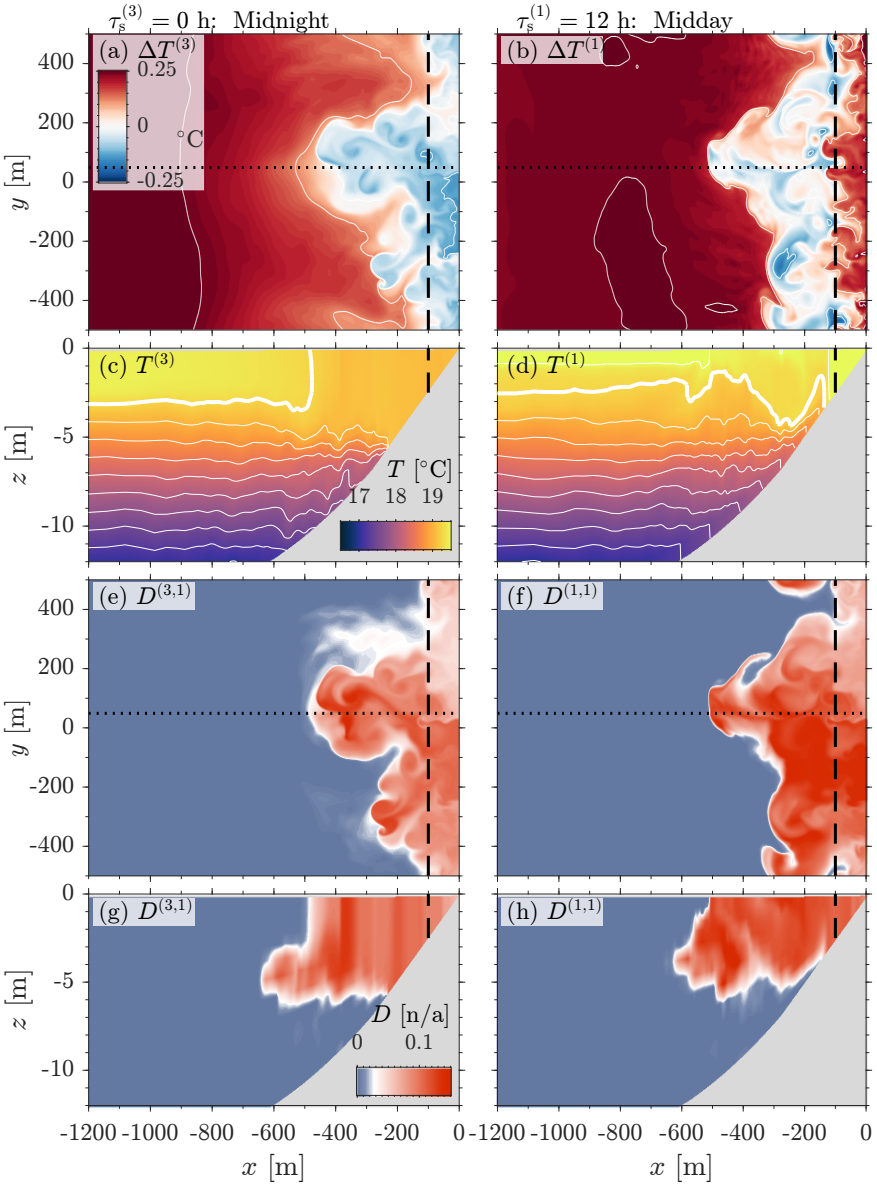

Figure 2.2: Instantaneous SHF+TRC forced runs at solar midnight ($\tau_s^{(3)} = 0$ h, left panels) and midday ($\tau_s^{(1)} = 12$ h, right panels) (a)-(b) surface temperature anomaly $\Delta T^{(i)}$; (c)-(d) cross-shore sub-surface temperature $T^{(i)}$; (e)-(f) surface and (g)-(h) cross-shore sub-surface tracer $D^{(i,1)}$. Surface panels (a,b,e,f) are functions of (x,y) and sub-surface panels (c,d,g,h) are functions (x,z) along $y = 50$ m (black dotted line in a,b,e,f). Snap-shots from model time $t = 12$ h, such that solar time (2.1) is $\tau_s^{(i)} = 12 + t_s^{(i)}$ where $i = \{3,1\}$, and in (e)-(f) time relative to tracer release (2.2) is $\tau_r = 12 - t_r^{(1)} = 6$ h. The outer limit of the surf-zone $x = -L_{sz}$ is indicated with a black dashed line and the bottom is gray.

The midnight ($\tau_s = 0$ h) $\Delta T^{(3)}$ (Figure 2.2a) shows consistent cooling toward shore with complex and irregular isotherm structure. Near-surface temperature also decreases toward shore along the $y = 50$ m cross-shore transect (Figure 2.2c), particularly near $x \approx -500$ m with near-vertical 19.25 °C isotherm from $z = -4$ m to $z = 0$ (thick contour, Figure 2.2c). For $x < -500$ m, the surface mixed layer is ≈ 3 m deep, whereas onshore temperature is well mixed to ≈ 5 m depth or to the bottom. The midnight surface $D^{(3,1)}$ field (Figure 2.2e) covaries with $\Delta T^{(3)}$, with high $D^{(3,1)}$ corresponding to cold $\Delta T^{(3)}$. As with sub-surface $T^{(3)}$ (Figure 2.2c), sub-surface $D^{(3,1)}$ is vertically well mixed for $x > -500$ m and $z > -5$ m (Figure 2.2g), with very sharp vertical front just offshore of $x = -500$ m. Farther offshore, out to $x \approx -600$ m, $D^{(3,1)}$ has a subsurface maximum below the offshore surface mixed layer.

Temperature and tracer structure is notably different midday ($\tau_s = 12$ h). Midday, cold $\Delta T^{(1)}$ (Figure 2.2b) is isolated to an alongshore band over roughly $-300 < x < -100$ m, with warmer surf-zone and offshore surface temperature. At $x = -150$ m, surface $\bar{T}$ is 0.31 °C warmer midday than midnight. Along the $y = 50$ m cross-shore transect, the cooler region is over roughly $-500 < x < -150$ m (Figure 2.2d). The $z > -5$ m stratification is elevated midday, relative to midnight (compare Figure 2.2d to Figure 2.2c). $T^{(1)}$ isotherms also have complex cross-shore structure, *e.g.,* the 19.25 °C isotherm deepens from $(x,z) \approx (-475\,\text{m}, -1.5\,\text{m})$ to $(-250, -4)$ and shoals again to $(-150, -2)$ (thick contour, Figure 2.2d). Midday, tracer is present in both relatively warm surf-zone and colder inner-shelf (Figure 2.2b and 2.2h). Midday $D^{(1,1)}$ and $\Delta T^{(1)}$ covariability at offshore surface fronts is similar to midnight. Sub-surface $D^{(1,1)}$ (Figure 2.2h) has more structure and is shallower than midnight $D^{(3,1)}$ (Figure 2.2g), and cross-shore tracer structure is similar to isotherm variability (Figure 2.2d and 2.2h). Offshore of $x \approx -500$ m, $D^{(1,1)}$ also tends toward a sub-surface maximum.

TRC generated eddies create the complex filamentous tracer and temperature patterns onshore of $x \approx -500$ m (Figure 2.2). Midday, eddies in this region heave isotherms and tracer (Figure 2.2d and 2.2h) inducing overturns that are mixed via increased K_v analogously to the

surface cooling induced convective mixed-layer deepening (Burchard and Bolding, 2001; Kumar and Feddersen, 2017b). TRC vertical mixing combined with night-time surface buoyancy loss and depth dependent thermal response strengthen the negative cross-shore surface temperature gradient (Figure 2.2a), deepening the surface mixed layer relative to $x < -500$ m (Figure 2.2c) and leading to midnight $x < -500$ m subsurface tracer maximum ($x < -500$ m, Figure 2.2g). Although SHF heating should stabilize stratification and develop a positive cross-shore temperature gradient, TRC mixing effects are sufficient to overcome SHF heating, causing the persistent mid-day inner-shelf cold band (Figures 2.2b and 2.2d) and sub-surface tracer maximum ($x < -500$ m, Figure 2.2h).

2.3.2 Average Temperature, Circulation and Tracer Structure

The different effects of SHF and SHF+TRC forcing on temperature and cross-shore circulation are evaluated using alongshore and 24 h time mean (3.4)-(2.4) and initialization ensemble averaged streamfunction $\left\langle \bar{\Psi} \right\rangle^{24\text{ h}}$, temperature $\left\langle \bar{T} \right\rangle^{24\text{ h}}$, and vertical eddy diffusivity $\left\langle K_{\mathrm{V}} \right\rangle^{24\mathrm{h}}$ (Figures 2.3a-2.3f). For SHF, the mean overturning stream-function $\left\langle \bar{\Psi} \right\rangle^{24\text{ h}}$ is relatively weak and retains the signature of warming response exchange circulation, with near-surface offshore flow $\left\langle \bar{u}_{\mathrm{L}} \right\rangle^{24\mathrm{h}} \approx -1 \times 10^{-3}$ m s^{-1} for $x > -950$ m (Figure 2.3a). The SHF $\left\langle \bar{T} \right\rangle^{24\text{ h}}$ stratification is decreased above $z = -4$ m (Figure 2.3c) due to diurnal mixed layer development, and offshore of $x = -500$ m isotherms are relatively flat. The SHF+TRC $\left\langle \bar{\Psi} \right\rangle^{24\text{ h}}$ is markedly different owing to TRC driven modification of $\left\langle \bar{T} \right\rangle^{24\text{ h}}$ (Figures 2.3b and 2.3d). The SHF+TRC $\left\langle \bar{\Psi} \right\rangle^{24\text{ h}}$ has a prominent inner-shelf circulation cell offshore of $x \approx -300$ m, with sub-surface offshore directed flow $\left\langle \bar{u}_{\mathrm{L}} \right\rangle^{24\mathrm{h}} < -3 \times 10^{-3}$ m s^{-1} to $x \approx -600$ m (Figure 2.3b). Similar to SHF, the SHF+TRC $\left\langle \bar{T} \right\rangle^{24\text{ h}}$ surface diurnal mixed layer is ≈ 4 m thick for $x \lesssim -1000$ m (Figure 2.3d). However, SHF+TRC isotherm structure differs moving toward shore, with the 19.0 °C isotherm sloping downward and the 19.25 °C rising to the surface near $x = -300$ m (highest two contours in Figure 2.3d).

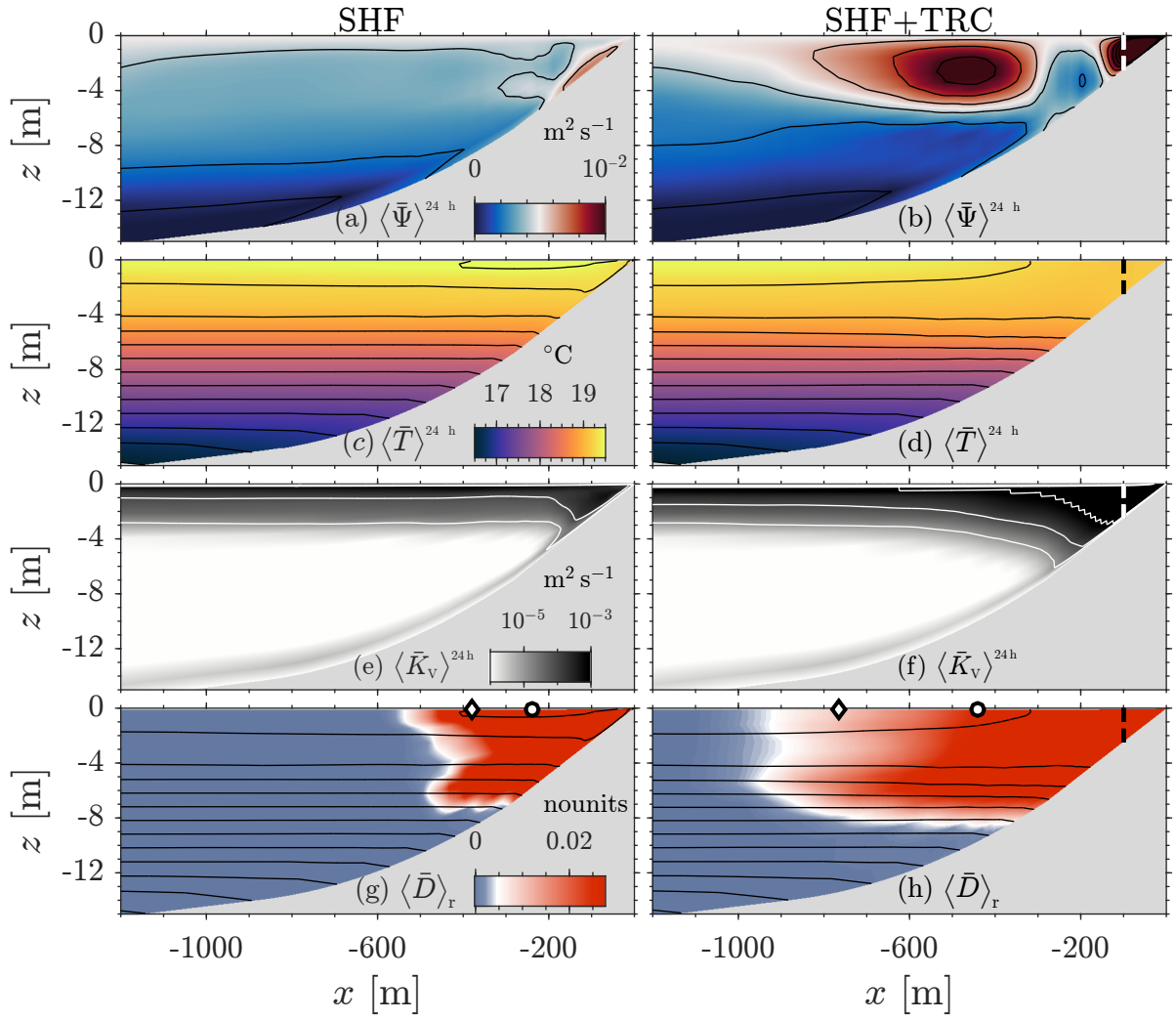

Figure 2.3: SHF (left) and SHF+TRC (right) averaged fields as a function of (x,z). Alongshore and 24 h time mean (3.4)-(2.4) and initialization ensemble averaged (a)-(b) velocity overturning stream-function $\langle\bar{\Psi}\rangle^{24\text{h}}$ contoured at 2×10^{-3} m^{2}s^{-1}; (c)-(d) temperature $\langle\bar{T}\rangle^{24\text{h}}$ contoured at 0.25 C; and vertical eddy viscosity $\langle\bar{K}_\text{v}\rangle^{24\text{ h}}$ with contours at $\{10^{-5},10^{-4},10^{-3}\}$ m^{2}s^{-1}. In (g)-(h) the alongshore mean and initialization and release ensemble averaged tracer concentration $\langle\bar{D}\rangle_\text{r}$ (2.5) is shown at $\tau_\text{r}=24$ h with overlaid $\langle\bar{T}\rangle^{24\text{h}}$ contours from (c)-(d). Shown in (g)-(h) are $x_{50\%}$ (circle) and $x_{90\%}$ (diamond), bounding 50% and 90% of the tracer mass, respectively. For case TRC+SHF (right), $x=-L_\text{sz}$ is indicated with a vertical dashed line.

The SHF and SHF+TRC differences in $\left\langle \bar{\Psi} \right\rangle^{24\text{ h}}$ and $\langle \bar{T} \rangle^{24\text{ h}}$ are largely due to inner-shelf TRC vertical mixing. The relatively flat SHF inner-shelf isotherms (Figure 2.3c) are reflected in the relatively flat $\langle K_\text{V} \rangle^{24\text{h}}$ contours, which deepen at $x \approx -200$ m, where the h becomes comparable to the diurnal mixed layer depth (Figure 2.3e). In contrast, the SHF+TRC $\langle K_\text{V} \rangle^{24\text{h}}$ contours progressively deepen onshore for $x > -1000$ m (Figure 2.3f) and SHF+TRC $\langle K_\text{V} \rangle^{24\text{h}}$ is $10\times$ that of SHF for $x > -300$ m. The shoreward enhanced vertical mixing is due to TRC effects. In TRC-only runs (not shown), K_V increases $>$ 1-order of magnitude onshore of $x = -400$ m, consistent with Kumar and Feddersen (2017b, Fig. 8b). Additionally, the shoreward broadened SHF+TRC isotherms that drive the inner-shelf overturning streamfunction are similar to the TRC-only case (c.f. Fig. 5 in Kumar and Feddersen, 2017c).

These SHF and SHF+TRC differences in $\left\langle \bar{\Psi} \right\rangle^{24\text{ h}}$ and $\langle \bar{T} \rangle^{24\text{ h}}$ result in differences in the alongshore, initialization, and release ensemble averaged tracer $\langle \bar{D} \rangle_\text{r}$ (2.5) at $\tau_\text{r} = 24$ h (Figure 2.3g-h). The 24 h SHF $\langle \bar{D} \rangle_\text{r}$ is nearly all onshore of $x = -500$ m, and offshore of $x \approx -200$ m, SHF $\langle D \rangle_\text{r}$ has a bimodal vertical structure suggesting tracer exchange occurs incrementally at each phase of diurnal thermal exchange. At $\tau_\text{r} = 24$ h, the SHF+TRC $\langle \bar{D} \rangle_\text{r}$ extends offshore to $x = -1000$ m and the SHF+TRC shoreline $\langle \bar{D} \rangle_\text{r}$ is $1/3$ that of SHF. SHF+TRC $\langle \bar{D} \rangle_\text{r}$ has a prominent subsurface tracer maximum for $x < -400$ m, following the 24 h mean streamlines in Figure 2.3b. In TRC only runs (not shown), the subsurface tracer maximum is more pronounced (c.f., Kumar and Feddersen, 2017c, Fig. 2b), relative to SHF+TRC, because SHF-induced surface mixing slightly weakens vertical tracer gradients above $z = -4$ m in Figure 2.3h. Thus, enhanced SHF+TRC exchange relative to SHF-only is likely due to the alongshore and 24 h time mean exchange flow sustained by TRC vertical mixing (Figure 2.3f).

2.3.3 Cross-shore Tracer Mass Evolution

Cross-shore tracer exchange is quantified using the integrated tracer mass onshore of x,

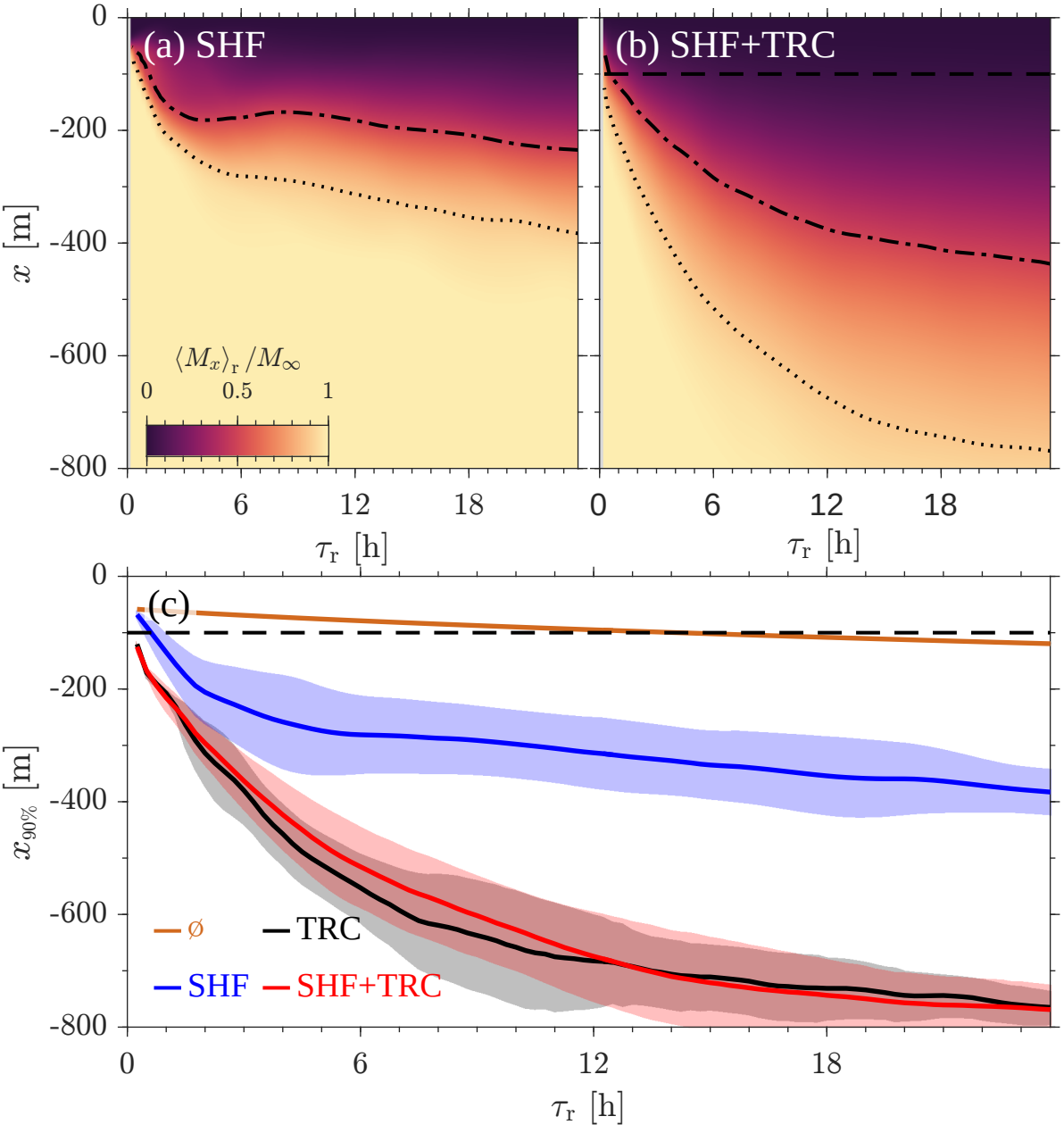

Figure 2.4: Normalized integrated tracer mass $\langle M \rangle_r / M_\infty$ evolution as a function of time since tracer release τ_r and cross-shore x for (a) SHF and (b) SHF+TRC forced runs, with $x_{50\%}$ (dashed-dotted) and $x_{90\%}$ (dotted) contours indicated. (c) Time evolution of $x_{90\%}$ (colored lines) for each forcing case with ± 1 root-mean-square deviation σ from the ensemble average (shading). In (b)-(c) the SZ boundary is indicated by a dashed black line.

$$\langle M \rangle_{\mathrm{r}}(x,\tau_{\mathrm{r}}) = L_y \int_x^0 \int_{-h}^{\eta} \langle \bar{D} \rangle_{\mathrm{r}}(x',z,\tau_{\mathrm{r}})\,\mathrm{d}z\,\mathrm{d}x'; \tag{2.6}$$

where η is the sea-surface. The domain-total tracer mass is denoted M_∞, such that the tracer mass fraction onshore of x is $\langle M \rangle_{\mathrm{r}} / M_\infty$ and two locations are highlighted $x_{50\%}$ and $x_{90\%}$ bounding 50% and 90% of the tracer mass, respectively. At $\tau_{\mathrm{r}} = 24$ h, SHF $x_{50\%} \approx -240$ m and $x_{90\%} \approx -380$ m (circle and diamond, respectively in Figure 2.3g). In contrast, at $\tau_{\mathrm{r}} = 24$ h the SHF+TRC $x_{50\%} \approx -440$ m and $x_{90\%} \approx -760$ m (circle and diamond, respectively (Figure 2.3h), quantifying the stronger SHF+TRC exchange.

The time-dependence of SHF & SHF+TRC ensemble averaged tracer mass fraction $\langle M \rangle_{\mathrm{r}} / M_\infty(x,\tau_{\mathrm{r}})$ (2.6) is shown in Figures 2.4a-2.4b. At $\tau_{\mathrm{r}} = 0$ h, $\langle M \rangle_{\mathrm{r}} / M_\infty = 1$ for $x < -100$ m, as tracer is release over $x > -100$ m. Over time, $\langle M \rangle_{\mathrm{r}} / M_\infty$ contours progress offshore (*e.g.,* $x_{90\%}$ in Figures 2.4a-2.4b) indicating cross-shore tracer transport. The $\langle M \rangle_{\mathrm{r}} / M_\infty$ distribution broadening (*i.e.,* increasing separation between $x_{50\%}$ and $x_{90\%}$) indicate either cross-shore advective straining or cross-shore tracer gradient weakening by mixing, or both. For SHF, the early ($\tau_{\mathrm{r}} \leq 3$ h) cross-shore tracer transport is offshore with $x_{90\%}$ moving at ≈ 2.5 cm s^{-1} (dotted line, Figure 2.4a). Shortly thereafter ($3 < \tau_{\mathrm{r}} < 8$ h), SHF offshore transport slows or even reverses (see $x_{50\%}$ in Figure 2.4a), likely due to flow reversal during warming-to-cooling transition (and vice-versa). After $\tau_{\mathrm{r}} = 12$ h, transport is offshore but slow with $x_{50\%}$ and $x_{90\%}$ moving offshore at < 0.3 cm s^{-1}. For SHF+TRC, early ($\tau_{\mathrm{r}} \leq 3$ h) cross-shore tracer transport is more rapid than for SHF, with $x_{90\%}$ moving at ≈ 3.5 cm s^{-1} (dotted line, Figure 2.4b). In contrast to the SHF reversal, SHF+TRC $\langle M \rangle_{\mathrm{r}} / M_\infty$ contours continuously progress offshore, although at a progressively slower rate.

The bulk cross-shore tracer transport across all forcing cases is evaluated with the $x_{90\%}$ time evolution (Figure 2.4c). In the unforced ø run (brown curve, Figure 2.4c), background diffusive mixing induces weak exchange, and $x_{90\%} > -110$ m, indicating strong tracer confinement. In contrast, over 24 h, SHF thermally driven exchange draws tracer 3× farther offshore (blue, Figure 2.4). For TRC and SHF+TRC, tracer mass evolution is statistically indistinct, as evidenced

by the overlap in $x_{90\%} \pm \sigma_{x_{90\%}}$ (shading in Figure 2.4c), where $\sigma_{x_{90\%}}$ is the root-mean-square deviation from the ensemble average, further indicating that the SHF+TRC forced exchange is dominated by TRC effects. After 24 h, the TRC and SHF+TRC $x_{90\%}$ extend twice as far offshore as that for SHF (Figures 2.3g-2.3h and 2.4c), demonstrating that for the wave, stratification, and SHF forcing regime here, the TRC exchange mechanism is stronger than the diurnal SHF exchange mechanism.

2.4 Discussion and Conclusions

2.4.1 Quantifying Exchange: Tracer Flux & Velocity Derived Estimates

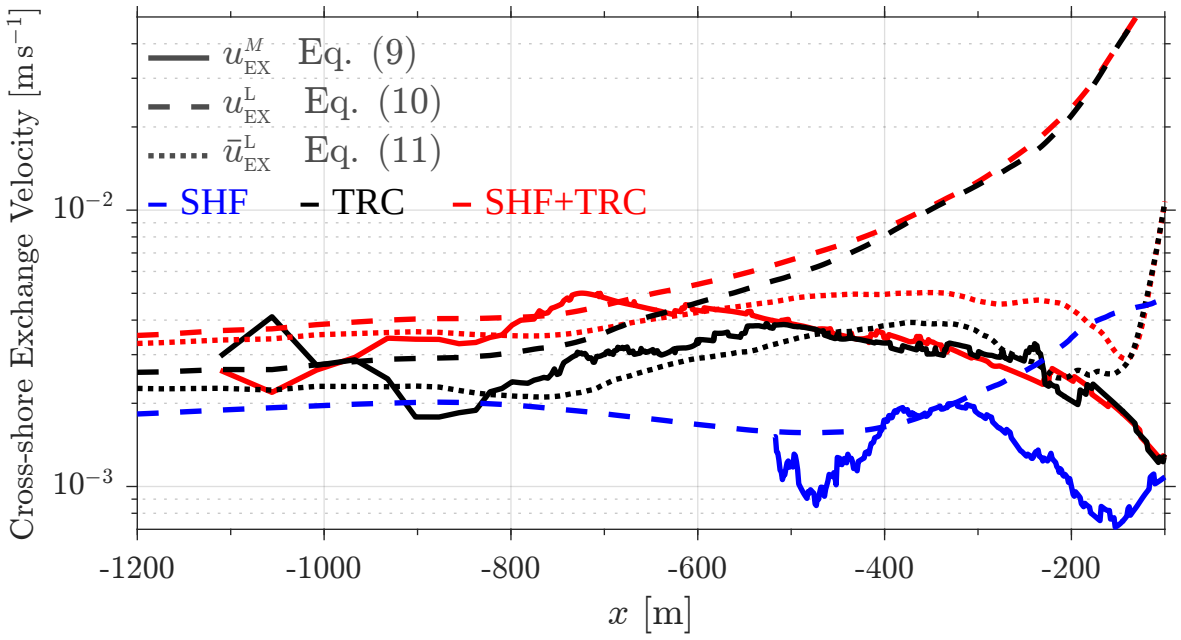

Figure 2.5: Cross-shore exchange velocity u_{EX} versus cross-shore coordinate x for SHF (blue), TRC (black), and SHF+TRC (red) simulations. Three definitions of u_{EX} are used: u^M_{EX} (solid) derived from tracer mass balances (2.9), u^L_{EX} (dashed) defined using offshore Lagrangian velocities (3.7) and $\bar{u}^L_{EX}$ defined using alongshore mean offshore Lagrangian velocities (2.11). All exchange velocities are 24 h time mean and initialization ensemble averaged, u_{EX} is also ensemble averaged over all releases and is only computed where $\partial \langle M \rangle_r / \partial x > 10^{-8}$.

Cross-shore tracer transport $\mathcal{T}_x$ (*e.g.,* sediment, heat, larvae, or pollutants) is a fundamental

quantity of interest in cross-shore exchange studies (*e.g.,* Hally-Rosendahl et al., 2015). In the absence of sources/sinks, alongshore averaged tracer transport may be estimated from the evolution of tracer mass $\langle M \rangle_{\mathrm{r}}$ (2.6) via (Hally-Rosendahl et al., 2015; Feddersen et al., 2016),

$$\mathcal{T}_x(x,\tau_{\mathrm{r}}) = \frac{\partial \langle M \rangle_{\mathrm{r}}}{\partial \tau_r}. \tag{2.7}$$

Cross-shore transport potential is often represented with an exchange velocity u_{EX}, which has various definitions (*e.g.,* MacCready, 2011; Suanda and Feddersen, 2015). Conceptually, transport driven by an idealized exchange flow is parameterized as (*e.g.,* Hally-Rosendahl et al., 2015),

$$\mathcal{T}_x \propto u_{\mathrm{EX}} L_y (\tilde{h}\tilde{D}), \tag{2.8}$$

where $\tilde{h} = h + \eta$ is the total water depth, and $\tilde{D}$ the depth average tracer concentration.

Although u_{EX} is a useful metric, the assumptions in (2.8) grossly approximate the tracer conservation equation governing $\mathcal{T}_x$; as such, u_{EX} estimates will depend on definition. Here, two unique u_{EX} definitions are examined. Leveraging (2.7) and substituting $L_y(\tilde{h}\tilde{D}) = \partial \langle M \rangle_{\mathrm{r}} / \partial x$ in (2.8), yields a tracer-derived exchange velocity,

$$u^M_{\mathrm{EX}} = \left\langle \frac{\partial \langle M \rangle_{\mathrm{r}}}{\partial \tau_{\mathrm{r}}} \left(\frac{\partial \langle M \rangle_{\mathrm{r}}}{\partial x} \right)^{-1} \right\rangle^{24\ \mathrm{h}}, \tag{2.9}$$

where the outer average $\langle \rangle^{24\ \mathrm{h}}$ is over $0 < \tau_{\mathrm{r}} \leq 24$ h. Although u^M_{EX} encapsulates recirculation, tracer presence is required and (2.9) is only evaluated for $\partial \langle M \rangle_{\mathrm{r}} / \partial x > 10^{-8}$ m^2, or $\tilde{h}\tilde{D} > 10^{-5}$ m. As an alternative, a Lagrangian velocity derived exchange u^L_{EX} is based on cross-shore flow alone (*e.g.,* MacCready, 2011; Suanda and Feddersen, 2015),

$$u^L_{\mathrm{EX}} = \left\langle \overline{\frac{2}{h+\eta} \int_{-h}^{\eta} u_{\mathrm{L}}^{-} \, dz} \right\rangle^{24\ \mathrm{h}}, \tag{2.10}$$

where the offshore Lagrangian velocity u_{L}^{-} has onshore values set to zero, and the alongshore average (3.4), 24 h time average (2.4) and initialization ensemble average are applied. The Lagrangian velocity derived u_{EX}^{L} can be estimated over the entire domain. The factor of 2 in (3.7) recovers (2.8) for 2-layer exchange flow; and makes (3.7) analogous to estuarine exchange flow (*e.g.,* Lerczak et al., 2006; MacCready, 2011).

The SHF u_{EX}^{M} is a factor of $1/3$ weaker than that for TRC and SHF+TRC (solid, Figure 2.5) with TRC and SHF+TRC u_{EX}^{M} differing by $< 10\%$ for $x < -200$ m, peaking near 5×10^{-3} m s^{-1}. This confirms findings of Section 2.3.3. Velocity derived u_{EX}^{L} is similarly weaker for SHF than for both TRC and SHF+TRC (dashed curves, Figure 2.5) and TRC and SHF+TRC u_{EX}^{L} are largely similar. For TRC and SHF+TRC, both u_{EX}^{M} and u_{EX}^{L} are consistent over $x < -500$ m, yet deviate onshore of $x = -400$ m, with u_{EX}^{L} exceeding $10 \times u_{\mathrm{EX}}^{M}$ at $x = -L_{\mathrm{sz}}$ m.

For TRC and SHF+TRC, inner-shelf eddy velocities increase toward $x = -L_{\mathrm{sz}}$, and the growing difference between u_{EX}^{M} and u_{EX}^{L} for $x > -400$ (Figure 2.5) is likely due to eddy recirculation that bias high u_{EX}^{L}. To account for recirculation in u_{EX}^{L}, an exchange factor (< 1) often is introduced in (3.7) that depends on x and hydrodynamics (Lemagie and Lerczak, 2015; Suanda and Feddersen, 2015). Previous estimates of the exchange factor for surf-zone to inner-shelf transport range 0.2-0.3 (Suanda and Feddersen, 2015; Smith and Largier, 1995; Dalrymple et al., 2011), consistent with the differences between u_{EX}^{M} and u_{EX}^{L} for $x > -400$ m.

An exchange velocity that removes eddy effects is based on the alongshore mean Lagrangian velocity (*e.g.,* MacCready, 2011; Lerczak et al., 2006),

$$\bar{u}_{\mathrm{EX}}^{L} = \left\langle \frac{2}{h+\bar{\eta}} \int_{-h}^{\bar{\eta}} \bar{u}_{\mathrm{L}}^{-} \, d\bar{z} \right\rangle^{24\ \mathrm{h}}, \tag{2.11}$$

where the alongshore average (3.4), 24 h and initialization ensemble average (2.4) are applied. Thus, for non-eddying SHF, estimates of u_{EX}^{L} and $\bar{u}_{\mathrm{EX}}^{L}$ are indistinguishable (Figure 2.5). The TRC and SHF+TRC $\bar{u}_{\mathrm{EX}}^{L}$ (dotted curves, Figure 2.5) are much lower than u_{EX}^{L} over $x > -400$ m,

converging offshore of $x = -600$ m, indicating that the transition from eddy dominated to alongshore mean dominated transport regimes occurs at $x \approx -500$ m (see Figure 2.2). The similar shape of $\bar{u}^L_{\mathrm{EX}}$ and u^M_{EX} for $x < -200$ m indicates that enhanced 24 h tracer exchange for TRC and SHF+TRC is primarily due to an alongshore mean exchange flow. Horizontal eddies associated with TRCs are inhomogeneous in x, which induces a long-time subdiffusive regime (*e.g.,* Spydell et al., 2019), which may explain why eddy-induced transport is weak. The consistently larger TRC and SHF+TRC u_{EX} estimates relative to SHF out to $x = -1200$ m or $-12L_{\mathrm{sz}}$ (2.5) confirms that the TRC baroclinic exchange mechanism is dominant for this wave and SHF forcing regime.

2.4.2 Concluding Remarks

For typical early-Fall Southern California conditions, the transient rip-current (TRC) exchange mechanism is stronger than surface heat flux (SHF) induced thermally driven exchange out to at least $x = -1200$ m or $-12L_{\mathrm{sz}}$, significantly offshore of the 100 m wide surf-zone. Combined SHF forcing with TRCs does not significantly modify the bulk inner-shelf cross-shore tracer exchange induced by TRCs. Inner-shelf TRC vertical mixing with stratification generates an alongshore and time mean inner-shelf overturning circulation with sub-surface offshore directed flow. For quasi-instantaneous surf-zone tracer release, this sub-surface baroclinic pathway is well represented by an exchange velocity derived from the alongshore mean and offshore directed Lagrangian velocity. Including horizontal eddies in exchange velocity estimates over predicted inner-shelf tracer transport, due to recirculation.

The TRC baroclinic cross–inner-shelf exchange flow mechanism critically depends on inner-shelf stratification. Here, the diurnal mixed layer depth does not extend beyond the TRC vertical mixing depth. The baroclinic exchange mechanism may be impacted if enhanced SHF forcing deepens the diurnal mixed layer relative to the TRC mixing depth. Here the diurnal net surface heat flux is zero. A shift toward net-cooling annihilating stratification would reduce transient rip-current exchange. Thus, in Mediterranean climates the potential for TRC inner-

shelf exchange will vary seasonally with wave and stratification changes. For relatively stable diurnal SHF forcing (*e.g.,* tropical climates), episodic incidence of swell, which at times dominate flow and modulate shallow reef thermal response (*e.g.,* Hench et al., 2008; Davis et al., 2011), may diminish TRC exchange relative to persistent diurnal thermally driven exchange. Other mechanisms influencing inner-shelf stratification and hydrodynamics, *e.g.,* wind, internal waves, and tides, are also likely to impact the TRC baroclinic exchange pathway. The ubiquity of coastline with a surf-zone and stratified inner-shelf would suggest that TRC exchange is common, motivating further study.

Acknowledgements

This work was funded under the CSIDE grant by the National Science Foundation (NSF OCE-1459389), and student funding was provided through the NSF-GRFP. This work used the Extreme Science and Engineering Discovery Environment (XSEDE) Comet at SDSC through allocation TG-OCE180014, which is supported by National Science Foundation grant number ACI-1548562. We thank Sarah N. Giddings, Geno T. Pawlak, Gregory Sinnett, and Aryan Safaie for stimulating discussion and feedback from 3 anonymous reviewers that improved this work. In accordance with AGU policy, presented data are available at https://sandbox.zenodo.org/record/507448 with the larger dataset digitally archived at https://doi.org/10.6075/J0WM1BSJ (Grimes et al., 2020b). Please email the corresponding author dgrimes@ucsd.edu for further details. Chapter 2, in full, is a reprint of the paper Tracer Exchange Across the Stratified Inner-Shelf Driven by Transient Rip-Currents and Diurnal Surface Heat Fluxes in Geophysical Research Letters: Oceans by D. J. Grimes, F. Feddersen and N. Kumar in 2020. The dissertation author was the primary investigator and author of this paper.

Chapter 3

The self-similar stratified inner-shelf response to transient rip-current induced mixing.

Abstract

The stratified inner-shelf response to surf-zone generated transient rip-currents (TRC) is examined with coupled surf-zone and inner-shelf idealized simulations with uniform initial thermal stratification $\mathrm{d}T_0/\mathrm{d}z$ [$^\circ\mathrm{C\,m^{-1}}$] (or N_0^2) varying from 0 (unstratified) to 0.75 $^\circ\mathrm{C\,m^{-1}}$ (highly stratified). Domain integrated eddy kinetic energy equilibrates in 1 h, and the mean depth-integrated cross-shore eddy kinetic energy flux is independent of $\mathrm{d}T_0/\mathrm{d}z$ and decays to near-zero within $4L_{\mathrm{sz}}$ (surf-zone width $L_{\mathrm{sz}} = 100$ m). TRC-driven mixing on the inner-shelf (onshore of $\approx 3L_{\mathrm{sz}}$) induces a cross-shore density gradient, driving a 3-layer cross-shore exchange flow at $-5L_{\mathrm{sz}} < x < -2L_{\mathrm{sz}}$ that increases with N_0, consistent with intrusive stratified gravity current. Offshore of $5L_{\mathrm{sz}}$, isotherms have characteristic slope f/N_0 and the alongshore velocity is largely geostrophic, scaling with N_0. The TRC-mixing region mostly (90%) increases

background potential energy (bpe) and also available (ape, 10%) potential energy, with efficiency that scales with $(\mathrm{d}T_0/\mathrm{d}z)^{3/4}$. The sorted temperature anomaly ΔT_s indicates TRC-mixing reduces stratification 50% near zero-crossing depth d_s that, based on an idealized well-mixed wedge, scales with $(\mathrm{d}T_0/\mathrm{d}z)^{-1/4}$. Sloping isotherms induce ape reservoirs above and below d_s and an idealized intrusion scenario qualitatively scales the simulated ape structure. Non-dimensional mean stratification and cross-shore velocity vertical profiles collapse with non-dimensional vertical coordinate z/d_s. Stratified inner-shelf circulation response to TRC-driven mixing is self-similar and with key dimensional parameters N_0, d_s, L_{sz} and eddy kinetic energy flux out of the surf-zone.

3.1 Introduction

The inner-shelf is influenced by myriad processes over broad spatial and temporal scales (*e.g.,* Brink, 2016), that regulate nutrient cycling and larval recruitment (Washburn and McPhee-Shaw, 2013; Morgan et al., 2018) and coastal water quality (Boehm et al., 2017). On sub-tidal time-scales, inner-shelf stratification and circulation are modified by wind-driven mixing and cross-shore transport (upwelling/downwelling) (*e.g.,* Lentz and Fewings, 2012), and modulated by tidal mixing (*e.g.,* Castelao et al., 2010). On both diurnal and longer time-scales, solar heating and surface buoyancy fluxes regulate inner-shelf stratification and circulation (*e.g.,* Monismith et al., 2006; Molina et al., 2014). Internal waves and tides induce cross-shelf exchange and vertical mixing on time-scales ranging from 10 min to 12 h (*e.g.,* Walter et al., 2012; Sinnett et al., 2018). On relatively fast time-scales ($<$ 1 h), strong and concentrated offshore directed rip-currents enhance exchange between surf-zone and inner-shelf (Clark et al., 2010; Brown et al., 2009; Reniers et al., 2010). After several hours ($>$ 6 h and $<$ 48 h), transient rip-current (TRC) enhanced vertical mixing on the stratified inner-shelf drives inner-shelf circulation (Kumar and Feddersen, 2017b,c). Ultimately, a range of processes contribute to both the background

inner-shelf conditions and variability. However, the stratified inner-shelf response to transient rip-currents remains poorly understood.

Rip-currents are surf-zone generated strong offshore flows extending onto the inner-shelf and are classified in various ways (c.f. Castelle et al., 2016). On alongshore uniform coasts, transient rip-currents (TRC) are defined as ephemeral rip-currents with no preferred alongshore formation site (Dalrymple et al., 2011). TRC generation is due to coalescence of surf-zone vorticity forced by short-crested breaking waves (Feddersen, 2014; Johnson and Pattiaratchi, 2006; Peregrine, 1998). In contrast to TRCs, bathymetrically controlled rip-currents (BRC) develop through coupling of shoaling waves and surf-zone currents with underlying bathymetry, and preferentially form in rip-channels (*e.g.,* MacMahan et al., 2010).

In the surf-zone, TRCs are predominately barotropic (depth uniform), with strength and occurrence varying with incident wave characteristics, particularly wave directional spread σ_θ, and beach slope (*e.g.,* Johnson and Pattiaratchi, 2006). In depth averaged TRC resolving simulations, TRC driven barotropic exchange velocity is self-similar (Suanda and Feddersen, 2015), and increased with directional spread σ_θ. In a depth resolving model, TRC-induced eddies enhance exchange across the unstratified inner-shelf relative to non-TRC resolving (*i.e.,* phase averaged) simulations (Kumar and Feddersen, 2017a).

The inner-shelf is often stratified, and TRC-enhanced vertical mixing decreases near-shore stratification, causing modeled isopycnals to broaden toward shore and increase shoreward depth integrated potential energy (Kumar and Feddersen, 2017b). Available potential energy reservoirs associated with cross-shore sloping isotherms, *e.g.,* due to upwelling favorable winds or estuarine buoyancy and vertical mixing gradients (MacCready and Giddings, 2016), drive baroclinic circulation. Modeled TRC mixing induces a baroclinic cross-shore exchange flow that transports surf-zone released passive tracer within a low-stratification offshore intrusion across the inner-shelf (Kumar and Feddersen, 2017c). In contrast, unstratified simulations had tracer confined to shore and vertically well-mixed. Farther offshore of the TRC eddy dominated region,

sloping isopycnals approached thermal wind balance after 42-48 h ($\approx 2\,f^{-1}$) with f the Coriolis frequency (Kumar and Feddersen, 2017b).

Sloping isopycnals are commonly observed on the mid- to outer-shelf, where thermal wind shear approximately balances the baroclinic pressure gradient. In wind driven upwelling/downwelling regimes, geostrophic interior (away from boundaries) isopycnal slope $\mathrm{d}z/\mathrm{d}x$ may vary weakly with depth and are characterized by the local Rossby deformation radius ($L_\mathrm{R} = NH/f$), or $\mathrm{d}z/\mathrm{d}x \sim H/L_\mathrm{R} = f/N$, with buoyancy frequency N, and depth scale H (*e.g.,* Lentz and Chapman, 2004). Mid-shelf tidal mixing also drive sloping isopycnals that tend to broaden toward shallow water with aspect ratio scaling f/N, and forming an offshore mixed fluid intrusion (*e.g.,* Garrett and Loder, 1981; van Heijst, 1986). The relationship between TRC-induced vertical mixing and inner-shelf isopycnal slopes, or the resulting available potential energy, is unknown.

As the baroclinic TRC exchange mechanism relies on mixing driven sloping isopycnals, changes to the background inner-shelf stratification are expected to modify TRC driven mixing and exchange. Kumar and Feddersen (2017b,c) only considered a single spatially uniform thermal stratification of $\mathrm{d}T_0/\mathrm{d}z = 0.25\ ^\circ\mathrm{C\,m^{-1}}$, characteristic of summer-fall in Southern California, and neglected other forcing mechanisms that might affect mixing and stratification. Internal waves and diurnal solar heating/cooling can significantly modify vertical and cross-shore buoyancy gradients over time-scales of hours (*e.g.,* Omand et al., 2011; Grimes et al., 2020a; Sinnett et al., 2018). However, based on an ensemble of idealized simulations that included a diurnal heating/cooling cycle, diurnal averaged TRC exchange was similar with and without surface heat flux and dominant relative to diurnal averaged thermally driven exchange (Grimes et al., 2020c). The weak surface heat flux modulation on TRC exchange was potentially due to shallow diurnal mixed layer relative to the TRC induced mixing. However, this detail was not addressed further, and the relationship between TRCs, stratification, and inner-shelf response not determined.

Herein, the stratified inner-shelf response to surf-zone generated TRCs is evaluated based

on idealized 3D coupled surf-zone/inner-shelf simulations with varying initial stratification $\mathrm{d}T_0/\mathrm{d}z$ (Section 3.2). The intermediate time-scale inner-shelf response, from 24-48 h, is quantified using alongshore and time mean statistics (Section 3.2.3). The effect of initial stratification on inner-shelf mean and eddy statistics are described qualitatively, with scalings for bulk inner-shelf circulation response presented in Section 3.3. In Section 3.4, the eddy kinetic energy distribution and relation between cross-shore kinetic energy flux and the background and available potential energy growth and distribution with varying $\mathrm{d}T_0/\mathrm{d}z$ are evaluated. The self-similar vertical structure of inner-shelf mean stratification and cross-shore velocity is related to the structure of TRC mixing induced change in background potential energy in Section 3.5.1. A scaling for background potential energy structure and qualitative description of model cross-shore available potential energy distribution are described in Section 3.5.2 and 3.5.3 using an idealized schematic representation of TRC mixing effects on stratified inner-shelf derived in 3.6 and 3.6. These results are extrapolated to varying incident wave properties using existing TRC-induced exchange velocity scalings in Section 3.5.4. Lastly, results are summarized and contextualized with other inner-shelf processes in Section 3.6.

3.2 Methods

3.2.1 Modeling

The COAWST modeling framework is used here (Warner et al., 2010) with methods similar to those used by Kumar and Feddersen (2017a,b,c) & Grimes et al. (2020c). The hydrodynamic model ROMS (Shchepetkin and McWilliams, 2005) is 1-way coupled (wave effects on currents) to the spectral wave model SWAN (Booij et al., 1999). ROMS is also supplied surf-zone depth averaged breaking wave rotational body forcing from phase-resolving wave model funwaveC (Kumar and Feddersen, 2017a). Rotational breaking-wave forcing generates surf-zone vertical vorticity and spontaneous formation of transient rip-currents, in a manner

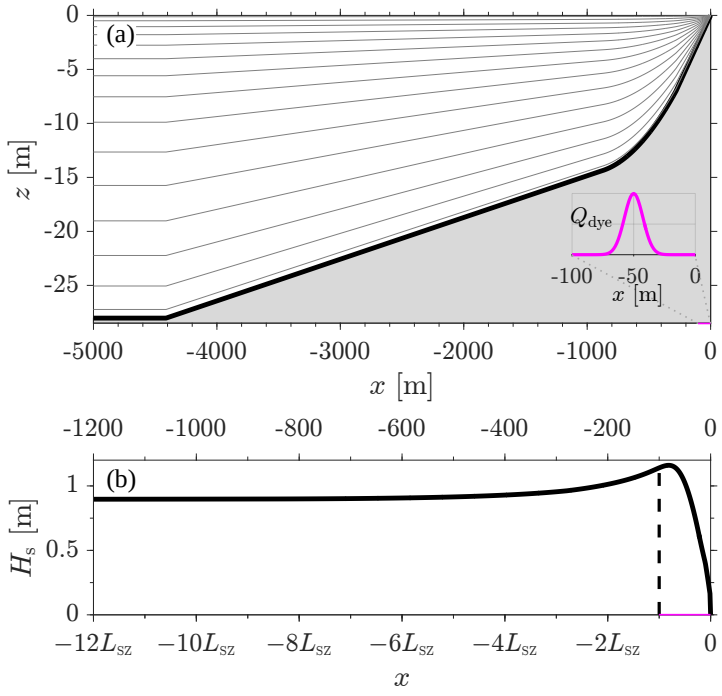

Figure 3.1: (a) Cross-shore (x) model domain with depth $z{=}{-}h(x)$ in black and ROMS σ-layers in gray. The inset illustrates the x-distribution of mid-surf-zone tracer bottom flux Q_{dye} centered on $x{=}{-}50$ m or $x{=}{-}L_{\mathrm{sz}}/2$. (b) SWAN significant wave height $H_{\mathrm{s}}(x)$ with the surf-zone boundary, $x{=}{-}L_{\mathrm{sz}}{=}{-}100$ m, indicated by vertical dashed black line. The lower x-axis of (b) is measured in surf-zone width L_{sz} with the surf-zone and tracer release region from inset (a) indicated by magenta colored x-axis. Note the cross-shore ranges differ in (a) and (b).

consistent with observations (Feddersen, 2014).

The model cross-shore (x) domain extends $L_x = 5$ km offshore (Figure 3.1a), with $x = 0$ at the shoreline and positive onshore. Close to shore, $x \geq -250$ m, bathymetry $h(x)$ has constant slope $\beta_{\mathrm{SZ}} = 0.025$ that transitions quadratically to $\beta_{\mathrm{IS}} = 0.004$ offshore of $x = -1000$ m. The domain is alongshore (y) uniform and periodic, spanning $L_y = 1$ km. The vertical coordinate $z = 0$ at the mean water-level with positive upwards. Fifteen ROMS terrain following vertical σ coordinates are used, and near-surface resolution is slightly increased offshore (gray, Figure 3.1a).

Tracer vertical eddy diffusivity K_{v} is determined using the two equation $k-\varepsilon$ turbulence closure with Kantha and Clayson (1994) stability functions (Warner et al., 2005). In the surf-zone, 15% of wave energy dissipation is supplied as surface turbulent kinetic energy flux, consistent with

previous surf-zone modeling studies (*e.g.,* Rodriguez et al., 2018). The background horizontal diffusivity $K_{\mathrm{H}} = 0.01$ m^2 s^{-1} is increased $20\times$ within the surf-zone, to account for unresolved bore/roller dispersion, but remains $\approx 5\times$ smaller than observed surf-zone rotational eddy driven stirring (*e.g.,* Clark et al., 2010, 2011). A spatially uniform quadratic bottom drag $C_{\mathrm{d}} = 0.0025$ and Coriolis parameter $f = 7.7 \times 10^{-5}$ s^{-1} are used.

Simulated wave conditions are typical of Southern California in summer-fall with normally incident $H_{\mathrm{sz}} \approx 1$ m significant wave height at breaking (Figure 3.1b), peak period $\mathrm{T_p} = 10$ s and directional spread $\sigma_\theta = 10$ deg. The resulting surf-zone, region of depth-limited wave dissipation, is confined to $-L_{\mathrm{sz}} \leq x \leq 0$ where the surf-zone width $L_{\mathrm{sz}} = 100$ m is used as a characteristic cross-shore length-scale (Figure 3.1b).

A series of 18 simulations are performed varying the initial stratification $\mathrm{d}T_0/\mathrm{d}z = \{0, 0.0125, 0.025, 0.05 : 0.05 : 0.75\}^\circ$C m^{-1} to evaluate how inner-shelf stratification affects transient rip-current mixing and induced inner-shelf circulation. The 48 h long simulations are initialized from rest, with spatially uniform and constant initial stratification $\mathrm{d}T_0/\mathrm{d}z$,

$$T(z, t=0) \equiv T_0(z) = T_{\mathrm{ref}} + z\frac{\mathrm{d}T_0}{\mathrm{d}z}, \tag{3.1}$$

with surface reference temperature $T_{\mathrm{ref}} = 20$ °C. A linear temperature dependent equation of state is used, with initial condition,

$$\rho(z, t=0) \equiv \rho_0(z) = \rho(1 - \alpha(T_0(z) - T_\rho)), \tag{3.2}$$

with constant reference density $\rho = 1027$ kg m^{-3} at T_ρ, and constant thermal expansion coefficient $\alpha = 1.7 \times 10^{-4}$ C^{-1}. Offshore boundary ($x = -5$ km) temperature is clamped to the initial condition $T_0(z)$. A zero mass flux offshore boundary condition is applied at each z-level. The surface and bottom boundaries are adiabatic and surface stress is zero, *i.e.,* no wind or surface heat fluxes. Similar to Grimes et al. (2020c), a series of 4 surf-zone passive tracer releases occur at 6 h

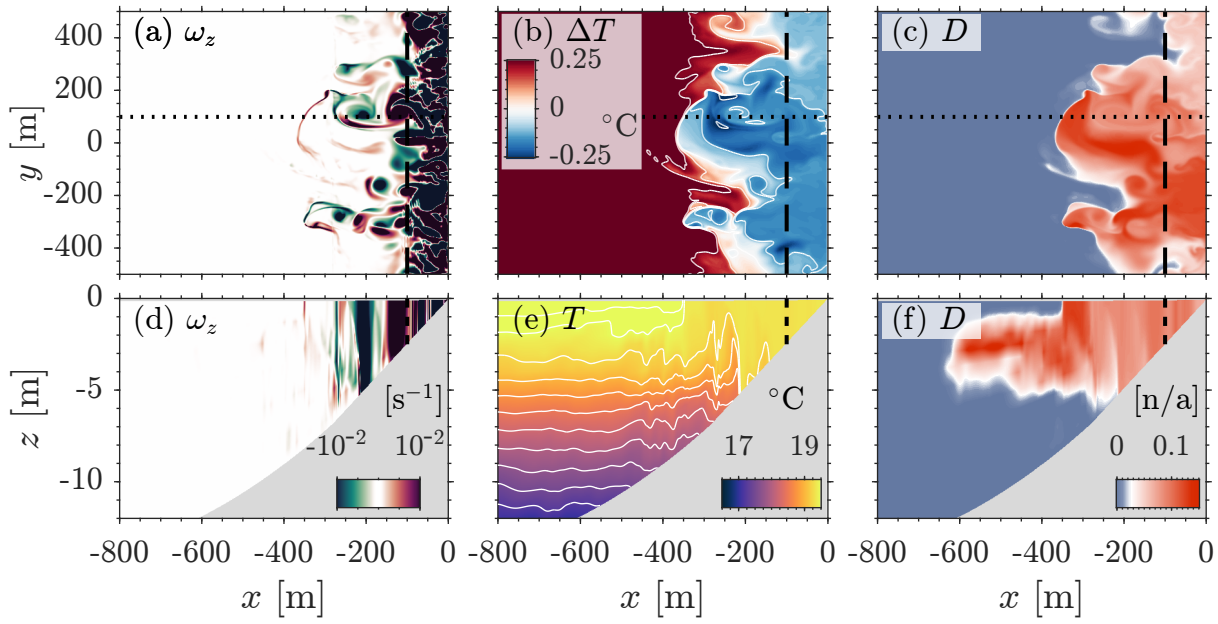

Figure 3.2: Model time t=12 h (a,d) vertical component of relative vorticity ω_z, (b) surface temperature anomaly ΔT relative to the x=−150 m alongshore mean, (e) subsurface temperature T and (c,f) tracer D. Surface panels (a)-(c) are functions of (x,y) and sub-surface panels (d)-(f) are functions of (x,z) at y=100 m, as indicated with black dotted line in (a)-(c). Tracer D in (c,f) 6 h has elapsed since tracer release (c.f. Grimes et al., 2020c). The L_{sz}=100 m wide surf-zone is delimited with vertical dashed black line, and in (d)-(f) the bottom is gray.

intervals with cross-shore distribution of tracer bottom flux Q_{dye} (magenta) shown in Figure 3.1a. Tracer evolution is not analyzed here. The full archive of raw model output and results presented herein are available from the UCSD Library Digital Collection (doi: TBD).

3.2.2 Description of Model Snapshot

An example snapshot from $dT_0/dz = 0.25$ °C m^{-1} simulation is presented to motivate the averaging methods used in analyzing the range of dT_0/dz considered. At model time $t = 12$ h, surf-zone generated TRC-induced eddies occupy the region $x > -4L_{sz}$ (Figure 3.2a), *e.g.,* at $(x = -2L_{sz}, y = 100$ m) in Figure 3.2a and 3.2d, with peak vertical vorticity of $O(100\ f)$. Near the surf-zone, TRC eddies are barotropic and temperature T and surf-zone $t = 6$ h released tracer

D are vertically well-mixed, *e.g.,* $x \geq -2.5L_{sz}$ in Figure 3.2e-3.2f. As such, the complex swirling and stirring patterns in surface T and D are representative of the depth averaged TRC eddy induced variability for $x > -3L_{sz}$ (Figure 3.2b-c).

Offshore of $3L_{sz}$, inner-shelf TRC-induced eddies have more vertical structure, and filamentous vorticity features are also present, *e.g.,* feature at $x = -3.5L_{sz}$ in Figure 3.2a and 3.2d. Along $y = 100$ m, vertical isotherm displacements of >1 m that vary with depth occur out to $x = -6L_{sz}$ (Figure 3.2e). The largest vertical displacements are offshore of a strong anticyclonic eddy (Figure 3.2d), linking TRC-induced eddies to development of T inversions and mixing. The TRC-enhanced vertical mixing generates alongshore averaged cross-shore temperature gradients and baroclinic inner-shelf circulation (*e.g.,* Kumar and Feddersen, 2017b). Surf-zone released tracer D is transported offshore sub-surface over $-6L_{sz} < x < -4L_{sz}$ by an alongshore averaged baroclinic (x,z)-exchange flow (Figure 3.2f; c.f. Kumar and Feddersen, 2017c; Grimes et al., 2020c).

3.2.3 Averaging and Analysis

To analyze TRC-induced eddy variability separately from the effects of enhanced vertical mixing on mean inner-shelf temperature and circulation, dynamical variables are decomposed into alongshore mean and perturbation components,

$$c(x,y,z,t) = \bar{c}(x,z,t) + c'(x,y,z,t), \tag{3.3}$$

where the alongshore mean of generic variable c is,

$$\bar{c}(x,z,t) = L_y^{-1} \int_0^{L_y} c(x,y',z,t)\, \mathrm{d}y', \tag{3.4}$$

and c' is the alongshore perturbation or eddy component. Following a < 6 h spin-up period, the simulated inner-shelf TRC-eddy statistics approach stationarity with low-frequency variability, analogous to surf-zone very-low frequency Eulerian current variability (*e.g.,* Elgar et al., 2019; Elgar and Raubenheimer, 2020). The alongshore mean statistics evolve continuously due to irreversible mixing (*e.g.,* Grimes et al., 2020c). Aspects of sections 3.3-3.4 analysis use a time average from $t = 24$-48 h,

$$\langle c \rangle (x,z) = (24 \text{ h})^{-1} \int_{24 \text{ h}}^{48 \text{ h}} c(x,z,t') \, \mathrm{d}t', \tag{3.5}$$

to diagnose stratified inner-shelf response to TRCs. The chosen time-averaging period begins after and spans an inertial period ($> f^{-1} \approx 23$ h). Hereafter, "mean" will refer to both alongshore average (3.4) and 24-48 h time average (3.5), unless otherwise noted.

3.3 Results: Inner-Shelf Response to TRC-Eddy Forcing

3.3.1 Mean Inner-Shelf Response with Varying Stratification

A qualitative picture of how varying stratification affects TRC-induced inner-shelf mixing, temperature and circulation is revealed by comparing the mean, alongshore (3.4) and 24-48 h time averaged (3.5), (x,z)-structure of tracer vertical eddy diffusivity $\langle \bar{K}_\mathrm{v} \rangle$, temperature $\langle \bar{T} \rangle$, streamfunction $\langle \bar{\Psi} \rangle$, and alongshore velocity $\langle \bar{v} \rangle$ at three levels of stratification $\mathrm{d}T_0/\mathrm{d}z = \{0.025, 0.1, 0.25\}$ °C m^{-1} (Figure 3.3). In the region significantly impacted by TRC-induced eddy activity, $x > -4L_\mathrm{sz}$ and denoted the TRC region, $\langle \bar{K}_\mathrm{v} \rangle$ is elevated, increasing from 10^{-6} m^2 s^{-1} offshore to 10^{-2} m^2 s^{-1} in the surf-zone (Figure 3.3a). Increasing stratification (left-to-right in Figure 3.3) decreases the inner-shelf ($x < -L_\mathrm{sz}$) $\langle \bar{K}_\mathrm{v} \rangle$ (Figure 3.3a-3.3c), confining the elevated mixing region to a smaller (x,z)-area. The elevated inner-shelf $\langle \bar{K}_\mathrm{v} \rangle$ is due to both temperature (density) inversions and shear driven mixing. The $\langle \bar{K}_\mathrm{v} \rangle$ reduction with $\mathrm{d}T_0/\mathrm{d}z$

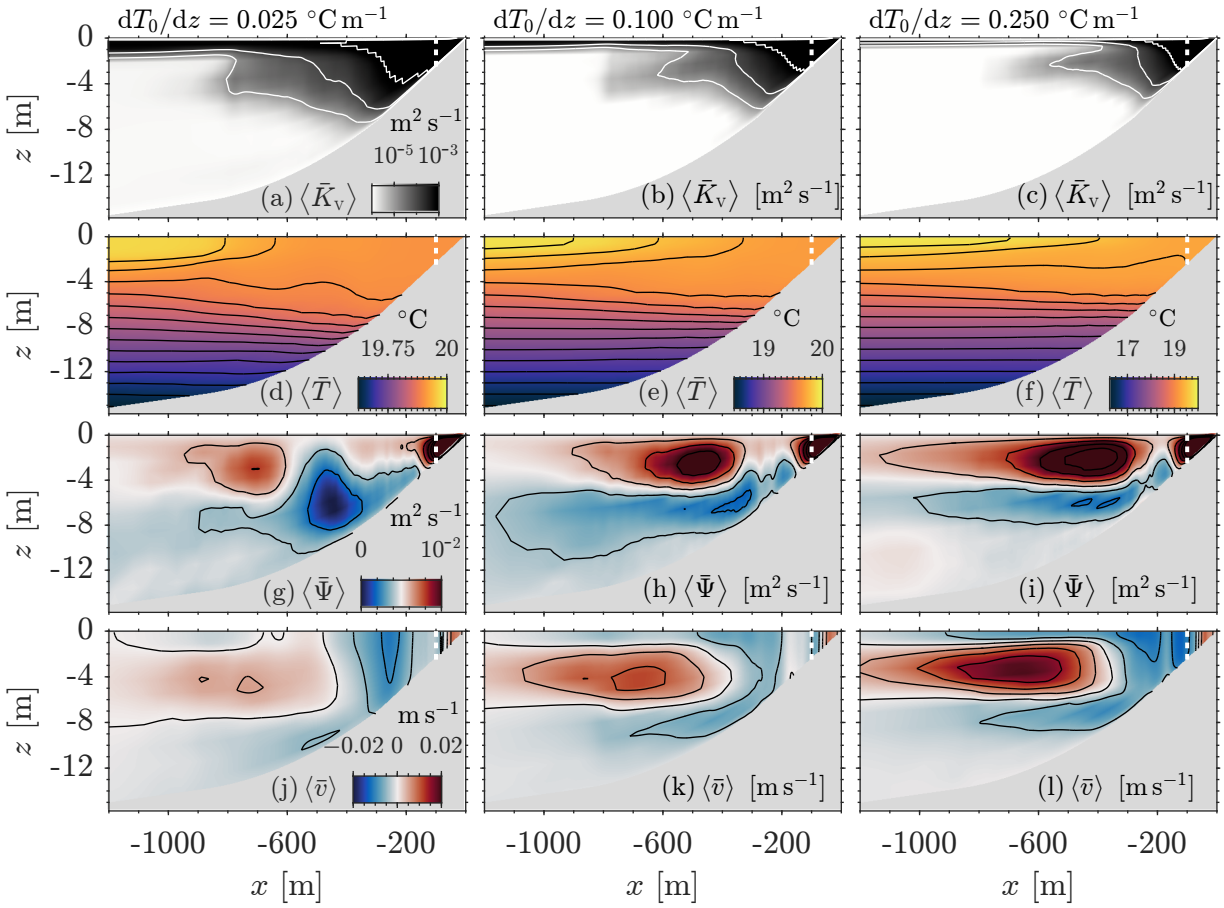

Figure 3.3: Mean (x,z)-sections of (a)-(c) vertical eddy diffusivity $\langle \bar{K}_v \rangle$ with white contours at $\{10^{-5}, 10^{-4}, 10^{-3}\}$ m^2 s^{-1}, (d)-(f) temperature $\langle \bar{T} \rangle$ with black contour interval $\Delta z(dT_0/dz)$ [°C] with initial Δz=1 m vertical separation, (g)-(i) overturning streamfunction $\langle \bar{\Psi} \rangle$ contoured at 2×10^{-3} m^2 s^{-1}, where red (blue) indicates clockwise (counter-clockwise) circulation, and (j)-(l) alongshore velocity $\langle \bar{v} \rangle$ with contour interval of 5×10^{-3} m s^{-1}. The left, center and right columns represent initial stratifications dT_0/dz=$\{0.025, 0.1, 0.25\}$ °C m^{-1}, respectively. Note, the T color-scale and contour interval vary from (d)-(f). The L_{sz}=100 m wide surf-zone is delimited with a vertical dashed white line.

is consistent with a suppression of vertical mixing by strong stratification (*e.g.,* Burchard and Bolding, 2001; Kumar and Feddersen, 2017b). Reduced TRC region stratification is evidenced by shoreward broadening isotherms and sub-surface wedge of mixed fluid extending offshore and centered on $z \approx -4$ m (*e.g.,* Figure 3.3d). The vertical thickness of this TRC-mixed fluid decreases with increased dT_0/dz (Figure 3.3d-3.3f), due to weaker $\langle \bar{K}_v \rangle$. Consequently, isotherm slopes near the base of the sub-surface wedge decrease by roughly half from 2×10^{-3} with a

factor of 10 increase in $\mathrm{d}T_0/\mathrm{d}z$. Reduced isotherm slopes also cause the cross-shore location where well-mixed fluid intersects the surface and bottom, forming fronts, to move closer to shore with increasing $\mathrm{d}T_0/\mathrm{d}z$ (not shown).

The baroclinic pressure gradient associated with cross-shore sloping $\langle\bar{T}\rangle$ isotherms drives an (x,z)-overturning circulation, described by stream-function $\langle\bar{\Psi}\rangle$, where cross-shore and vertical Lagrangian velocities (Eulerian + Stokes drift) are $(\bar{u}_\mathrm{L},\bar{w}_L) = (-\partial_z,\partial_x)\bar{\Psi}$. The inner-shelf circulation associated with $\langle\bar{\Psi}\rangle$ is clockwise near-surface and counter-clockwise near-bottom (red and blue, respectively; Figure 3.3g-3.3i), leading to sub-surface offshore transport and near-surface and bottom onshore transport for $x < -3L_\mathrm{sz}$. The circulation exchanges well mixed fluid from the TRC region with stratified fluid from offshore that when vertically mixed maintains the cross-shore pressure gradient. Inner-shelf $\langle\bar{\Psi}\rangle$ extrema generally occur over $-5L_\mathrm{sz} \leq x \leq -2L_\mathrm{sz}$, defined here as the near-field. As stratification increases the near-surface clockwise cell moves onshore and intensifies, confining the counter-clockwise cell below mid-depth and slightly weakening.

Offshore of $x = -5L_\mathrm{sz}$, termed the far-field, the cross-shore sloping isotherms are in approximate thermal wind balance with vertically sheared alongshore current $\langle\bar{v}\rangle$ (Kumar and Feddersen, 2017b). Maximum northward (positive) $\langle\bar{v}\rangle$, denoted $\max\{\langle\bar{v}\rangle\}$, occurs roughly at the depth where isotherms switch from being upward to downward sloping toward shore ($z \approx -4$ m in Figure 3.3d-3.3f and Figure 3.3j-3.3l). The $\max\{\langle\bar{v}\rangle\}$ increases from 0.6×10^{-2} m s^{-1} to 1.8×10^{-2} m s^{-1} for increase in $\mathrm{d}T_0/\mathrm{d}z$ from 0.025 °C m^{-1} to 0.25 °C m^{-1} (Figure 3.3j & 3.3l). The maximum $\langle\bar{v}\rangle$ occurs offshore of the inner-shelf $\langle\bar{\Psi}\rangle$ extrema. The offshore extent of the positive alongshore current increases with $\mathrm{d}T_0/\mathrm{d}z$, while the vertical thickness decreases weakly. In the TRC region ($x > -4L_\mathrm{sz}$) and offshore of the surf-zone ($x < -L_\mathrm{sz}$), $\langle\bar{v}\rangle$ is negative with weak vertical structure, and on average varying with $\mathrm{d}T_0/\mathrm{d}z$ as $\leq -0.75\max\{\langle\bar{v}\rangle\}$. In the surf-zone, $\langle\bar{v}\rangle$ is much weaker, positive and depth uniform.

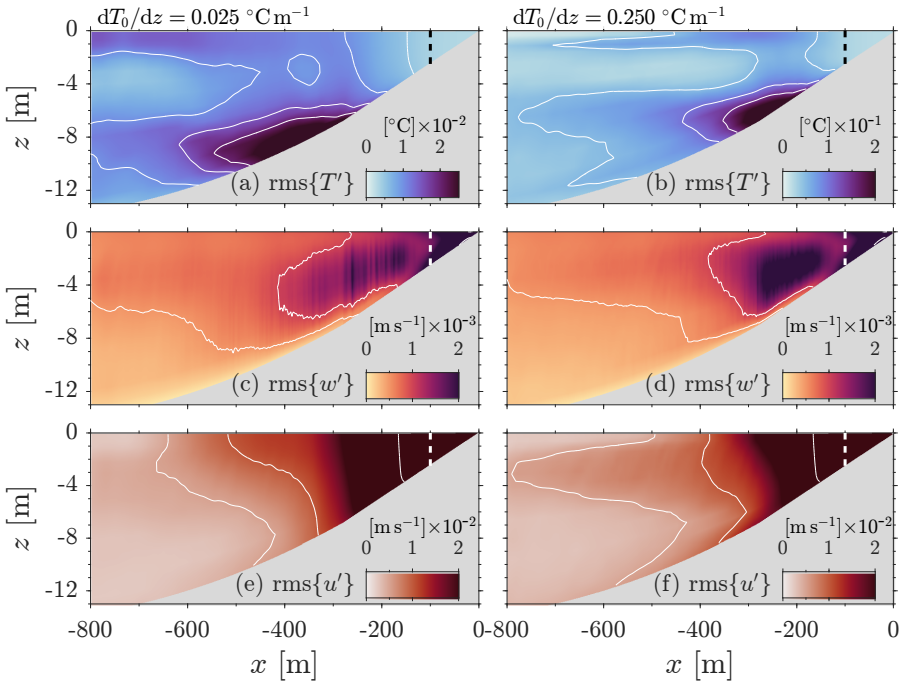

Figure 3.4: Time and alongshore root-mean-square (3.6) (a)-(b) temperature perturbation rms$\{T'\}(x,z)$ with white contour intervals of 0.005 and 0.05 °C in (a) and (b) respectively; (c)-(d) vertical velocity rms$\{w'\}$ with white contours at $\{0.5,1\}\times10^{-3}$ m s^{-1}; and (e)-(f) cross-shore velocity rms$\{u'\}$ with contours at $\{0.5,1,5\}\times10^{-2}$ m s^{-1}. Left panels (a,c,f) have dT_0/dz=0.025 °C m^{-1} and correspond to left panels (a,d,g,j) in Figure 3.3; and right panels (b,d,e) have dT_0/dz=0.25 °C m^{-1}, corresponding to right panels (c,f,i,l) in Figure 3.3. Note the approximate factor of 10 change color scale between (a) and (b). The L_{sz}=100 m wide surf-zone is delimited with a vertical dashed line, and the bottom is gray.

3.3.2 Fluctuating Inner-shelf Response with Varying Stratification

The effects of initial stratification dT_0/dz on eddy variability are introduced using a 24-48 h time and quadratic alongshore average, *e.g.,* for temperature,

$$\text{rms}\{T'\} = \langle\overline{T'^2}\rangle^{\frac{1}{2}}. \tag{3.6}$$

Two levels of stratification, $dT_0/dz = \{0.025, 0.25\}$ °C m^{-1}, are shown in columns of Figure 3.4. For both cases, the largest temperature fluctuations occur at the base of the TRC-mixed fluid ($\approx$ 6-8 m depth, Figure 3.3d-3.3f), where isotherms are vertically compressed $\Delta z \leq 1$ m (Figure 3.3d-3.3f). The maximum is roughly 10$\times$ larger in Figure 3.4b than Figure 3.4a, consistent with 10$\times$

larger N_0^2 and indicating roughly 1 m alongshore rms vertical isotherm displacement. Above the maximum, a vertical band of elevated rms$\{T'\}$ extends to the surface. For $\mathrm{d}T_0/\mathrm{d}z = 0.025\ ^\circ\mathrm{C\,m^{-1}}$ (Figure 3.4a), the band is broader horizontally than for $\mathrm{d}T_0/\mathrm{d}z = 0.25\ ^\circ\mathrm{C\,m^{-1}}$ (Figure 3.4b), spanning roughly $-5L_{sz} < x < -2L_{sz}$ and $-3L_{sz} < x < -2L_{sz}$, respectively. At the surface, there is again increased temperature variability associated with the surface temperature front (*e.g.,* $-4L_{sz} < x < -2L_{sz}$, Figure 3.2b).

Outside the surf-zone, $x < -L_{sz}$, the largest vertical velocity fluctuations rms$\{w'\} \approx 2 \times 10^{-3}\ \mathrm{m\,s^{-1}}$ occur mid-water column and predominately onshore of $x = -4L_{sz}$, consistent with Kumar and Feddersen (2017b). These relatively strong vertical velocities heave isotherms (*e.g.,* Figure 3.2e) driving the band of rms$\{T'\}$, leading to temperature overturns. The magnitude of vertical eddy velocities increases slightly with $\mathrm{d}T_0/\mathrm{d}z$, while the cross-shore extent decreases weakly, consistent with the cross-shore narrowing of rms$\{T'\}$. The weak enhancement of rms$\{w'\}$ near $x = -2L_{sz}$ with $\mathrm{d}T_0/\mathrm{d}z$ is potentially related to stratification enhancing the growth of 3D instabilities. In contrast to temperature fluctuations, the vertical velocity fluctuations have similar structure and magnitude despite the order of magnitude change in $\mathrm{d}T_0/\mathrm{d}z$, suggesting TRC induced vertical velocity fluctuations are weakly affected by stratification.

The cross-shore directed eddy velocity peak rms$\{u'\} \approx 0.22\ \mathrm{m\,s^{-1}}$ occurs within the surf-zone, $x > -L_{sz}$, and decreases to $< 5 \times 10^{-2}\ \mathrm{m\,s^{-1}}$ by $x = -2L_{sz}$ (Figure 3.4e). For $x > -2L_{sz}$, rms$\{u'\}$ vertical structure is weak and largely independent of $\mathrm{d}T_0/\mathrm{d}z$. Vertical structure increases over $-3L_{sz} < x < -2L_{sz}$, particularly for cases with higher stratification (*e.g.,* Figure 3.4f). Offshore of $-4L_{sz}$, rms$\{u'\}$ continues to decrease and tends toward sub-surface maximum roughly following $\langle\bar{\Psi}\rangle$ streamlines, suggesting offshore advection of the residual eddy velocities. The weak variation in eddy velocity statistics with $\mathrm{d}T_0/\mathrm{d}z$ combined with temperature fluctuations increasing in proportion to $\mathrm{d}T_0/\mathrm{d}z$, suggests TRC induced over-turns may have larger associated diapycnal mixing.

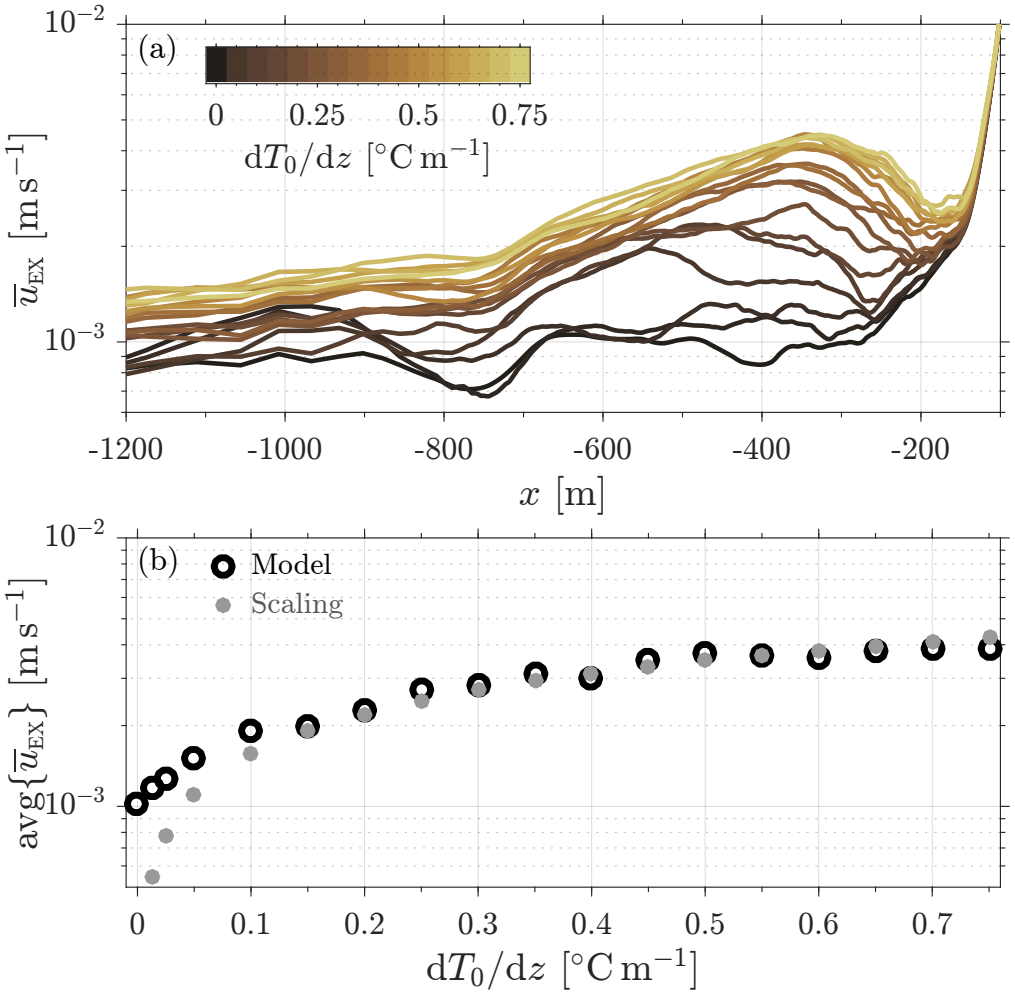

Figure 3.5: (a) Inner-shelf cross-shore exchange velocity $\overline{u}_{\rm EX}$ (3.7) versus cross-shore coordinate x and initial stratification dT_0/dz (colors). (b) Cross-shore ($-5L_{\rm sz} \le x \le -2L_{\rm sz}$) averaged $\overline{u}_{\rm EX}$ (3.8) versus dT_0/dz (black circles) with the near-field exchange scaling (3.9) in gray. The surf-zone width is $L_{\rm sz} = 100$ m, and in (a) only $x < -L_{\rm sz}$ is shown.

3.3.3 Near-Field Baroclinic Cross-shore Exchange

Variation in the strength of baroclinic circulation $\langle\bar{\Psi}\rangle$ with initial stratification is evaluated using a cross-shore exchange velocity based on the alongshore averaged (3.4) Lagrangian (Eulerian + Stokes) cross-shore velocity $\overline{u}_{\rm L}$ (*e.g.,* Grimes et al., 2020c),

$$\overline{u}_{\rm EX}(x) \;=\; \langle \frac{-2}{h+\bar{\eta}} \int_{-h}^{\bar{\eta}} \overline{u}_{\rm L}(x,z,t)\, dz \rangle, \tag{3.7}$$

where the vertical integral is restricted to offshore directed flow indicated with superscript $\overline{u}_{\mathrm{L}}^{-}$. As a bulk measure of cross-shore exchange flow strength (*e.g.,* Lerczak et al., 2006; MacCready, 2011), $\overline{u}_{\mathrm{EX}}$ is a useful metric to evaluate the effects of stratification on TRC-induced inner-shelf (x,z)-circulation and cross-shore exchange potential (Suanda and Feddersen, 2015; Kumar and Feddersen, 2017a,b). For $x < -1.5L_{\mathrm{sz}}$, roughly the division between surf-zone and inner-shelf circulation cells (Figure 3.3g-i), $\overline{u}_{\mathrm{EX}}$ is $O(10^{-3}\ \mathrm{m\,s^{-1}})$ and generally increases with increasing $\mathrm{d}T_0/\mathrm{d}z$ (Figure 3.5a). For $\mathrm{d}T_0/\mathrm{d}z \gtrapprox 0.1\ ^{\circ}\mathrm{C\,m^{-1}}$, $\overline{u}_{\mathrm{EX}}(x)$ has a near-field $(-5L_{\mathrm{sz}} \le x \le -2L_{\mathrm{sz}})$ inner-shelf maximum (Figure 3.5a), roughly where well-mixed fluid intersects the surface and bottom (Figure 3.3d-f) and between inner-shelf $\langle\bar{\Psi}\rangle$ extrema (Figure 3.3h-3.3i). The maximum $\overline{u}_{\mathrm{EX}}$ also tends to move slightly onshore with increasing stratification, consistent with the onshore movement of the upper $\langle\bar{\Psi}\rangle$ cell.

The initial stratification dependence of baroclinic exchange is explored using the near-field $(-5L_{\mathrm{sz}} \le x \le -2L_{\mathrm{sz}})$ averaged $\overline{u}_{\mathrm{EX}}$ spanning the inner-shelf maximum, defined as,

$$\mathrm{avg}\{\overline{u}_{\mathrm{EX}}\} = (3L_{\mathrm{sz}})^{-1} \int_{-5L_{\mathrm{sz}}}^{-2L_{\mathrm{sz}}} \overline{u}_{\mathrm{EX}}(x)\,\mathrm{d}x. \tag{3.8}$$

Consistent with Figure 3.5a, $\mathrm{avg}\{\overline{u}_{\mathrm{EX}}\}$ increases with $\mathrm{d}T_0/\mathrm{d}z$ (black circles, Figure 3.5b), although the rate of change decreases with increasing $\mathrm{d}T_0/\mathrm{d}z$. The near-field $\overline{u}_{\mathrm{EX}}$ maximum occurs near the transition from depth uniform weak stratification $(x > -3L_{\mathrm{sz}})$ to a weakly stratified far-field wedge bound by stratified fluid below and above ($x < -5L_{\mathrm{sz}}$, Figure 3.3d-3.3f), consistent with gravity current intrusion into stratified ambient (*e.g.,* Bolster et al., 2008). Near-field exchange is related to $\mathrm{d}T_0/\mathrm{d}z$ using baroclinic velocity scaling $U = (\mathrm{C}_0 N_0 \tilde{h})$, with near-field average water depth $\tilde{h} \approx 8.25$ m, and Froude number C_0. Assuming the offshore directed sub-surface transport occurs over height $\mathrm{C}_1\tilde{h}$, the average near-field exchange velocity is scaled as,

$$\mathrm{avg}\{\overline{u}_{\mathrm{EX}}\} \approx (\mathrm{C}_1\tilde{h})\,U/\tilde{h} = (\mathrm{C}_0\mathrm{C}_1)N_0\tilde{h}, \tag{3.9}$$

Scaling (3.9) with constant $(C_0C_1) = 1.4 \times 10^{-2}$ (gray, Figure 3.5b) generally reproduces the observed behavior of avg$\{\overline{u}_{EX}\}$ for $dT_0/dz \geq 0.05$ °C m^{-1} with $r^2 = 0.99$ and skill-score $(1 - \text{mse}/\text{var})^{1/2} = 0.98$ (mse is mean square error and var the model variance). The result is not sensitive to the cross-shore bounds chosen in (3.8), provided it spans the $\overline{u}_{EX}$ maximum. Consistency of scaling (3.9) over large range in stratification suggests the baroclinic exchange flow is self-similar. Fixing the vertical scale to $C_1\tilde{h} = \tilde{h}/3$, roughly the vertical separation between $\langle\bar{\Psi}\rangle$ extrema (Figure 3.3g-i), suggests small Froude number $C_0 \approx 0.04$ compared to lock-release gravity currents where $C_0 \sim 1/4$ (Bolster et al., 2008). Weak baroclinic momentum advection suggests additional dynamics in the cross-shore momentum balance, potentially related to either near-field TRC effects or transition to far-field geostrophy (*e.g.,* Kumar and Feddersen, 2017a,b) discussed next.

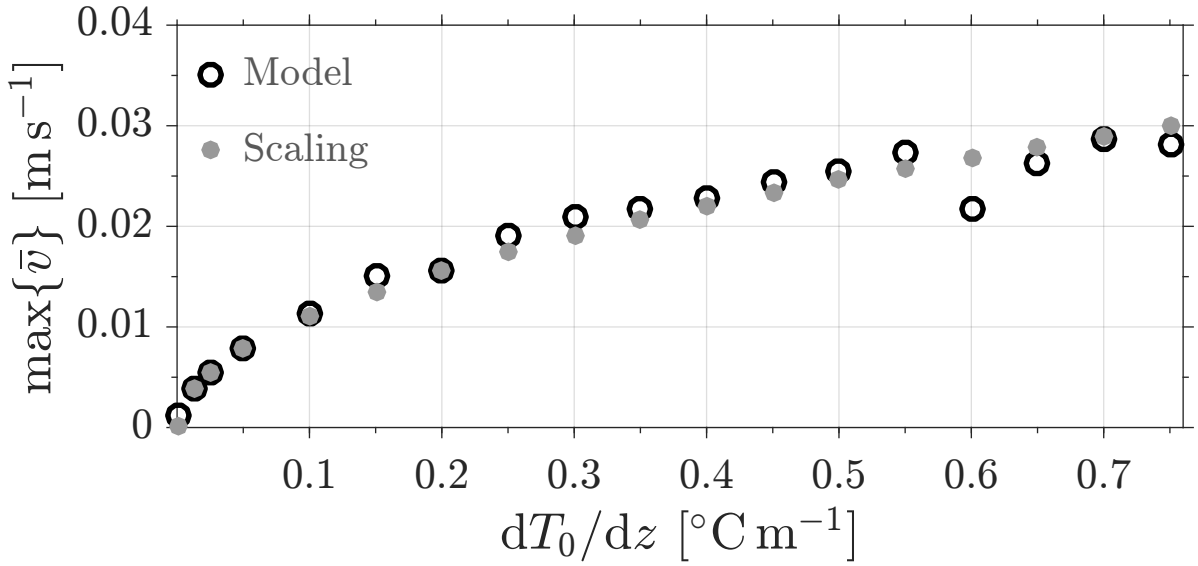

Figure 3.6: Mean alongshore velocity maximum max$\{\langle\bar{v}\rangle\}$ versus dT_0/dz (black circles), with the scaling (3.12) for maximum geostrophic velocity max$\{\bar{v}_g\}$ in gray.

3.3.4 Far-Field Alongshore Thermal Wind

The strength of alongshore current $\langle\bar{v}\rangle$ also increases with dT_0/dz (Figure 3.3d-3.3f), forming a far-field ($x < -5L_{sz}$) positive alongshore current roughly centered between the broadening

$\langle \bar{T} \rangle$ isotherms (Figure 3.3d-3.3f). The strength of far-field $\langle \bar{v} \rangle$ is quantified using the maximum alongshore velocity $\max\{\langle \bar{v} \rangle\}$ (black, Figure 3.6). The $\max\{\langle \bar{v} \rangle\}$ increases with $\mathrm{d}T_0/\mathrm{d}z$ (black, Figure 3.6), consistent with Figure 3.3j-3.3l. However, the rate of change in $\max\{\langle \bar{v} \rangle\}$ decreases with increasing stratification, similar to $\mathrm{avg}\{\overline{u}_{\mathrm{EX}}\}$ (Figure 3.5).

Kumar and Feddersen (2017b) found that offshore of $4.5L_{\mathrm{sz}}$ alongshore flow was in approximate thermal wind balance,

$$\frac{\partial \bar{v}_{\mathrm{g}}}{\partial z} = \frac{g\alpha}{f}\frac{\partial \bar{T}}{\partial x}, \tag{3.10}$$

where v_g is the geostrophic component of alongshore velocity. Thermal wind relation (3.10) also implies that $\bar{v}_g$ will have a sub-surface maximum at the depth were isotherm slopes change sign, consistent with Figure 3.3d-f and Figure 3.3j-l. A scaling for $\max\{\langle \bar{v} \rangle\}$ based on thermal wind relation (3.10) is formed by relating far-field TRC-mixed wedge isotherm slope to initial stratification through the baroclinic Rossby length $L_{\mathrm{R}} = (N_0 H/f)$ (*e.g.,* Pedlosky, 1978), with far-field depth scale H, such that,

$$\begin{aligned} \frac{\partial \bar{T}}{\partial x} &\approx \frac{H}{L_{\mathrm{R}}}\frac{\mathrm{d}T_0}{\mathrm{d}z} \\ &= \frac{f}{N_0}\frac{\mathrm{d}T_0}{\mathrm{d}z}. \end{aligned} \tag{3.11}$$

The magnitude of L_{R} increases with $\mathrm{d}T_0/\mathrm{d}z$, ranging from ≈ 475 m at $\mathrm{d}T_0/\mathrm{d}z = 0.0125\ ^{\circ}\mathrm{C\,m^{-1}}$ to ≈ 1800 m at $\mathrm{d}T_0/\mathrm{d}z = 0.75\ ^{\circ}\mathrm{C\,m^{-1}}$ with $H = 4$ m. Substituting (3.11) in (3.10) implies the maximum geostrophic velocity scales as,

$$\max\{\bar{v}_{\mathrm{g}}\} \approx \mathrm{C}_2 H N_0, \tag{3.12}$$

where $\mathrm{C}_2 H$ represents the vertical scale over which $\langle \bar{v} \rangle$ increases to $\max\{\langle \bar{v} \rangle\}$. The scaling (3.12) with constant $\mathrm{C}_2 H = 0.8$ m (gray Figure 3.6) reproduces the $\mathrm{d}T_0/\mathrm{d}z$ dependence of $\max\{\langle \bar{v} \rangle\}$, with $r^2 = 0.98$, indicating the maximum alongshore thermal wind is also self-similar. Setting

$H = h(x{=}{-}6L_{sz}) = 12$ m gives $C_2 \approx 0.07$ m, implying vertically thin positive alongshore flow, qualitatively consistent with structure of $\langle \bar{v} \rangle$ (Figure 3.3j-3.3l).

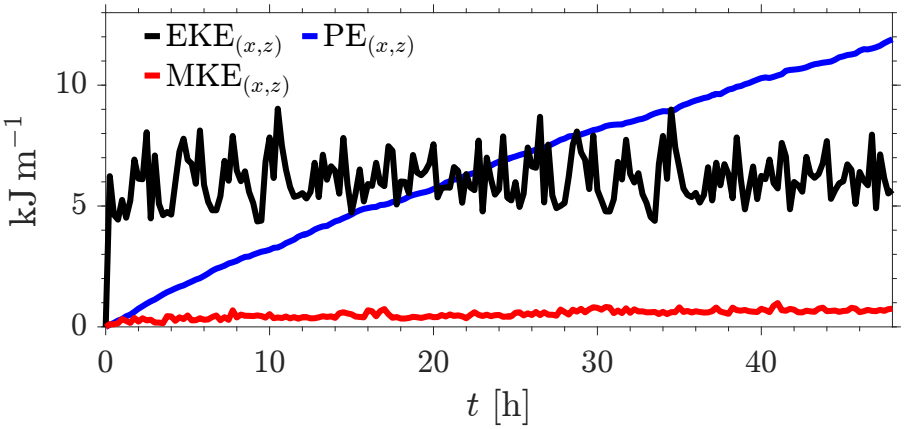

Figure 3.7: Time evolution of dT_0/dz=0.25 °C m^{-1} domain integrated eddy kinetic energy EKE$_{(x,z)}$ (3.14) in black, mean kinetic energy MKE$_{(x,z)}$ (red), and potential energy PE$_{(x,z)}$ (blue).

3.4 Results: Effect of Stratification, Waves, & TRCs on Energetics

Here, we examine aspects of the energy exchange between the forced surf-zone and the adjoining inner-shelf for varying initial stratification. First, the domain integrated kinetic and potential energy evolution are presented for $dT_0/dz = 0.25$ °C m^{-1}, followed by analysis of spatial structure and temporal evolution with varying stratification. The kinetic energy is decomposed using (3.3) into contributions from specific eddy kinetic energy,

$$\text{eke}(x,z,t) = \frac{\rho}{2}\overline{(u'^2 + v'^2)}, \tag{3.13}$$

and specific y-mean kinetic energy mke defined similar to (3.13) using $(\bar{u}_L, \bar{v})$. As surf-zone breaking wave rotational forcing is the only external driver of eddy variability (*e.g.,* Grimes et al., 2020c), eke quantifies energy in the TRC-induced eddy field. The domain (x,z)-area A integrated

eke is,

$$\mathrm{EKE}_{(x,z)}(t) = \int_A \mathrm{eke}\ \mathrm{d}A, \tag{3.14}$$

where subscripts indicate the integrated dimensions. The domain integrated mean kinetic energy $\mathrm{MKE}_{(x,z)}(t)$ is defined similar to $\mathrm{EKE}_{(x,z)}$ (3.14) by substituting mke for eke. For stratified conditions, irreversible vertical mixing induces changes in alongshore mean specific potential energy relative to the initial condition ρ_0 (3.2), defined as (*e.g.,* Kumar and Feddersen, 2017b),

$$\Delta\mathrm{pe}(x,z,t) = gz\left[\overline{\rho}(x,z,t) - \rho_0(z)\right]. \tag{3.15}$$

For a closed domain, vertical mixing increases the domain area integrated potential energy, denoted $\mathrm{PE}_{(x,z)}(t)$.

For $\mathrm{d}T_0/\mathrm{d}z = 0.25\ ^\circ\mathrm{C\,m^{-1}}$, the TRC-induced eddy field reaches 85% of the 24-48 h time average $\langle \mathrm{EKE}_{(x,z)} \rangle = 6.24\ \mathrm{kJ\,m^{-1}}$ in roughly 1 h (black, Figure 3.7). Subsequently, $\mathrm{EKE}_{(x,z)}$ varies $\pm 15\%$ of $\langle \mathrm{EKE}_{(x,z)} \rangle$ over time-scales of $\lessapprox 3$ h with no discernible linear trend for $t > 1$ h, indicating the eddy field has equilibrated. The domain integrated mean kinetic energy, $\mathrm{MKE}_{(x,z)}(t)$ increases continuously throughout the 48 h simulation, but is much weaker than $\mathrm{EKE}_{(x,z)}$, only reaching $\approx 0.75\ \mathrm{kJ\,m^{-1}}$ in 48 h (red, Figure 3.7). Alongshore flow $\bar{v}$ dominates $\mathrm{MKE}_{(x,z)}$, with minor contributions from $\bar{u}_\mathrm{L}$, and $\mathrm{MKE}_{(x,z)}$ temporal variability is also relatively large, $\approx 25\,\%$ of the 24-48 h mean (not shown). The domain integrated potential energy change $\mathrm{PE}_{(x,z)}(t)$ also increases continuously, becoming larger than $\mathrm{MKE}_{(x,z)}$ after ≈ 30 min and larger than $\langle \mathrm{EKE}_{(x,z)} \rangle$ after 22 h (blue, Figure 3.7). The $\mathrm{PE}_{(x,z)}$ slope decreases slowly between $0 < t \leq 12$ h, becoming approximately constant after 24 h. Continuous $\mathrm{PE}_{(x,z)}$ growth suggests continuous water-mass transformation.

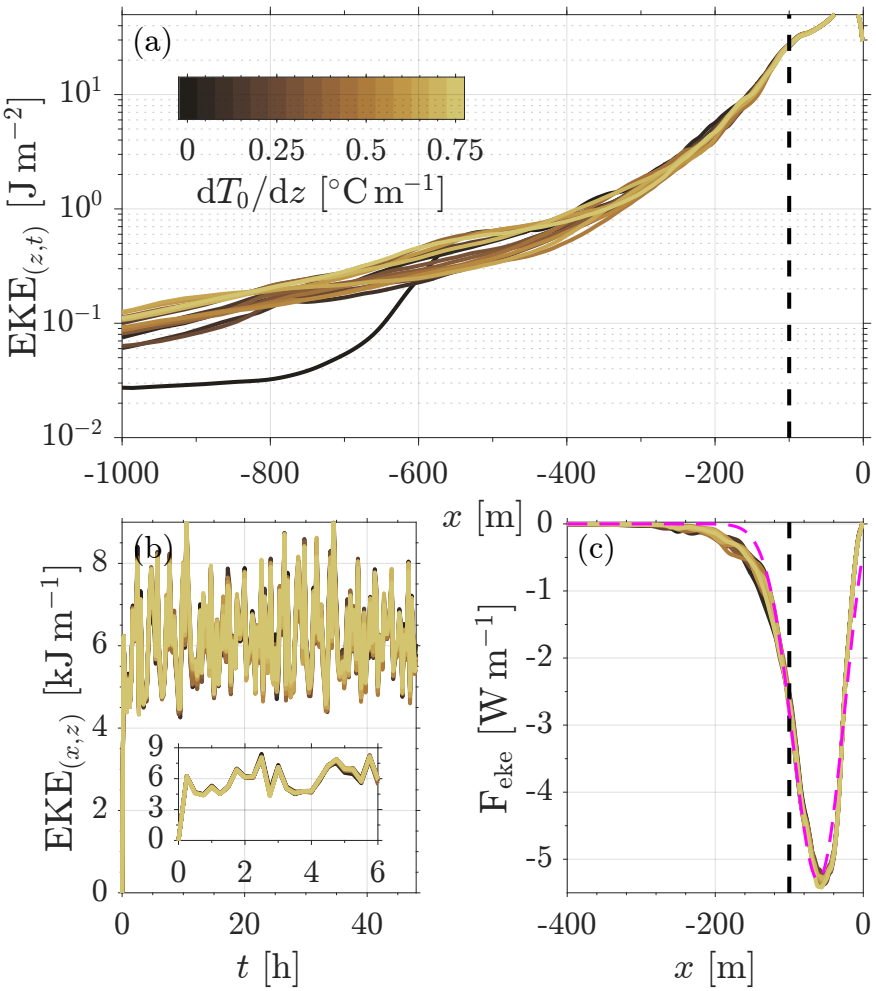

Figure 3.8: (a) Cross-shore distribution of depth integrated mean eddy kinetic energy $\mathrm{EKE}_{(z,t)}$ at varying $\mathrm{d}T_0/\mathrm{d}z$ (colors). (b) 48 h time evolution of alongshore averaged depth and cross-shore integrated eddy kinetic energy $\mathrm{EKE}_{(x,z)}$, with inset showing 6 h spin-up period. (c) Distribution of cross-shore directed kinetic energy flux $\mathrm{F}_{\mathrm{eke}}$ (3.17), with Gaussian barotropic rotational velocity scaling (3.32)-(3.36) in magenta. In (a,c), the vertical dashed line indicates $x = -L_{\mathrm{sz}}$.

3.4.1 Eddy Kinetic Energy

The effect of stratification on the cross-shore distribution of TRC-induced velocity fluctuations (u', v') is evaluated by depth integrating the time-averaged specific eddy kinetic energy (3.13),

$$\mathrm{EKE}_{(z,t)}(x) = \int_{-h}^{\langle\bar{\eta}\rangle} \langle \mathrm{eke} \rangle \, \mathrm{d}z, \tag{3.16}$$

where the subscripted t indicates time averaged integrand. The cross-shore varying $\mathrm{EKE}_{(z,t)}$ is maximum in the surf-zone and decreases rapidly offshore (Figure 3.8a). At $x = -L_{\mathrm{sz}}$, $\mathrm{EKE}_{(z,t)} \approx 25\ \mathrm{J\,m^{-2}}$ implies a depth average velocity magnitude of $0.14\ \mathrm{m\,s^{-1}}$, consistent with the $\mathrm{rms}\{u'\}$ magnitude (Figure 3.4c). For all simulations, $\mathrm{EKE}_{(z,t)}$ consistently decreases offshore with no obvious $\mathrm{d}T_0/\mathrm{d}z$ dependence out to $x = -6L_{\mathrm{sz}}$ (colored lines, Figure 3.8a). The $\mathrm{d}T_0/\mathrm{d}z = 0$ case (black) differs for $x < -6L_{\mathrm{sz}}$ due to offshore advection of baroclinic eddy potential vorticity along $\langle\bar{\Psi}\rangle$ streamlines for $x \lessapprox -400$ m in stratified simulations (as suggested by $\mathrm{rms}\{u'\}$, Figure 3.4c). The cross-shore $\mathrm{EKE}_{(z,t)}$ structure suggests that the energetic TRC-induced eddies are confined within a few surf-zone widths from shore, and this distribution is weakly affected by stratification.

The time dependent $\mathrm{EKE}_{(x,z)}$ (3.14) is similar for all $\mathrm{d}T_0/\mathrm{d}z$ simulations (Figure 3.8b), suggesting that TRC-induced eddy kinetic energy is slaved to the stochastic surf-zone rotational forcing, which is the same for all simulations. The absence of $\mathrm{EKE}_{(x,z)}$ secular growth indicates that surf-zone eddy kinetic energy generation is in equilibrium with its domain integrated destruction through conversion (to potential and alongshore mean kinetic energy) and viscous dissipation (internal energy, not considered here).

The flux of eke to the inner-shelf is quantified using the mean cross-shore kinetic energy flux,

$$\mathrm{F_{eke}} = \int_{-h}^{\langle\bar{\eta}\rangle} \langle\overline{u_{\mathrm{L}}\,(\mathrm{eke})}\rangle\,\mathrm{d}z. \tag{3.17}$$

Eddy transport dominates $\mathrm{F_{eke}}$, *i.e.,* from $u'(u'^2 + v'^2)$, and negative $\mathrm{F_{eke}}$ indicates a surf-zone to inner-shelf flux (Figure 3.8c). The $\mathrm{F_{eke}}$ is similar for all $\mathrm{d}T_0/\mathrm{d}z$, indicating that TRCs are largely unaffected by initial stratification, consistent with $\mathrm{rms}\{u'\}$ and $\mathrm{rms}\{w'\}$ (Figure 3.4b-c). As eddy kinetic energy statistics are approximately stationary for $t > 1$ h, the $x < -L_{\mathrm{sz}}$ slope of $\mathrm{F_{eke}}$ indicates either frictional damping of $\mathrm{EKE}_{(z,t)}$ or conversion to potential energy. Rapid $\mathrm{F_{eke}}$ divergence over $-4L_{\mathrm{sz}} \le x \le -1L_{\mathrm{sz}}$ for all $\mathrm{d}T_0/\mathrm{d}z$, indicates the TRC-induced eke is dissipated/converted over similar cross-shore region independent of stratification. The magnitude and cross-shore $\mathrm{F_{eke}}$ distribution is consistent with previously derived TRC velocity scaling by

Suanda and Feddersen (2015) (magenta, Figure 3.8c; discussed in more detail in Section 3.5.4).

3.4.2 Potential Energy

Mixing raises $\mathrm{PE}_{(x,z)}$ (*e.g.,* Figure 3.7) and enhanced mixing in the TRC region ($x > -400$ m) generates inner-shelf Δpe anomalies, indicated by sloping isotherms (Figure 3.3d-f), which drive inner-shelf circulation (*e.g.,* Kumar and Feddersen, 2017b). The effect of varying initial stratification $\mathrm{d}T_0/\mathrm{d}z$ on TRC-induced eddy driven mixing and the resulting potential energy structure and evolution are evaluated by decomposing the change in alongshore averaged specific potential energy (3.15) into changes in background (Δbpe) and available (ape) potential energies (*e.g.,* Winters et al., 1995; MacCready and Giddings, 2016),

$$\Delta\mathrm{pe}(x,z,t) \equiv \Delta\mathrm{bpe}(z,t) + \mathrm{ape}(x,z,t). \tag{3.18}$$

The change in background potential energy is defined as,

$$\Delta\mathrm{bpe}(z,t) = g\,z\,[\rho_\mathrm{s}(z,t) - \rho_0(z)]\,, \tag{3.19}$$

in terms of the sorted density profile $\rho_s(z,t)$, derived from $\overline{\rho}(x,z,t)$ by adiabatically redistributing water parcels such that the sorted isopycnals are horizontal, thus giving the minimum potential energy state of the system (Winters et al., 1995). Irreversible mixing modifies ρ_s and increases the background potential energy. TRC region ($x > -4L_\mathrm{sz}$) mixing also modifies the local specific potential energy, manifested as sloped $\langle\bar{T}\rangle$ isotherms (*e.g.,* Figure 3.3d-f). The ape is commonly defined as the work required to vertically displace parcels through the sorted density field, as determined by ρ_s (*e.g.,* Winters and Barkan, 2013; MacCready and Giddings, 2016),

$$\mathrm{ape}(x,z,t) = \int_{\bar{z}_\mathrm{s}}^{z} g\,\left[\bar{\rho}(x,z,t) - \rho_\mathrm{s}(z',t)\right]\,\mathrm{d}z', \tag{3.20}$$

where $\bar{z}_s$ is the z-level corresponding to $\rho_s(\bar{z}_s) = \bar{\rho}(x,z,t)$. Thus, ape (3.20) is a measure of available potential energy due to cross-shore sloping alongshore averaged isopycnals. As the ape is the available component of the alongshore averaged density field, it does not include contributions from alongshore varying TRC induced eddies whose statistics are largely stationary (cf. Section 3.4.1).

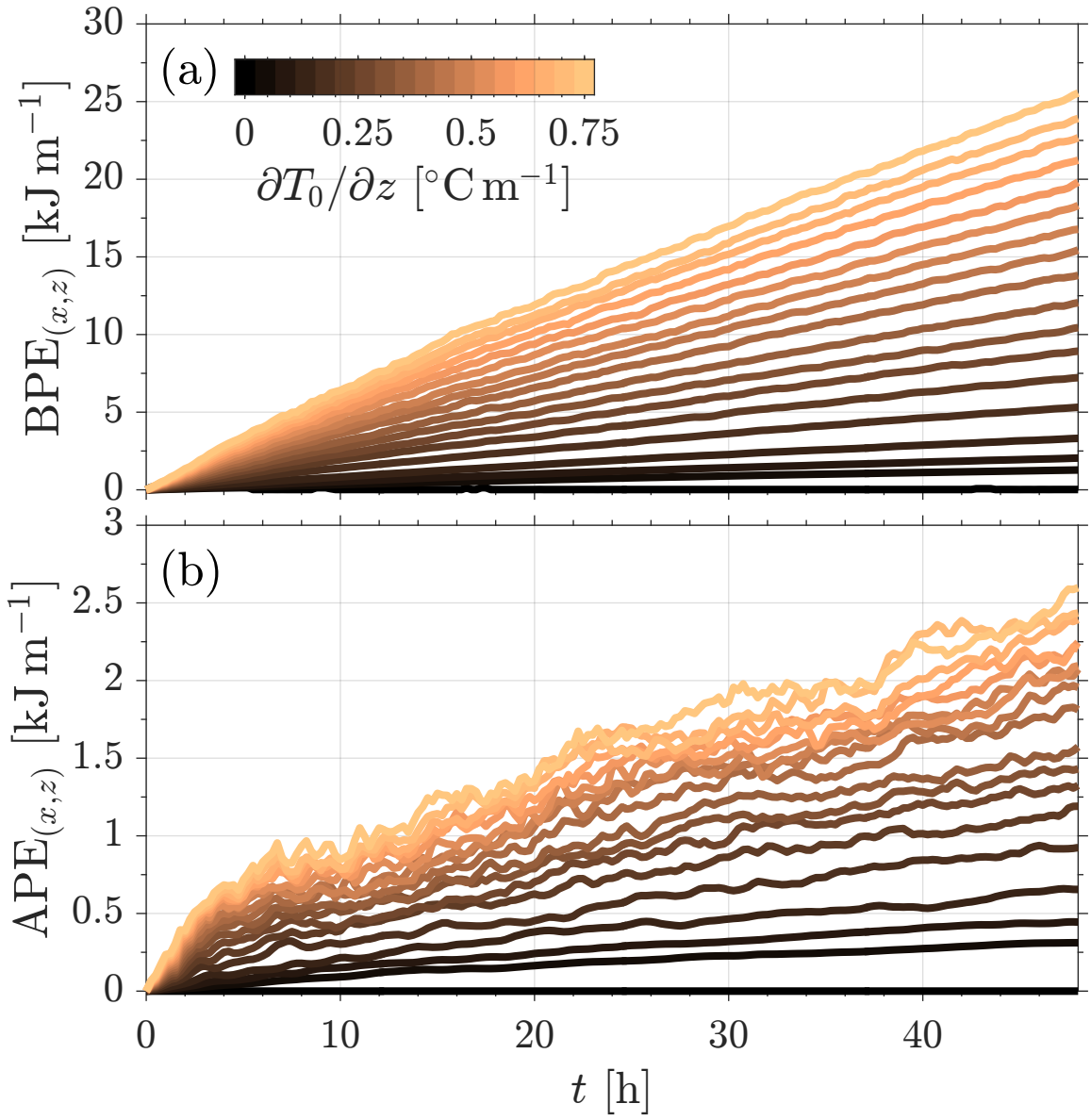

Figure 3.9: Time evolution of domain integrated (a) background potential energy $\text{BPE}_{(x,z)}$ (3.21) and (b) available potential energy $\text{APE}_{(x,z)}$ (3.22) at varying levels of initial stratification $\text{d}T_0/\text{d}z$ (colors).

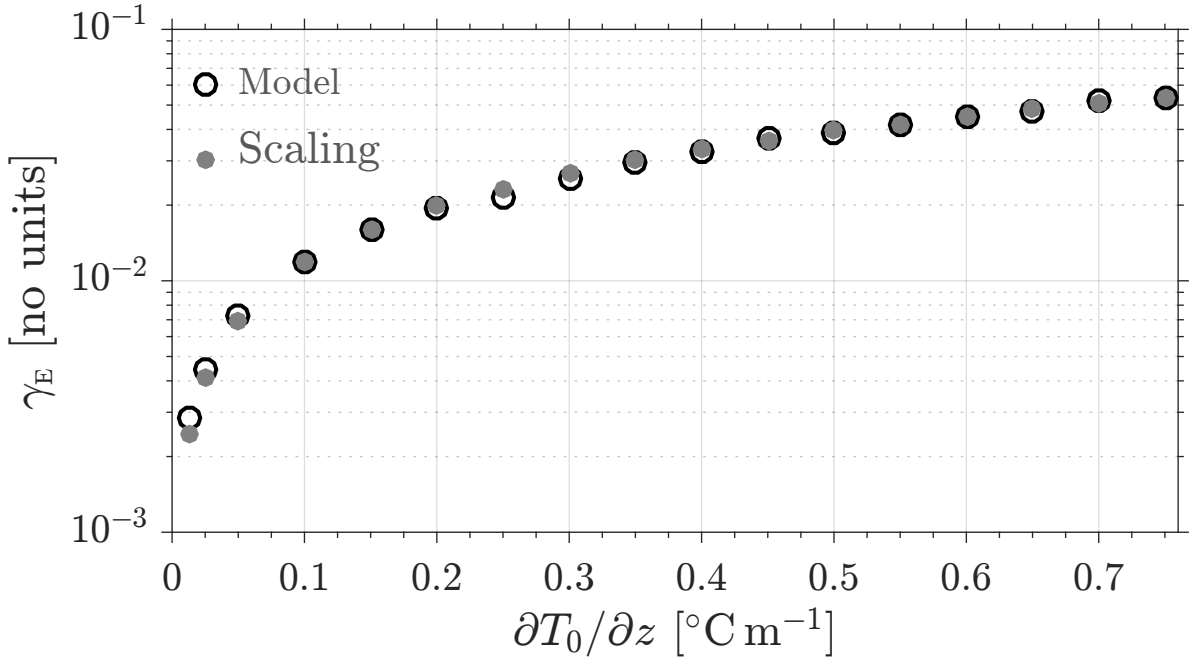

Figure 3.10: Domain integrated and 24-48 h averaged $\mathrm{EKE}_{(x,z)}$ to $\mathrm{PE}_{(x,z)}$ bulk conversion efficiency γ_{E} (3.23) versus $\mathrm{d}T_0/\mathrm{d}z$ (black circles) and $(\mathrm{d}T_0/\mathrm{d}z)^{3/4}$ scaling (gray dots).

Domain Integrated Potential Energy Evolution with Varying Stratification

The temporal evolution of potential energy is analyzed using the domain integrated background potential energy change,

$$\mathrm{BPE}_{(x,z)}(t) \quad = \quad \int_{-\max\{h\}}^{0} \Delta\mathrm{bpe}(z,t)\,\mathcal{L}_x(z)\,\mathrm{d}z, \tag{3.21}$$

where the area increment $(\mathcal{L}_x(z)\,\mathrm{d}z)$ accounts for the sloping bottom, such that vertically integrating $(\mathcal{L}_x(z)\,\mathrm{d}z)$ gives the domain (x,z)-area A. The (x,z)-area integrated available potential energy is given by the residual,

$$\mathrm{APE}_{(x,z)}(t) \quad \equiv \quad \mathrm{PE}_{(x,z)} - \mathrm{BPE}_{(x,z)}. \tag{3.22}$$

Initially, at $t = 0$, $\mathrm{BPE}_{(x,z)}$ and $\mathrm{APE}_{(x,z)}$ are both zero (Figure 3.9). For stratified cases, both quantities subsequently increase as irreversible mixing and reversible buoyancy fluxes modify the density field. The $\mathrm{BPE}_{(x,z)}$ growth rate is roughly constant for $t > 24$ h with slope increasing with increasing $\mathrm{d}T_0/\mathrm{d}z$ (Figure 3.9a). For $\mathrm{d}T_0/\mathrm{d}z = 0.0125\ ^\circ\mathrm{C\,m^{-1}}$, the 24-48 h averaged growth rate is 0.006 $\mathrm{W\,m^{-1}}$, whereas for $\mathrm{d}T_0/\mathrm{d}z = 0.75\ ^\circ\mathrm{C\,m^{-1}}$ the growth rate is 0.13 $\mathrm{W\,m^{-1}}$. Similarly, $\mathrm{APE}_{(x,z)}$ increases with $\mathrm{d}T_0/\mathrm{d}z$, but is smaller than $\mathrm{BPE}_{(x,z)}$ by roughly an order of magnitude (Figure 3.9b). Thus, only a small fraction, $O(10\%)$, of the potential energy changes are available for driving inner-shelf circulation. The $\mathrm{APE}_{(x,z)}$ temporal variability increases for strong stratification. For vertical mixing localized to $-4L_{\mathrm{sz}} < x < -L_{\mathrm{sz}}$, modeled $\mathrm{PE}_{(x,z)}$ growth rates imply a mean vertical buoyancy flux varying between 0.3×10^{-4} $\mathrm{W\,m^{-2}}$ and 5×10^{-4} $\mathrm{W\,m^{-2}}$, similar to inner-shelf observations of individual internal bore mixing events (Sinnett et al., 2018).

The increasing 24-48 h growth rate of $\mathrm{PE}_{(x,z)} = \mathrm{BPE}_{(x,z)} + \mathrm{APE}_{(x,z)}$ with initial stratification suggests the fraction of surf-zone generated eddy kinetic energy converted into $\mathrm{PE}_{(x,z)}$ increases with $\mathrm{d}T_0/\mathrm{d}z$. This implies the domain integrated frictional dissipation rate is reduced with $\mathrm{d}T_0/\mathrm{d}z$ for energy conservation (not shown). The conversion rate is estimated using the 24-48 h time averaged $\mathrm{PE}_{(x,z)}$ growth rate, $\langle \partial_t \mathrm{PE}_{(x,z)} \rangle$. As the cross-shore kinetic energy flux $\mathrm{F_{eke}}$ is not affected by initial stratification, a bulk conversion efficiency γ_{E} from eddy kinetic to potential energy is estimated as,

$$\gamma_{\mathrm{E}} = \frac{\langle \partial_t \mathrm{PE}_{(x,z)} \rangle}{\mathrm{F}_{\mathrm{eke}}^{(\mathrm{sz})}}, \tag{3.23}$$

where $\mathrm{F}_{\mathrm{eke}}^{(\mathrm{sz})} = \mathrm{F_{eke}}(x = -L_{\mathrm{sz}})$, the eddy kinetic energy flux at $x = -L_{\mathrm{sz}}$, is used to quantify the source rate. As initial stratification increases, γ_{E} increases from ≈ 0.003 to 0.05 (black circles, Figure 3.10), suggesting only a small fraction of $\mathrm{F}_{\mathrm{eke}}^{(\mathrm{sz})}$ goes to increasing $\mathrm{PE}_{(x,z)}$. The increase in γ_{E} with $\mathrm{d}T_0/\mathrm{d}z$ indicates the surf-zone generates more than sufficient energy to mix the stratified inner-shelf. The growth of γ_{E} decreases with increasing stratification, roughly following $\mathrm{C_E}\,(\mathrm{d}T_0/\mathrm{d}z)^{3/4}$ with dimensional constant $\mathrm{C_E} = 0.066\ (^\circ\mathrm{C\,m^{-1}})^{-3/4}$ (gray, Figure 3.10).

Specific Background Potential Energy

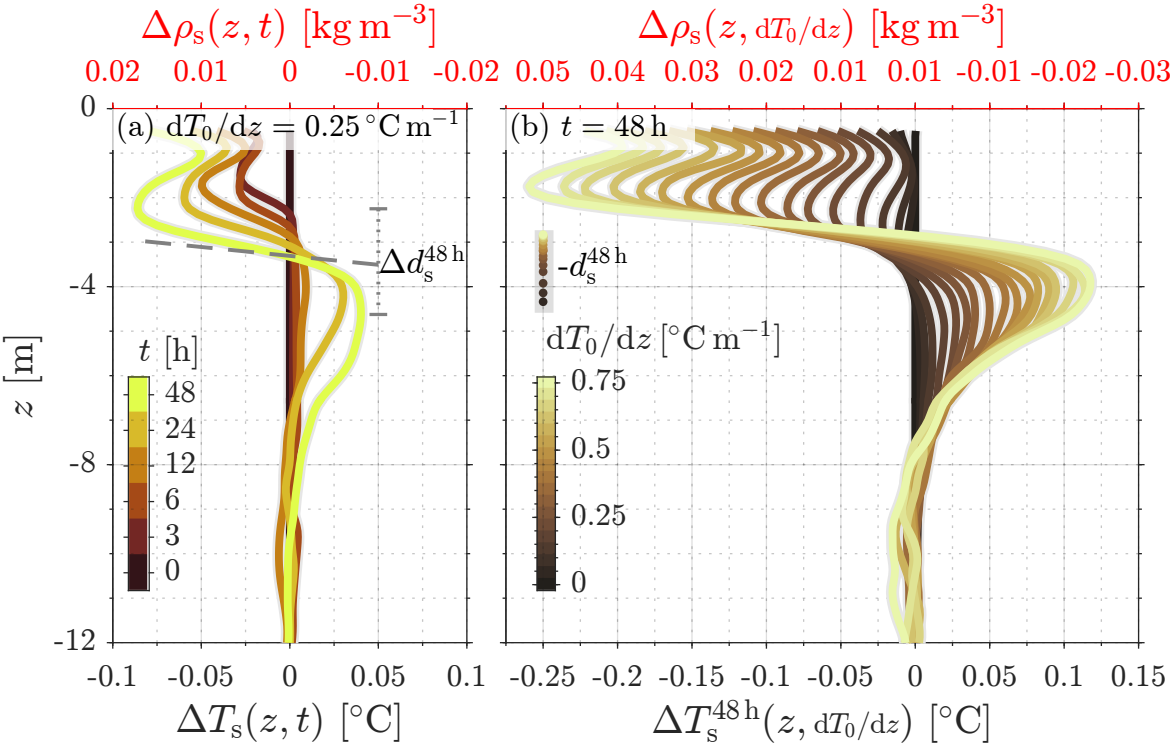

Figure 3.11: Temperature anomaly $\Delta T_s = T_s(z,t) - T_0(z)$ of the sorted state T_s relative to the initial temperature profile for (a) run initialized with dT_0/dz=0.25 °C m^{-1} at several times (colors) showing the effect of irreversible mixing on the background state, and (b) at model time t = 48 h for varying dT_0/dz (colors). In (a) the dashed gray line indicates minimum slope $\partial_z \Delta T_s = -dT_0/dz$ with intercept at the $t = 48$ h zero-crossing depth $z = -d_s^{48\,h}$; the $t = 48$ h vertical extrema separation $\Delta T_s^{48\,h}$ is also shown. In (b) the $t = 48$ h zero-crossing depth $d_s^{48\,h}$ are shown for each dT_0/dz. Note, in the top axes of (a,b) $\Delta\rho_s$ increases right to left.

Domain integrated $BPE_{(x,z)}$ increases more rapidly for larger dT_0/dz (Figure 3.9a & 3.10), indicating increased diapycnal mixing modification of the domain density distribution, and thus the structure of sorted density profile $\rho_s(z,t)$ (3.19). The effect of initial stratification on the Δbpe structure and evolution is evaluated using the sorted density anomaly relative to the initial condition $\rho_0(z)$, $\Delta\rho_s(z,t) = \rho_s(z,t) - \rho_0(z)$. Thus, $\Delta\rho_s(z) = 0$ at $t = 0$. For the linear equation of state (3.2), Δbpe is also characterized by the sorted temperature anomaly

$\Delta T_s(z,t) = T_s(z,t) - T_0(z)$, *i.e.,*

$$\Delta\text{bpe}(z,t) = gz\Delta\rho_s(z,t) \equiv -gz\rho\alpha\Delta T_s(z,t). \tag{3.24}$$

The effect of TRC region mixing on Δbpe is evident in profiles of $\Delta\rho_s$ and ΔT_s (top & bottom axes, Figure 3.11). As surf-zone and TRC mixing modify the inner-shelf temperature, positive near surface density anomaly $\Delta\rho_s$ develops (density increases right-to-left in Figure 3.11a), or negative ΔT_s, indicating dense (colder) fluid raised to higher z-level. A corresponding sub-surface $\Delta\rho_s < 0$ ($\Delta T_s > 0$) also grows, indicating less-dense (warmer) water mixed to lower z-level. The vertical location where $\Delta T_s = 0$ is defined as the zero-crossing depth $z = -d_s$, and indicates the vertical location where the average temperature of fluid mixed in the TRC region intersects the initial condition $T_0(z)$. Above and below $z = -d_s$, ΔT_s has local extrema separated by vertical height Δd_s (right Figure 3.11a). The sub-surface ΔT_s extrema are asymmetric, with larger ΔT_s minima. Sorted isotherms above and below the ΔT_s extrema are compressed causing enhanced sorted stratification $\partial_z T_s(z,t)$ relative to $\mathrm{d}T_0/\mathrm{d}z$. From $3 \le t \le 48$ h, the $\mathrm{d}T_0/\mathrm{d}z = 0.25\ ^\circ\mathrm{C\,m^{-1}}$ zero-crossing depth d_s increases from ≈ 2.5 m to 3.3 m indicating both continuous water-mass transformation and decreasing average temperature of TRC-mixed fluid. The time rate-of-change of d_s is large early on ($t < 3$ h), then decreases and becomes roughly constant after ≈ 12 h (time interval doubles between successive curves in Figure 3.11a). Subsequently, d_s only increases by $\lessapprox 10\%$ between $24 \le t \le 48$ h, consistent with $\partial_t \mathrm{BPE}_{(x,z)}$ becoming constant for $t > 24$ h (Figure 3.9a). At $t = 48$ h, appreciable $\Delta\rho_s$ & ΔT_s are limited to approximately $z > -3d_s$, or $z > -10$ m for $\mathrm{d}T_0/\mathrm{d}z = 0.25\ ^\circ\mathrm{C\,m^{-1}}$ (Figure 3.11a).

Conceptually, TRC-enhanced vertical mixing decreases the $z = -d_s$ sorted density/temperature stratification, *i.e.,* $\partial T_s/\partial z$, relative to the initial stratification $\mathrm{d}T_0/\mathrm{d}z$. The sorted stratification reduction occurs near d_s owing to the exchange flow quantified by $\overline{u}_{\mathrm{EX}}$, which exports mixed fluid with characteristic $T \approx T_0(-d_s)$ from the TRC region, thereby increasing the (x,z)-area

of this water-mass. The increasing area of $T_0(-d_s)$ fluid comes at the expense of the area between isotherms of the stratified fluid from which it was formed, such that sorting decreases the vertical separation between these isotherms and $\partial T_s/\partial z > dT_0/dz$ above and below the ΔT_s extrema. Continuous water-mass transformation also causes the magnitude of ΔT_s extrema to increase with time (Figure 3.11a). Since T_s is positive definite by construction the minimum possible slope is $\partial_z \Delta T_s = -dT_0/dz$ (dashed gray line, Figure 3.11a), implying that $\max\{\Delta T_s\} - \min\{\Delta T_s\} \leq (\Delta d_s\, dT_0/dz)$, where Δd_s quantifies the vertical separation between local ΔT_s extrema (*e.g.,* dotted gray line, Figure 3.11a).

The accumulated effect of TRC-enhanced mixing on Δbpe with varying initial stratification are evaluated using $t = 48$ h profiles of sorted temperature anomaly, denoted $\Delta T_s^{48\,h}$ (Figure 3.11b). The $t = 48$ h zero-crossing, denoted $z = -d_s^{48\,h}$, shoals from $z \approx -4.4$ to ≈ -2.9 m with increasing dT_0/dz (colored dots in Figure 3.11b). Similar to $dT_0/dz = 0.25\ ^\circ\mathrm{C\,m^{-1}}$ (Figure 3.11a), the largest $\Delta T_s^{48\,h}$ are limited to approximately $z > -3d_s^{48\,h}$ for all dT_0/dz; > 12 m for weak dT_0/dz and > 8 m for strong dT_0/dz. The $\Delta T_s^{48\,h}$ extrema also shoal with increasing dT_0/dz, although asymmetrically, with the maxima shoaling 50% more than minima. The vertical separation between extrema $\Delta d_s^{48\,h} \approx 0.72\, d_s^{48\,h}$ for all dT_0/dz. The minimum slope $\partial_z \Delta T_s^{48\,h} \approx -0.5\, dT_0/dz$ for all dT_0/dz is half the minimum possible slope $-dT_0/dz$, suggesting the fluid exported from the TRC region has reduced stratification $\approx N_0^2/2$. The minimum $\partial_z \Delta T_s^{48\,h}$ occur slightly above $z = -d_s^{48\,h}$, *i.e.,* closer to the $\Delta T_s^{48\,h}$ minima (not shown), causing pronounced asymmetry of $\Delta T_s^{48\,h}$ extrema, with the minima on average $1.6\times$ the maxima. The asymmetry is potentially due to the time-dependence of d_s and differences in onshore transport between upper and lower $\langle\bar{\Psi}\rangle$ cells (cf. Figure 3.3g-3.3i), with implications for the structure of available potential energy, discussed next.

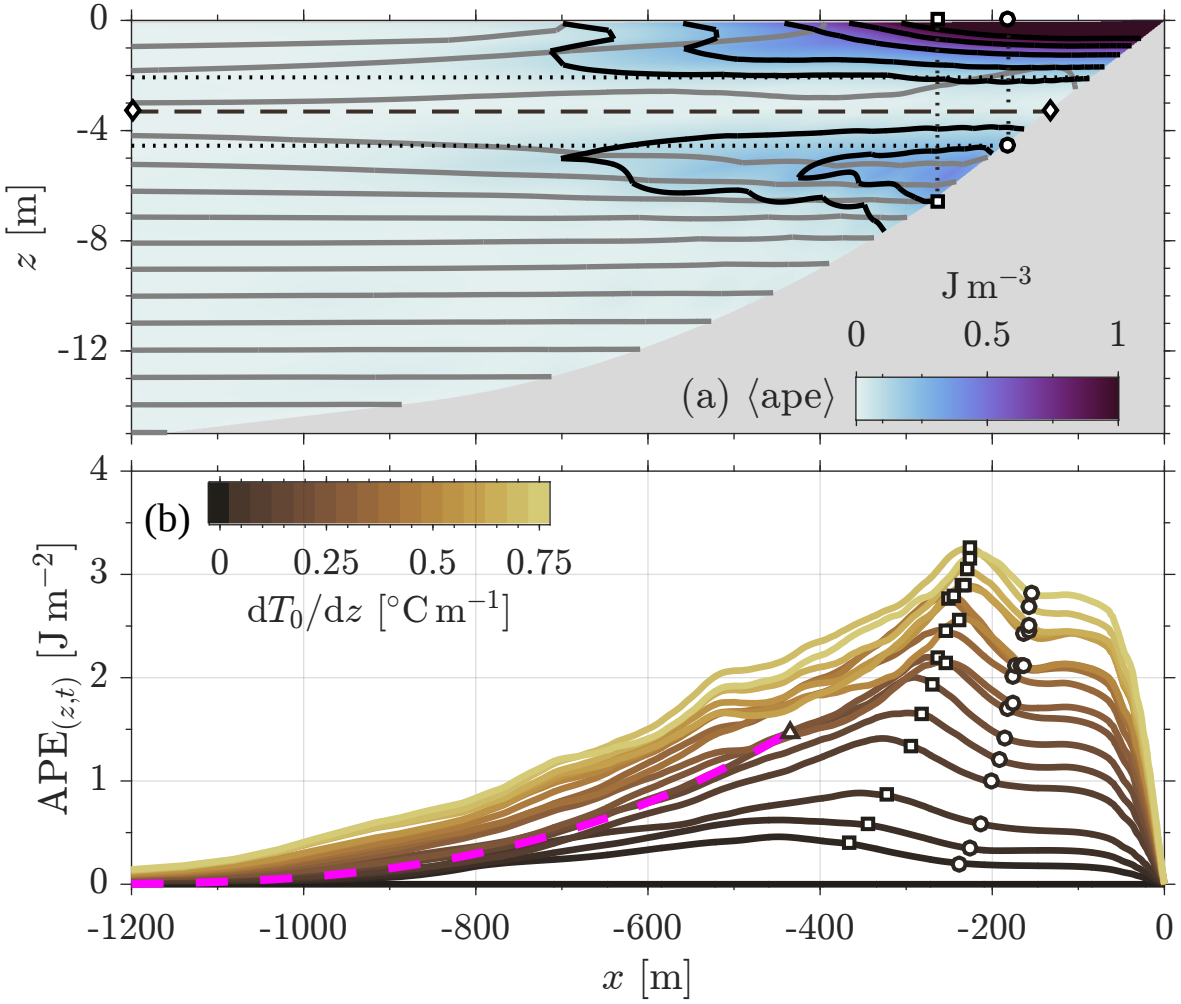

Figure 3.12: (a) Mean available potential energy $\langle \text{ape} \rangle (x,z)$ as function of cross-shore and vertical. Black contours are $\{0.1, 0.25, 0.5, 0.75, 1\}$ J m^{-3}, and gray contours are from corresponding $\langle \bar{T} \rangle$ at 0.25 °C intervals (c.f. Figure 3.3f). (b) Depth integrated APE$_{(z,t)}$ versus cross-shore and dT_0/dz (colors). In (a) the t=48 h zero-crossing depth z=$-d_s^{48\text{h}}$ is indicated by diamonds and horizontal dashed line and the approximate depth of ΔT_s extrema at z=$-(d_s^{48\text{h}} \pm \Delta d_s^{48\text{h}}/2)$ are indicate by horizontal dotted lines. In (a,b) the cross-shore locations where $h(x)$=$2d_s^{48\text{h}}$ & $h(x) = (d_s^{48\text{h}} + \Delta d_s^{48\text{h}}/2)$ are indicated by black square and circle, respectively, with vertical dotted line in (a). Also in (b) is far-field APE$_x^{\text{ff}}$ scaling (3.31) in magenta for h>$3d_s^{48\text{h}}$ and dT_0/dz=0.25 °C m^{-1}.

Specific Available Potential Energy

Localized vertical mixing in the TRC region broadens isotherms toward shore (*e.g.,* Figure 3.3d-f), and the increase of $\overline{u}_{\mathrm{EX}}$ and $\bar{v}$ with $\mathrm{d}T_0/\mathrm{d}z$ are both intimately related to sloping isotherms and thus $\mathrm{APE}_{(x,z)}$. In a domain integrated sense, $\mathrm{APE}_{(x,z)}$ is only 10% of $\mathrm{BPE}_{(x,z)}$, but $\mathrm{ape}(x,z)$ (3.20) serves as an energy reservoir to drive near-field circulation $\bar{\Psi}$ and far-field thermal wind induced $\bar{v}$. The distribution of specific available potential energy is introduced using the mean $\langle \mathrm{ape} \rangle (x,z)$ (3.20) for $\mathrm{d}T_0/\mathrm{d}z = 0.25\ ^{\circ}\mathrm{C\,m^{-1}}$ (Figure 3.12a). Consistent with its definition (3.20), elevated $\langle \mathrm{ape} \rangle$ coincides with regions where $\langle \bar{T} \rangle$ isotherms are sloping (gray contours, Figure 3.12a) and is largest in the TRC-region $x > -4L_{\mathrm{sz}}$. There is an $\langle \mathrm{ape} \rangle$ minimum at $z \approx -3.3$ m coinciding with the $t = 48$ h zero-crossing depth $d_{\mathrm{s}}^{48\,\mathrm{h}}$ (diamond and dashed horizontal line,Figure 3.12a). Above and below $z = -d_{\mathrm{s}}^{48\,\mathrm{h}}$ are two $\langle \mathrm{ape} \rangle$ reservoirs. The $z < -d_{\mathrm{s}}^{48\,\mathrm{h}}$ reservoir occurs where $\langle \bar{T} \rangle > T_{\mathrm{s}}$ and is concentrated where sloping isotherms intersect the bottom, near where $h = 2d_{\mathrm{s}}^{48\,\mathrm{h}}$ (square and dotted vertical line, Figure 3.12a). The $\langle \mathrm{ape} \rangle$ is weak offshore of $x \approx -7L_{\mathrm{sz}}$ and is roughly zero below $z = -3d_{\mathrm{s}}^{48\,\mathrm{h}}$. For $z > -d_{\mathrm{s}}^{48\,\mathrm{h}}$, elevated $\langle \mathrm{ape} \rangle$ is due to $\langle \bar{T} \rangle < T_{\mathrm{s}}$. Onshore of where $h = 2d_{\mathrm{s}}^{48\,\mathrm{h}}$ the temperature anomaly increases and $\langle \mathrm{ape} \rangle \geq 1\ \mathrm{J\,m^{-3}}$ at the surface.

The magnitude and cross-shore structure of $\langle \mathrm{ape} \rangle$ reservoirs with varying $\mathrm{d}T_0/\mathrm{d}z$ are evaluated using depth integrated available potential energy, defined as,

$$\mathrm{APE}_{(z,t)}(x) = \int_{-h}^{\langle \bar{\eta} \rangle} \langle \mathrm{ape} \rangle \, \mathrm{d}z. \tag{3.25}$$

For all $\mathrm{d}T_0/\mathrm{d}z > 0$, maximum $\mathrm{APE}_{(z,t)}$ occurs in the near-field region ($-5L_{\mathrm{sz}} < x < -2L_{\mathrm{sz}}$) and increases from 0.5 $\mathrm{J\,m^{-2}}$ for weakest $\mathrm{d}T_0/\mathrm{d}z$ to 3.25 $\mathrm{J\,m^{-2}}$ for strong stratification. The cross-shore location of $\mathrm{APE}_{(z,t)}$ maxima moves onshore with increasing $\mathrm{d}T_0/\mathrm{d}z$, occurring roughly where $h(x) = 2d_{\mathrm{s}}^{48\,\mathrm{h}}$ (black squares, Figure 3.12b), owing to contributions from both upper and lower $\langle \mathrm{ape} \rangle$ reservoirs (black squares, Figure 3.12a). There is an $\mathrm{APE}_{(z,t)}$ plateau onshore

of $h \approx d_s^{48\,h} + \Delta d_s^{48\,h}/2$ (black circle, Figure 3.12). The plateau results from the upper-$\langle \text{ape} \rangle$ reservoir being surface maximum and weak below $z < -d_s^{48\,h} + \Delta d_s^{48\,h}/2$ (upper dotted horizontal line, Figure 3.12a) such that $\text{APE}_{(z,t)}$ is constant over the narrow cross-shore region where $(d_s^{48\,h} - \Delta d_s^{48\,h}/2) < h(x) < (d_s^{48\,h} + \Delta d_s^{48\,h}/2)$. The ratio of the $\text{APE}_{(z,t)}$ plateau to the $\text{APE}_{(z,t)}$ maximum (circle to square, Figure 3.12b) increases from 0.4 at $\mathrm{d}T_0/\mathrm{d}z = 0.0125\ ^\circ\mathrm{C\,m^{-1}}$ to 0.9 at $\mathrm{d}T_0/\mathrm{d}z = 0.75\ ^\circ\mathrm{C\,m^{-1}}$, indicating a weakening contribution from the lower $\langle \text{ape} \rangle$ reservoir with increasing $\mathrm{d}T_0/\mathrm{d}z$, consistent with asymmetric shoaling of $\Delta T_s^{48\,h}$ extrema (Figure 3.11). Offshore of the maximum, $\text{APE}_{(z,t)}$ decreases over a cross-shore length-scale similar to the cross-shore extent of sloping isotherms (Figure 3.3d-f) that increases with $\mathrm{d}T_0/\mathrm{d}z$, consistent with larger L_R.

3.5 Discussion

3.5.1 Self Similarity of Near-field Stratification and Exchange Flow Structure.

The $\overline{u}_{EX}$ (3.9) scaling with varying $\mathrm{d}T_0/\mathrm{d}z$ (Figures 3.5 & 3.6) suggests the bulk inner-shelf response to TRC-enhanced mixing is self-similar. However, scaling (3.9) was applied to the near-field average $\text{avg}\{\overline{u}_{EX}\}$ to account for the varying location of near-field $\overline{u}_{EX}$ maxima, and the vertical structure of $\langle \bar{u}_L \rangle(z)$ was neglected. Here, the $\Delta T_s^{48\,h}$ zero-crossing depth $d_s^{48\,h}$, which described multiple aspects of the near-field $\langle \text{ape} \rangle(x,z)$ and $\text{APE}_{(z,t)}(x)$ distributions (Figure 3.11b & Figure 3.12a-b), is used to evaluate the self-similar vertical structure of mean stratification $\langle \bar{N} \rangle(z)$ and cross-shore velocity $\langle \bar{u}_L \rangle(z)$. The zero-crossing depth $d_s^{48\,h}$ is used here to re-define the off-shore limit of the near-field to where $h(x) = 3d_s^{48\,h}$, which roughly tracks the varying cross-shore location of $\overline{u}_{EX}$ maxima (not shown).

For $\mathrm{d}T_0/\mathrm{d}z \geq 0.05\ ^\circ\mathrm{C\,m^{-1}}$, $d_s^{48\,h}$ decreases from 4 m to 2.8 m (Figure 3.11b), resulting in maximum $h = 12$ m ($x \approx -6L_{sz}$) for weakest N_0 and minimum $h = 8$ m ($x \approx -3L_{sz}$) for highest

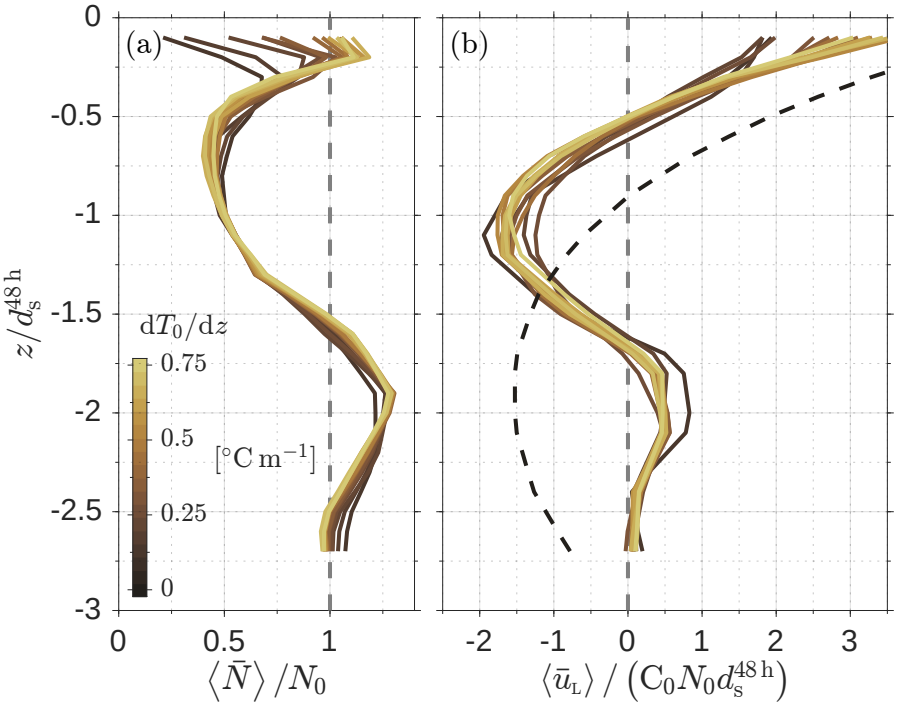

Figure 3.13: (a) Normalized mean stratification $\langle\bar{N}\rangle/N_0$ and (b) normalized mean cross-shore Lagrangian velocity $\langle\bar{u}_L\rangle/\left(C_0N_0d_s^{48\,h}\right)$ versus non-dimensional depth $z/d_s^{48\,h}$ for $\mathrm{d}T_0/\mathrm{d}z \geq 0.05\ ^\circ\mathrm{C\,m^{-1}}$ at the cross-shore location where $h(x)=3d_s^{48\,h}$, which varies from $h=12$ m ($x\approx -6L_{sz}$) to $h=8$ m ($x\approx -3L_{sz}$) for the weakest to strongest N_0. In (b) the unstratified $\mathrm{d}T_0/\mathrm{d}z=0$ simulation at $h(-6L_{sz})\approx 12$ m profile of $\langle\bar{u}_L\rangle/(5\times10^{-4}\ \mathrm{m\,s^{-1}})$ is dashed black.

N_0. Thus, the near-field (x,z)-area shrinks as stratification increases. Profiles of $\langle\bar{N}\rangle$ & $\langle\bar{u}_{\mathrm{L}}\rangle$ are extracted at a virtual mooring located where $h(x) = 3d_{\mathrm{s}}^{48\,\mathrm{h}}$. The mean stratification $\langle\bar{N}\rangle(z)$ is scaled by initial stratification N_0. To account for the shifting cross-shore location of $h = 3d_{\mathrm{s}}^{48\,\mathrm{h}}$, mean Lagrangian velocity $\langle\bar{u}_{\mathrm{L}}\rangle(z)$ is scaled by a modified exchange velocity scale $\left(\mathrm{C}_0 N_0 d_{\mathrm{s}}^{48\,\mathrm{h}}\right)$, where the vertical scale of offshore transport is varied with $\mathrm{d}T_0/\mathrm{d}z$ as $\mathrm{C}_1\tilde{h} = d_{\mathrm{s}}^{48\,\mathrm{h}}$ and constant $\mathrm{C}_0 = 0.04$ is used (see Section 3.3.3). A non-dimensional vertical coordinate $z/d_{\mathrm{s}}^{48\,\mathrm{h}}$ is also used to account for varying $h = 3d_{\mathrm{s}}^{48\,\mathrm{h}}$ with $\mathrm{d}T_0/\mathrm{d}z$ (Figure 3.13). Note, the variation in $d_{\mathrm{s}}^{48\,\mathrm{h}}$ is much weaker than N_0.

Normalized mean stratification profiles are self-similar below $z/d_{\mathrm{s}}^{48\,\mathrm{h}} \approx -0.35$. Sub-surface stratification is reduced for $-1 < z/d_{\mathrm{s}}^{48\,\mathrm{h}} < -0.5$, and slightly enhanced for $z/d_{\mathrm{s}}^{48\,\mathrm{h}} < -1.5$. The minimum $\langle\bar{N}\rangle/N_0 \approx 0.5$ occurs slightly above $z/d_{\mathrm{s}}^{48\,\mathrm{h}} = -1$, consistent with the minimum $\partial_z \Delta T_{\mathrm{s}}^{48\,\mathrm{h}}$ occurring shallower than $d_{\mathrm{s}}^{48\,\mathrm{h}}$ (Figure 3.11), potentially due to aliasing of d_{s} time-dependence. As d_{s} growth is large until $t > 12$ h, fluid exported offshore earlier than $t \approx 24$ h would occupy depth shallower than $z/d_{\mathrm{s}}^{48\,\mathrm{h}} = 1$. Near-surface stratification is also reduced for small $\mathrm{d}T_0/\mathrm{d}z$, owing to the proximity of where the well-mixed fluid intersects the surface and due to larger near surface $\langle\bar{K}_{\mathrm{V}}\rangle$ for weak N_0 (*e.g.,* Figure 3.3a). Below $z/d_{\mathrm{s}}^{48\,\mathrm{h}} = -1.5$, stratification is elevated, reaching $\langle\bar{N}\rangle/N_0 \approx 1.25$ at $z/d_{\mathrm{s}}^{48\,\mathrm{h}} \approx -2$, consistent with the compressed $\langle\bar{T}\rangle$ isotherms and elevated $\mathrm{rms}\{T\}$ at depth (Figure 3.4a).

The non-dimensional cross-shore velocity $\langle\bar{u}_{\mathrm{L}}\rangle/\left(\mathrm{C}_0 N_0 d_{\mathrm{s}}^{48\,\mathrm{h}}\right)$ is also self-similar for $\mathrm{d}T_0/\mathrm{d}z \geq 0.05\ ^{\circ}\mathrm{C\,m^{-1}}$, and has a 3-layer exchange flow structure with near-surface and bottom onshore flow and offshore flow in between (Figure 3.13b). Substitution $\mathrm{C}_1\tilde{h} = d_{\mathrm{s}}^{48\,\mathrm{h}}$ slightly improves the $\langle\bar{u}_{\mathrm{L}}\rangle$ collapse relative to constant $C_1\tilde{h} = \tilde{h}/3$, where $\tilde{h} = 8.25$ m is the $-5L_{\mathrm{sz}} < x < -2L_{\mathrm{sz}}$ average depth. Near-surface ($z/d_{\mathrm{s}}^{48\,\mathrm{h}} > -0.5$), onshore flow is strong, with maximum $\langle\bar{u}_{\mathrm{L}}\rangle/\left(\mathrm{C}_0 N_0 d_{\mathrm{s}}^{48\,\mathrm{h}}\right) \approx 3$. The maximum offshore flow occurs at $z/d_{\mathrm{s}}^{48\,\mathrm{h}} \approx -1$, with $\langle\bar{u}_{\mathrm{L}}\rangle/\left(\mathrm{C}_0 N_0 d_{\mathrm{s}}^{48\,\mathrm{h}}\right) \approx -1.5$ or $1/2$ the surface maximum. Below $z/d_{\mathrm{s}}^{48\,\mathrm{h}} = -1.5$, flow becomes onshore again with a weak maximum $\langle\bar{u}_{\mathrm{L}}\rangle/\left(\mathrm{C}_0 N_0 d_{\mathrm{s}}^{48\,\mathrm{h}}\right) \approx 0.5$ at $z/d_{\mathrm{s}}^{48\,\mathrm{h}} = -2$. The offshore directed maximum roughly coincides with

the $\langle \bar{N} \rangle / N_0$ minimum, indicating subsurface export of relatively low stratification (mixed) fluid, consistent with previous TRC exchange modeling (Kumar and Feddersen, 2017c; Grimes et al., 2020c). The relative strength of near-surface onshore transport ($z/d_s^{48\,\mathrm{h}} > -0.5$) compared to sub-surface onshore transport ($z/d_s^{48\,\mathrm{h}} < -1.5$) implies stratified near-surface fluid is the dominant source to TRC region.

The 3-layer exchange flow for stratified cases is contrasted by the unstratified 2-layer $\langle \bar{u}_\mathrm{L} \rangle$ profile at $x = -6L_{\mathrm{sz}}$ (black dashed, Figure 3.13b), which is characteristic of Stokes drift and quasi-uniform undertow velocity profile (*e.g.,* Lentz et al., 2008; Hally-Rosendahl et al., 2014). The 3-layer to 2-layer differences between stratified and unstratified $\langle \bar{u}_\mathrm{L} \rangle$ indicate different dynamics. The occurrence of low $\langle \bar{N} \rangle / N_0$ where $\langle \bar{u}_\mathrm{L} \rangle / \left(\mathrm{C}_0 N_0 d_s^{48\,\mathrm{h}} \right)$ is offshore and vice-verse is qualitatively consistent with gravity current intrusion into stratified ambient (*e.g.,* Bolster et al., 2008). However, direct analogy between lock-release initial condition and time-dependent spin-up of continuous TRC mixing cannot be made. As the intrusion has reduced stratification $\langle \bar{N} \rangle / N_0 \approx 1/2$, the estimated Froude number $\mathrm{C}_0 = 0.04$ increases to 0.1 which is still small relative to lock-release pressure/advection balance, indicating additional dynamics. The advective speed $0.04\,(N_0 d_\mathrm{s})$ is also small relative to the background mode-1 internal wave phase speed $\approx N_0 d_\mathrm{s}$ (*e.g.,* White and Helfrich, 2008), suggesting radiated internal waves may contribute to the gravitational adjustment of the TRC mixed fluid. Also, since the time average is over $t =$ 24-48 h, when far-field sloping isotherms are in thermal wind balance, the cross-shore speed can be reduced due to potential vorticity dynamics (*e.g.,* Thomas and Linden, 2007). The addition of inner-shelf eddy activity in the TRC region ($x > -4L_{\mathrm{sz}}$) also adds further complexity to the momentum balance.

Assuming the near-field region is bounded offshore by $h = 3d_\mathrm{s}$, with onshore (x,z)-area of roughly $(9/2)\,(d_\mathrm{s})^2/\beta_{\mathrm{SZ}}$ and bottom slope $\beta_{\mathrm{SZ}} = 0.025$, the modified exchange flow scaling

implies a near-field flushing time-scale,

$$\mathcal{T}_{\mathrm{f}} \sim \frac{9}{2}\frac{(d_{\mathrm{s}})^2/\beta_{\mathrm{sz}}}{d_{\mathrm{s}}\,(\mathrm{C_0N_0}d_{\mathrm{s}})} = \frac{9}{2}(\beta_{\mathrm{sz}}\mathrm{C_0}N_0)^{-1}. \tag{3.26}$$

Thus, increasing $\mathrm{d}T_0/\mathrm{d}z$ (larger N_0) decreases the flushing time $\mathcal{T}_{\mathrm{f}}$ due to enhanced u_{EX} and decreased near-field area (smaller d_{s}). Using modeled $d_{\mathrm{s}}^{48\,\mathrm{h}}$, $\mathcal{T}_f$ ranges from 11 d (weak N_0) to 1.5 d (strong N_0). These flushing time-scales are relatively large compared to estimates based on thermally driven cross-shelf transport (Molina et al., 2014). However, the periodic reversal of diurnal thermal exchange has potential to recirculate tracer, which is contrasted by the persistent TRC driven offshore transport within sub-surface intrusion (*e.g.,* Grimes et al., 2020c).

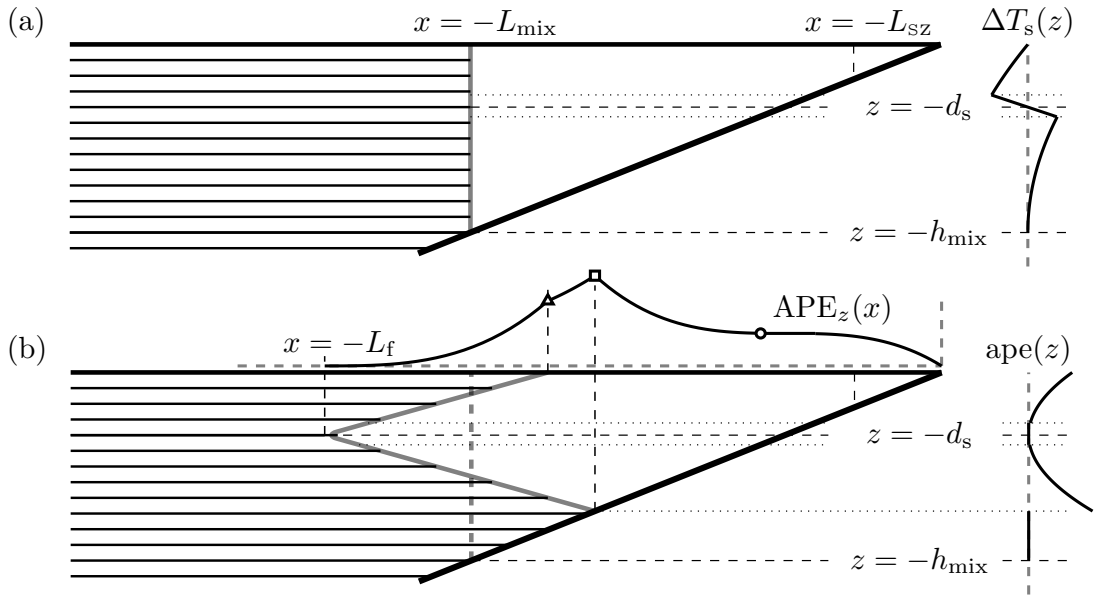

Figure 3.14: (a) Idealized well-mixed wedge driven by TRC-induced mixing of temperature onshore of $x{=}{-}L_{\mathrm{mix}}$ with the associated sorted temperature anomaly ΔT_{s} (right). (b) Idealized offshore intrusion of well-mixed fluid, with the vertical structure of $\mathrm{ape}(z)$ for the well-mixed wedge (right) and the cross-shore $\mathrm{APE}_z(x)$ structure (above). In (a-b), the zero-crossing depth d_{s} (denoted d_{mix} in 3.6-3.6) and mixed region depth $h_{\mathrm{mix}}{=}3d_{\mathrm{s}}$ are indicated with horizontal dashed black line, and the location of the upper and lower bounds $(d_{\mathrm{s}} \pm \Delta d_{\mathrm{s}}/2)$ (denoted $d_{\mathrm{mix}}^{+/-}$ in 3.6-3.6) of the unstratified $T_{\mathrm{s}}(z)$ region are indicated with horizontal dotted lines. In (b), the cross-shore location of the surface front (triangle), bottom front (square) and plateau (circle) are shown, roughly corresponding to markers in Figure 3.12b, the offshore apex at $x{=}-L_{\mathrm{f}}$ is also indicated.

3.5.2 Relating Zero-Crossing Depth d_s to Initial Stratification.

The ΔT_s zero-crossing depth d_s characterizes multiple aspects of the inner-shelf response to TRC-enhanced mixing, *e.g.,* the $\text{APE}_{(z,t)}$ maximum near $h(x) = 2d_s^{48\,h}$ and self-similarity of $\langle \bar{N} \rangle$ and $\langle \bar{u}_L \rangle$ profiles at $h(x) = 3d_s^{48\,h}$. A simplified domain with constant bathymetric slope $h(x) = -\beta x$ that extends offshore to $x = -L_x$ with maximum depth $h_{max} = \beta L_x$ is used to relate TRC region mixing to the specific background potential energy distribution through the sorted temperature anomaly ΔT_s and zero-crossing depth d_s (Figure 3.14a). Surf-zone and TRC-induced mixing is idealized by homogenizing the constant stratification initial temperature $T_0(z)$ (3.1) within the wedge formed by a vertical offshore front at $x = -L_{mix}$ (Figure 3.14a). Derivations are given in 3.6, with d_s denoted d_{mix}. The idealized well-mixed wedge can be thought of as the short time-scale effect of TRC-region mixing (*e.g.,* $t < 3$ h Figure 3.9a-b), before the development of inner-shelf $\bar{\Psi}(x,z,t)$ and $\bar{v}(x,z,t)$. The well-mixed fluid has uniform temperature $T_{mix} = T_0(-d_s)$, where $d_s = \beta L_{mix}/3$ (3.38) is the ΔT_s zero-crossing depth for the idealized well-mixed wedge. With these assumptions, analytical expressions for the sorted temperature profile $T_s(z)$ (3.50), and $\Delta T_s(z)$ (right of Figure 3.14a), vary depending on d_s and with the parameter $\varepsilon_z = d_s/h_{max}$, quantifying the ratio of the zero-crossing depth to the maximum offshore domain depth. The idealized ΔT_s profile is qualitatively consistent with the modeled ΔT_s curves in many respects, with ΔT_s extrema above and below d_s and $\Delta T_s = 0$ below $z = -3d_s = h_{mix}$ (right of Figure 3.14a; and Figure 3.11). For the idealized T_s profile, the region $(-d_s - \Delta d_s/2) < z < (-d_s + \Delta d_s/2)$ has minimum possible $\partial T_s/\partial z = 0$ and $\partial_z \Delta T_s = -\mathrm{d}T_0/\mathrm{d}z$ owing to the idealized wedge being perfectly-mixed and smaller than the $t = 48$ h modeled slope (Figure 3.11a).

Here, the potential energy change associated with homogenizing $x > -L_{mix}$ is used to relate modeled zero-crossing depth d_s to the initial stratification $\mathrm{d}T_0/\mathrm{d}z$. The potential energy change is assumed to depend on the eddy kinetic energy flux from the surf-zone to inner-shelf, *i.e.,*

$$\text{PE}^{mix}_{(x,z)} \propto \tau_{mix}\, \text{F}^{(sz)}_{eke}, \tag{3.27}$$

where τ_{mix} is the idealized wedge mixing time-scale and $\mathrm{F}_{\text{eke}}^{(\text{sz})} = \mathrm{F}_{\text{eke}}(x = -L_{\text{sz}})$. Based on the time-scale for $\mathrm{EKE}_{(x,z)}$ to spin-up (Figure 3.8b), τ_{mix} is approximately 1 h and does not vary with $\mathrm{d}T_0/\mathrm{d}z$. The wedge mixing time-scale τ_{mix} is short relative to the $\mathcal{T}_{\text{f}} > 24$ h (3.26) flushing time-scale that would modify the vertical offshore front in the idealized well-mixed wedge. Since F_{eke} is also constant across simulations (Figure 3.8c), (3.27) implies $\mathrm{PE}_{(x,z)}^{\text{mix}}$ is constant. For the idealized well-mixed wedge with $T_{\text{mix}} = T_0(-d_{\text{s}})$ and linear temperature dependent equation of state (3.2),

$$\begin{aligned}
\mathrm{PE}_{(x,z)}^{\text{mix}} &= \int_{-L_{\text{mix}}}^{0}\int_{-h(x)}^{0} g\,z\,[\rho_0(-d_{\text{s}}) - \rho_0(z)]\,\mathrm{d}z\,\mathrm{d}x, \\
&= \frac{1}{36}\rho\beta^3 N_0^2 L_{\text{mix}}^4, \qquad (3.28) \\
&= \frac{9}{4}\rho\beta^{-1} N_0^2 d_{\text{s}}^4. \qquad (3.29)
\end{aligned}$$

As the offshore region $x < -L_{\text{mix}}$ is unchanged, $\mathrm{PE}_{(x,z)}^{\text{mix}}$ is a both a measure of the potential energy change of the idealized wedge and the entire domain. Combining (3.29) with (3.27) gives,

$$\{d_{\text{s}}, L_{\text{mix}}\} \propto (\tau_{\text{mix}}\,\mathrm{F}_{\text{eke}}^{(\text{sz})})^{1/4}(\rho\,N_0^2)^{-1/4}. \qquad (3.30)$$

As such, d_{s} is expected to decrease as stratification increases, and increase with increasing $\mathrm{F}_{\text{eke}}^{(\text{sz})}$. The $\mathrm{d}T_0/\mathrm{d}z \geq 0.05\ ^{\circ}\mathrm{C\,m^{-1}}$ model $d_{\text{s}}^{48\,\text{h}}$ (Figure 3.11b) is roughly consistent with (3.30), with skill-score of 0.60. Modifying (3.30) to $(d_{\text{s}}^{48\,\text{h}} - d_0) \propto \mathrm{d}T_0/\mathrm{d}z^{-1/4}$ with $\mathrm{d}_0 = 1.4$ m and proportionality constant 0.94 $\mathrm{m^2\,C^{-1}}$, improves the skill to 0.98. The additional length-scale d_0 for large-stratification may depend on the surf-zone depth $h_{\text{sz}} = \beta_{\text{sz}} L_{\text{sz}}$, such that if inner-shelf mixing is suppressed to the point of $d_{\text{s}} \approx h_{\text{sz}}$ then the only source of mixing is the turbulent surf-zone. Thus, (3.30) scales the change in d_{s} due to the effect of varying $\mathrm{d}T_0/\mathrm{d}z$ on inner-shelf TRC-enhanced mixing. The decrease in the (x,z)-extent of elevated $\langle \bar{K}_{\text{v}} \rangle$ with increasing $\mathrm{d}T_0/\mathrm{d}z$ (Figure 3.3a-c) is consistent with decrease in both $\{d_{\text{s}}, L_{\text{mix}}\}$ with $\mathrm{d}T_0/\mathrm{d}z$, as are the onshore

movement of $\overline{u}_{\mathrm{EX}}$ and $\mathrm{APE}_{(z,t)}$ maxima. Thus, the vertical length scale d_{s} delimiting the near-field, $h < 3d_{\mathrm{s}}$, and determining the vertical structure z/d_{s} of inner-shelf response is related to the surf-zone to inner-shelf TRC eddy kinetic energy flux $\mathrm{F}_{\mathrm{eke}}^{(\mathrm{sz})}$ and initial stratification N_0 through the work done in mixing an idealized well-mixed wedge. However, the idealized well-mixed wedge does not account several dynamical aspects of the mean inner-shelf response to TRC-region mixing, *e.g.,* the far-field intrusion, which are addressed next.

3.5.3 Idealized Cross-shore $\mathrm{APE}_{(z,t)}(x)$ Structure.

The modeled far-field mean $\langle \bar{T} \rangle$ isotherms broaden toward shore (Figure 3.3d-f), and the far-field thermal wind shear is related to $\mathrm{d}T_0/\mathrm{d}z$ through isotherm slope scaling $\mathrm{d}z/\mathrm{d}x = f/N_0$ (3.11). This implies that while the vertical scale height d_{s} decreases with increasing $\mathrm{d}T_0/\mathrm{d}z$ the offshore extent of TRC-mixed water-mass increases with $\mathrm{d}T_0/\mathrm{d}z$ owing to larger L_{R}. In the idealized well-mixed wedge case (Figure 3.14a) both d_{s} and L_{mix} decreased and with increasing $\mathrm{d}T_0/\mathrm{d}z$, which is inconsistent with growing offshore extent for $t \gg \tau_{\mathrm{mix}}$. Insight to the mean cross-shore $\mathrm{APE}_{(z,t)}(x)$ distribution, a measure of sloping isotherms and driver of inner-shelf mean circulation, is developed by transforming the vertical front at $x = -L_{\mathrm{mix}}$ to an idealized intrusion sloping symmetrically about $z = -d_{\mathrm{s}}$ (Figure 3.14b). Holding $A_{\mathrm{mix}} = (9/2)d_{\mathrm{s}}/\beta$ and thus d_{s} constant for simplicity, the apex of the idealized intrusion at $x = -L_{\mathrm{f}}$ moves offshore as the intrusion slope $\mathrm{d}z/\mathrm{d}x = f/N_0$ decreases (3.57)-(3.61). For simplicity adjustment of isotherms outside of the idealized intrusion are neglected, meaning the adiabatic transformation from idealized well-mixed wedge to idealized intrusion decreases the domain integrated available potential energy, which is qualitatively consistent with conversion to inner-shelf mean circulation.

Here, idealized intrusion ape and APE_z scalings are summarize, detailed derivations are found in 3.6. To leading order in $\varepsilon_z = d_{\mathrm{s}}/h_{\mathrm{mix}}$, the specific available potential energy within the idealized well-mixed wedge and intrusion scales as $\mathrm{ape}(z) \propto \rho N_0^2 (z + d_{\mathrm{s}})^2$ (3.51), and is concentrated in two reservoirs above and below d_{s} (right, Figure 3.14b), roughly consistent with modeled

$\langle \text{ape} \rangle$ (Figure 3.12a). Vertically integrating ape(z) over the well-mixed wedge and intrusion gives $\text{APE}_z(x)$, which at leading order is proportional to $\rho N_0^2 d_s^3$ with cubic dependence on sloping boundaries, *e.g.,* $h(x)$ in (3.54) and (3.62). Similar to modeled $\text{APE}_{(z,t)}(x)$ (Figure 3.12b), moving away from shore $\text{APE}_z(x)$ plateaus where $(d_s - \Delta d_s/2) < h(x) < (d_s + \Delta d_s/2)$ (dotted lines horizontal lines, Figure 3.14b) then increases again for $h(x) > d_s + \Delta d_s/2$ (circle, Figure 3.14b). For the idealized well-mixed intrusion, maximum $\text{APE}_z(x) \propto \rho N_0^2 d_s^3$ occurs at $h < 3d_s$ where the vertical thickness of the well-mixed fluid is largest (square, Figure 3.14b). The maximum vertical thickness depends on the where the idealized well-mixed intrusion intersects the surface and bottom (triangle and square, Figure 3.14b) and varies with f/N_0 (3.62). For large N_0 the front locations approach the TRC region and surf-zone, where strong mixing would limit further onshore progression, required further constraints not considered here. The modeled $\text{APE}_{(z,t)}$ maxima occur near $h(x) = 2d_s^{48\,\text{h}}$ (squares, Figure 3.12b), and are well represented by the leading order idealized intrusion dependence $\max\{\text{APE}_z(x)\} \propto \rho N_0^2 d_s^3$, with best fit proportionality constant 0.12 for all $\text{d}T_0/\text{d}z > 0$, giving $r^2 = 0.99$ and skill score 0.97.

Restricting attention to the far-field region, defined here as where the idealized intrusion is symmetric about $z = -d_s$ with vertical thickness is $H(x) = 2f/N_0(x + L_f)$ (3.56) (offshore of $\triangle$, Figure 3.14b), the idealized intrusion APE_z varies as (3.63),

$$\text{APE}_z^{\text{ff}} \propto \rho N_0^2 d_s^3 \left[1 + (x - x_0)/L_R\right]^3, \tag{3.31}$$

with x_0 corresponding to the triangle in Figure 3.14b and using a the internal deformation radius $L_R = d_s N_0/f$. This functional dependence is shown in Figure 3.12b (dashed magenta) for $\text{d}T_0/\text{d}z = 0.25\ ^\circ\text{C}\,\text{m}^{-1}$, with $h(x_0) = 3d_s^{48\,\text{h}}$ and $L_R = d_s^{48\,\text{h}} N_0/f$, and reproduces the offshore decay in modeled $\text{APE}_{(z,t)}$. However, the parameters x_0 and proportionality constant (0.1) vary with $\text{d}T_0/\text{d}z$ due to additional near-field dynamics. Thus, the idealized well-mixed intrusion is qualitatively consistent with the modeled isotherms broadening with aspect ratio d_s/L_r and

varying with initial stratification N_0, and zero-crossing depth d_s (a function of both dT_0/dz and $F_{eke}^{(sz)}$).

3.5.4 Scaling Incident Wave Effects on Stratified Inner-shelf Response

Using a simplified representation of TRC mixing of inner-shelf temperature, the length scale d_s characterizing the cross-shore and vertical structure of inner-shelf response was related to the work done in mixing through F_{eke} (Section 3.5.2). The incident wave forcing was kept constant for all simulations and F_{eke} was essentially unaffected by the large range of dT_0/dz (Section 3.4.1). Thus, the derived near-field exchange velocity $\overline{u}_{EX}$ scaling (3.9) and far-field alongshore thermal wind $\bar{v}$ scaling (3.12) do not explicitly relate the inner-shelf circulation $\langle \bar{u}_L \rangle$, $\langle \bar{v} \rangle$ and stratification $\langle \bar{N} \rangle$ response to the incident waves that force TRCs. However, these scalings implicitly depend on the magnitude of wave and TRC forcing, through the surf-zone to inner-shelf eddy kinetic energy flux $F_{eke}^{(sz)}$ and zero-crossing depth d_s. Based on energy arguments, the zero-crossing depth roughly scales as $d_s \propto (F_{eke}^{(sz)})^{1/4}$ (3.30). Here, we explore how variations in incident wave conditions, *e.g.,* wave height H_{sz}, offshore wave-length $L_\infty = gT_p$ or peak period T_p, and directional spread σ_θ, affect F_{eke} and in turn the zero-crossing depth d_s. For simplicity, the surf-zone depth $h_{sz} = (\beta_{sz} L_{sz})$ is determined from wave height using constant ratio $H_{sz}/h_{sz} = \gamma_{sz} = 0.4$.

The cross-shore directed eddy kinetic energy flux from surf-zone to inner-shelf $F_{eke}^{(sz)}$ is scaled as,

$$F_{eke}^{(sz)} \approx \rho\, h_{sz}\, \mathrm{rms}\{U_{sz}^{(rot)}\}^3, \tag{3.32}$$

where $\mathrm{rms}\{U_{sz}^{(rot)}\}$ is the quadratic alongshore mean (rms) of barotropic rotational horizontal velocity, *i.e.,* neglecting wave orbital and Stokes-undertow velocities. The third-moment of $U_{sz}^{(rot)}$ is non-zero owing to strong, concentrated offshore flow and generally weaker and broader onshore flow, and approximated using $\mathrm{rms}\{U_{sz}^{(rot)}\}^3$. Based on 2D TRC-resolving simulations, Suanda

and Feddersen (2015) found that the cross-shore distribution of barotropic cross-shore exchange velocity is self-similar over broad range of incident wave and beach slope variations, and well represented by Gaussian form,

$$U_{\rm EX}(x) = U_0^{\rm (rot)} \exp\left[-\frac{(x-x_0)^2}{L_d^2}\right], \tag{3.33}$$

where $U_0^{\rm (rot)}$ is a rotational velocity scale, x_0 the location of maximum velocity, and $L_{\rm d}$ the offshore decay length-scale. The Gaussian form (3.33) also represented the distribution of rms$\{U_{\rm sz}^{\rm (rot)}\}$ with different dimensional coefficients,

$$\begin{aligned} U_0^{\rm (rot)} &= {\rm C}_4\,\sigma_\theta\sqrt{g\,h_{\rm sz}}\,[1+70\,S_{\rm sz}], && (3.34)\\ x_0 &= -{\rm C}_5\frac{h_{\rm sz}}{\beta_{\rm SZ}}\left[1+0.005\,S_{\rm sz}^{-1}\right], && (3.35)\\ L_{\rm d} &= {\rm C}_6\frac{h_{\rm sz}}{\beta_{\rm SZ}}{\rm Ir}\,\sigma_\theta^{-1/4}\left[1+22\,S_{\rm sz}^{1/2}\right], && (3.36) \end{aligned}$$

where wave directional spread σ_θ describes whether waves are long- (small σ_θ) or short-crested (large σ_θ), and Iribarren number ${\rm Ir} = \beta_{\rm SZ}/S_{\rm sz}^{1/2}$ relates the bottom slope to the wave steepness at breaking $S_{\rm sz} = H_{\rm sz}/L_\infty$. The modified non-dimensional coefficients $\{{\rm C}_4,{\rm C}_5,{\rm C}_6\} = \{0.1075, 0.37, 0.77\}$ minimize the squared error between (3.33) and the ensemble average ${\rm F}_{\rm eke}(x)$ (Figure 3.8c) and decently reproduce the modeled ${\rm F}_{\rm eke}(x)$ magnitude and distribution.

The surf-zone and TRC mixing effects on the inner-shelf have functional dependence on the incident wave field. Focusing on incident wave height and directional spread dependence, *i.e.,* constant period (and L_∞) and beach slope $\beta_{\rm SZ}$, relations (3.32)-(3.36) give,

$$d_{\rm s} \propto (g^{3/2}N_0^{-2}\tau_{\rm mix})^{1/4}\sigma_\theta^{3/4}\,(H_{\rm sz})^{5/8}\,[1+70\,S_{\rm sz}]^{3/4}\exp\left[-\frac{3}{4}H_{\rm sz}\sigma_\theta^{1/2}\,\mathcal{F}\right], \tag{3.37}$$

where function $\mathcal{F}(H_{\rm sz}, L_\infty, \beta_{\rm SZ})$ varies weakly with $H_{\rm sz}$. The wave height increases $d_{\rm s}$ owing

to increase in $U_0^{(\mathrm{rot})}$, h_{sz} and L_{d}. Directional spread also increases d_{s} due to larger $U_0^{(\mathrm{rot})}$, but decreases the decay length-scale L_{d}, *i.e.,* TRC region closer to shore. The leading H_{sz} dependence of exp[ ] in (3.37) is due to the numerator $(x-x_0)^2 \propto H_{\mathrm{sz}}^2$ and denominator $L_{\mathrm{d}}^2 \propto H_{\mathrm{sz}}$, whereas $\sigma_\theta^{1/2}$ dependence is due to $L_{\mathrm{d}} \propto \sigma_\theta^{-1/4}$. With modeled wave conditions $H_{\mathrm{sz}} = 1$ m, $\mathrm{T_p} = 10$ s and $\sigma_\theta = 10$ degrees, (3.37) implies that $\pm 25\%$ variation in H_{sz} induces $\pm 18\%$ change in d_{s}, to within 1% holding $\mathcal{F}$ constant. Alternatively, varying σ_θ by $\pm 25\%$ induces $\pm 15\%$ change in d_{s}.

3.6 Summary

Idealized simulations were analyzed to determine the bulk (or mean) effects of TRC-enhanced mixing on inner-shelf stratification and circulation using relatively simple energy arguments and existing scalings. Domain integrated eddy kinetic energy equilibrates in 1 h, and depth integrated cross-shore eddy kinetic flux is independent of $\mathrm{d}T_0/\mathrm{d}z$ and decays to near-zero within $4L_{\mathrm{sz}}$ (400 m). TRC-driven mixing onshore of $\approx 3L_{\mathrm{sz}}$ induces a cross-shore density gradient that drives inner-shelf circulation. In the near-field ($-5L_{\mathrm{sz}} < x < -2L_{\mathrm{sz}}$), a 3-layer cross-shore exchange flow $\langle \bar{u}_{\mathrm{L}} \rangle$ transports mixed fluid offshore with reduced stratification $\langle \bar{N} \rangle / N_0 \approx 1/2$, with exchange velocity $\overline{u}_{\mathrm{EX}}$ scaling proportional to N_0, consistent with intrusive stratified gravity current. Farther offshore, far-field ($x < -5L_{\mathrm{sz}}$) mean isotherms broaden toward shore, and are in approximate geostrophic balance with alongshore flow $\langle \bar{v} \rangle$. Based on the thermal wind relation, with isotherm slope scaling $\mathrm{d}z/\mathrm{d}x = f/N_0$, far-field maximum alongshore velocity scales with N_0.

The TRC-driven mixing increased domain background potential energy, quantified through sorted temperature (or density) anomaly $\Delta T_{\mathrm{s}}(z)$. The ΔT_{s} zero-crossing depth d_{s} characterized the self-similar near-field response, delimited a posteriori as where $h(x) = 3d_{\mathrm{s}}$. The $t = 48$ h modeled zero-crossing depth $d_{\mathrm{s}}^{48\mathrm{h}}$ decreased with initial stratification, indicating shrinking near-field region with increasing $\mathrm{d}T_0/\mathrm{d}z$. Vertical profiles of non-dimensional mean $\langle \bar{N} \rangle / N_0$ and cross-

shore velocity $\langle \bar{u}_{\mathrm{L}} \rangle / \bar{u}_{\mathrm{EX}}$ at $h(x) = 3d_{\mathrm{s}}^{48\,\mathrm{h}}$ collapse with non-dimensional depth $z/d_{\mathrm{s}}^{48\,\mathrm{h}}$. Based on the work done by short time-scale $O(1\ \mathrm{h})$ TRC-driven mixing of an idealized wedge, the zero-crossing depth d_{s} scales as $(\mathrm{F_{eke}})^{1/4}(\mathrm{d}T_0/\mathrm{d}z)^{-1/4}$. A modified scaling $d_{\mathrm{s}} \approx d_0[1 + \mathrm{d}T_0/\mathrm{d}z^{-1/4}]$ reproduced the modeled $d_{\mathrm{s}}^{48\,\mathrm{h}}$ suggesting an additional length-scale, potentially related to incident wave and surf-zone characteristics. At longer time-scales > 24 h, cross-shore exchange flow modifies the distribution of TRC-mixed fluid forming a far-field intrusion. The modeled cross-shore distribution of available potential energy is qualitatively consistent with transformation the idealized well-mixed wedge to offshore well-mixed intrusion with characteristic aspect ratio $\mathrm{d}z/\mathrm{d}x = f/N_0$.

Results indicate that inner-shelf available and background potential energy respond rapidly to surf-zone and TRC-induced mixing (a few hours), but following an inertial period (f^{-1}) the shoreward broadening isotherms approach geostrophic balance and the potential energy growth rate decreases, becoming roughly constant. This state of quasi-equilibrium is characterized by a 3-layer cross-shore exchange flow that exports mixed fluid with $N/N_0 \approx 0.5$ offshore sub-surface (over $-1.5d_{\mathrm{s}} < z < -0.5d_{\mathrm{s}}$) and re-supplies the TRC-driven mixing region with stratified fluid $N \approx N_0$ from above and below the intrusion ($z > -0.5d_{\mathrm{s}}$ and $z < -1.5d_{\mathrm{s}}$, respectively). The re-supply of stratified fluid to be vertically mixed sustains the cross-shore sloping isotherms.

The mean $t = 24$-48 h offshore extent of inner-shelf response was characterized by the internal Rossby deformation radius $L_{\mathrm{R}}^{48\,\mathrm{h}} = d_{\mathrm{s}}^{48\,\mathrm{h}} N_0/f$ with modeled zero-crossing depth. Over longer time-scales (> 48 h) the offshore length-scale is expected to grow due to frictional effects and continuous water-mass transformation in the TRC region. However, as incident wave conditions are not typically steady, there is potential for enhanced sub-tidal inner-shelf variability modulated by surf-zone processes. A d_{s} scaling based on barotropic TRC surf-zone to inner-shelf eddy kinetic energy flux suggests increasing wave height and directional spread also increase d_{s} (and vice-versa), subsequently modifying the offshore extent of inner-shelf response through L_{R}. Additional inner-shelf stratification and circulation variability induced by various other coastal

processes, *e.g.,* surface and internal tides, wind, non-linear internal waves and bores and surface or lateral heat fluxes, also potentially modulate the inner-shelf response to TRCs.

Acknowledgements

This work was funded under the CSIDE grant by the National Science Foundation (NSF OCE-1459389), and student funding was provided through the NSF-GRFP. This work used the Extreme Science and Engineering Discovery Environment (XSEDE) Comet at SDSC through allocation TG-OCE180014, which is supported by National Science Foundation grant number ACI-1548562. We thank Nirnimesh Kumar and Sarah N. Giddings for thoughtful insight that improved this work.

Chapter 3, in full, is currently being prepared for submission for publication of the material to Journal of Fluid Mechanics by D. J. Grimes and F. Feddersen. The dissertation author was the primary investigator and author of this paper.

Appendix A: Conceptual Model of SZ/TRC-induced Mixing and Cross-shore Deformation of Mixed Fluid

Herein we provide the derivation for the zero-crossing depth d_s and the $\mathrm{APE}_{(z,t)}(x)$ scalings for the idealized scenarios in Figure 3.14a,b used to contextualize the results. Consider a simplified alongshore (y) uniform domain with constant bathymetric slope $h = -\beta x$ extending offshore to $x = -L_x$, such that the cross-shore domain width at each z-level is given by $\mathcal{L}(z) = L_x + z/\beta$ (Figure 3.14a). The impact of surf-zone and TRC-induced eddy driven mixing on the structure of available and background potential energy are illustrated by assuming the TRC-region mixing homogenizes temperature over $x > -L_{\mathrm{mix}}$ (Figure 3.14a), with offshore depth $h_{\mathrm{mix}} = \beta L_{\mathrm{mix}}$. The well mixed fluid within area $A_{\mathrm{mix}} = \beta L_{\mathrm{mix}}^2/2$ has initial temperature $T_0(z)$ (3.1), such that homogenizing results in uniform temperature, T_{mix},

$$\begin{aligned} T_{\mathrm{mix}} &= A_{\mathrm{mix}}^{-1} \int_{-L_{\mathrm{mix}}}^{0} \int_{-h(x)}^{0} T_0(z)\, \mathrm{d}z\, \mathrm{d}x, \\ &= T_{\mathrm{ref}} - \frac{1}{3}\beta L_{\mathrm{mix}} \frac{\mathrm{d}T_0}{\mathrm{d}z}, \\ &= T_0(-d_{\mathrm{mix}}), \end{aligned} \tag{3.38}$$

where $d_{\mathrm{mix}} = \beta L_{\mathrm{mix}}/3$ is the depth where the initial $T_0(z)$ matches the well mixed fluid (denoted d_s in Figure 3.14a). The mixing depth d_{mix} is equivalent to the ΔT_s zero-crossing depth d_s, because the sorting procedure redistributes the mixed fluid about the depth where $T_{\mathrm{mix}} = T_0$ (right of Figure 3.14a). However, modifying the geometry of the well mixed region will modify the form of d_{mix}, thus symbol d_{mix} is used in lieu of d_s in the following derivations.

The sorted density and temperature profile of idealization Figure 3.14a is determined by redistributing temperature above $z = -h_{\mathrm{mix}} = -3d_{\mathrm{mix}}$ such that all isotherms are horizontal and intersect the sloping bottom (c.f. Section 3.4.2). After sorting, fluid initially within the region $x < -L_{\mathrm{mix}}$ and $-3d_{\mathrm{mix}} < z < -d_{\mathrm{mix}}$ vertically contracts to occupy $-3d_{\mathrm{mix}} < z < -d_{\mathrm{mix}}^{-}$, *i.e.,* with

$d^-_{\rm mix} > d_{\rm mix}$. The depth $d^-_{\rm mix}$ is determined by equating the initial area offshore of $x = -L_{\rm mix}$ and between $-3d_{\rm mix} < z - d_{\rm mix}$,

$$A^-_0 = 2d_{\rm mix}(L_x - L_{\rm mix}), \tag{3.39}$$

to the sorted area occupying the full cross-shore domain $\mathcal{L}(z)$ over $-3d_{\rm mix} < z < -d^-_{\rm mix}$,

$$\begin{aligned} A^-_{\rm s} &= \int_{-3d_{\rm mix}}^{-d^-_{\rm mix}} \mathcal{L}(z)\,{\rm d}z, \\ &= (3d_{\rm mix} - d^-_{\rm mix})L_x + \left[(d^-_{\rm mix})^2 - 9d^2_{\rm mix}\right](2\beta)^{-1}, \end{aligned} \tag{3.40}$$

resulting in a quadratic equation for $d^-_{\rm mix}$, with the relevant root being,

$$d^-_{\rm mix} = \beta L_x \left[1 - (1 - \varepsilon^-_\Delta)^{1/2}\right], \tag{3.41}$$

where the non-dimensional sorted layer thickness parameter,

$$\varepsilon^-_\Delta = 2\varepsilon_z + 3\varepsilon_z^2, \tag{3.42}$$

with $\varepsilon_z = d_{\rm mix}/h_{\rm max}$ (or $L_{\rm mix}/L_x = 3\varepsilon_z$) quantifying the relative size of zero-crossing depth to the maximum depth $h_{\rm max} = (\beta L_x)$. The modeled $\max\{d^{48\,{\rm h}}_{\rm s}\} = 4.3$ m suggests $\varepsilon_z < 0.04$ for the present simulations. Expanding (3.41) to $O(\varepsilon_z)$ gives,

$$d^-_{\rm mix} \sim d_{\rm mix}(1 + 2\varepsilon_z). \tag{3.43}$$

Applying the same procedure to redistribute the stratified near-surface offshore region $x < -L_{\rm mix}$ and $z > -d_{\rm mix}$ to occupy the full cross-shore domain and $z > -d^+_{\rm mix}$, gives

$$d^+_{\rm mix} = \beta L_x \left[1 - (1 - \varepsilon^+_\Delta)^{1/2}\right], \tag{3.44}$$

where,

$$\varepsilon_{\Delta}^{+} = 2\varepsilon_z - 6\varepsilon_z^2, \tag{3.45}$$

such that to $O(\varepsilon_z)$,

$$d_{\mathrm{mix}}^{+} = d_{\mathrm{mix}}\left(1 - \frac{5}{2}\varepsilon_z\right). \tag{3.46}$$

Lastly, the well-mixed region $x > -L_{\mathrm{mix}}$ spans $-d_{\mathrm{mix}}^{-} < z < -d_{\mathrm{mix}}^{+}$ after sorting. It is worth noting that the separation between ΔT_{s} extrema scales as $\Delta d_{\mathrm{mix}} = 9/2\, d_{\mathrm{mix}}\varepsilon_z$, or $\approx 0.18\, d_{\mathrm{mix}}$, roughly $1/4$ the modeled separation $\Delta d_{\mathrm{s}}^{48\mathrm{h}} \approx 0.75\, d_{\mathrm{s}}^{48\mathrm{h}}$.

Following the sorting procedure isotherms within the stratified regions are compressed. The sorted temperature profile for upper and lower sections are derived by matching $T_{\mathrm{s}}(0) = T_0(0)$ and $T_{\mathrm{s}}(-3d_{\mathrm{mix}}) = T_0(-3d_{\mathrm{mix}})$ and conserving area between initial and sorted isotherms. At $z = \{-3d_{\mathrm{mix}}, 0\}$, the conservation of area between isotherms separated by,

$$\Delta T = \Delta z \frac{\mathrm{d}T_0}{\mathrm{d}z} \equiv \Delta z_{\mathrm{s}} \frac{\partial T_{\mathrm{s}}}{\partial z}, \tag{3.47}$$

requires the initial and sorted isotherm separations $\{\Delta z, \Delta z_s\}$ satisfy,

$$\Delta z_{\mathrm{s}}\, \mathcal{L}(z) = \Delta z\, (L_x - L_{\mathrm{mix}}). \tag{3.48}$$

Substituting relation (3.48) in (3.47) gives,

$$\frac{\partial T_{\mathrm{s}}}{\partial z} = \frac{\mathrm{d}T_0}{\mathrm{d}z}\, (1 + \varepsilon_z z/d_{\mathrm{mix}})\, /\, (1 - 3\varepsilon_z), \tag{3.49}$$

and T_{s} is given in the upper and lower region by integration of (3.49) with $T_{\mathrm{s}} = T_0$ at $z = 0$ and

$z = -3d_{\rm mix}$, respectively. Thus, the sorted temperature is piecewise continuous,

$$T_{\rm s} = \begin{cases} T_{\rm ref} + z(1+\varepsilon_z z/(2d_{\rm mix}))\frac{{\rm d}T_0}{{\rm d}z}(1-\varepsilon_x)^{-1} & \text{for } z > -d^+_{\rm mix}, \\ T_{\rm mix} & \text{for } -d^-_{\rm mix} < z < -d^+_{\rm mix}, \\ T_{\emptyset} + z(1+\varepsilon_z z/(2d_{\rm mix}))\frac{{\rm d}T_0}{{\rm d}z}(1-\varepsilon_x)^{-1} & \text{for } -3d_{\rm mix} < z < -d^-_{\rm mix}, \end{cases} \tag{3.50}$$

where $T_{\rm ref} = T_0(0)$ and $T_{\emptyset} = T_0(9/2\,\varepsilon_z d_{\rm mix}/(1-3\varepsilon_z))$ satisfy the matching conditions. Thus, for small $d_{\rm mix}$ or large $h_{\rm max}$ the sorted temperature profile approaches the initial condition (3.1), *i.e.,* $T_{\rm s}(z) = T_0(z)$.

Appendix B: Idealized Available Potential Energy

The specific available potential energy is determined using (3.20) by integrating from the reference level $z_{\rm s}$ to z. In the well-mixed region $x > -L_{\rm mix}$, the sorted reference depth $z_{\rm s} = -d^{\pm}_{\rm mix}$ and the displacement distance $|z - z_{\rm s}|$ is linear. For $z > -d^+_{\rm mix}$,

$$\begin{aligned} {\rm ape}^+(z) &= \rho N_0^2 d_{\rm mix} \int_{-d_{\rm mix}}^{z} \left[1 + \left(\frac{z}{d_{\rm mix}}\right)\right] {\rm d}z, + O(\varepsilon_z) \\ &= \frac{1}{2}\rho N_0^2 d_{\rm mix}^2 \left[1 + \left(\frac{z}{d_{\rm mix}}\right)\right]^2 + O(\varepsilon_z), \end{aligned} \tag{3.51}$$

and is equivalent to ${\rm ape}^-(z)$ at leading order (right of Figure 3.14b). The cross-shore varying ${\rm APE}_z(x)$ is given by combining the depth integrated ${\rm ape}^{\pm}(z)$. Integrating ${\rm ape}^+$ over $z \geq -d^+_{\rm mix} \sim -d_{\rm mix}$ gives,

$$\begin{aligned} {\rm APE}^+_z(x) &= \frac{1}{2}\rho N_0^2 d_{\rm mix}^2 \int_{-\max\{d_{\rm mix}, h(x)\}}^{0} \left[1 + \left(\frac{z}{d_{\rm mix}}\right)\right]^2 {\rm d}z + O(\varepsilon_z), \\ &= \frac{1}{6}\rho N_0^2 d_{\rm mix}^3 \left[1 - \left(1 - \frac{\max\{d_{\rm mix}, h(x)\}}{d_{\rm mix}}\right)^3\right] + O(\varepsilon_z), \end{aligned} \tag{3.52}$$

and is separated into two regions at $x = -d^+_{\rm mix}/\beta$. For $x \le -d^+_{\rm mix}/\beta$, at leading order $\mathrm{APE}^+_z = \rho N_0^2 d^3_{\rm mix}/6$ is independent of x. Onshore of $x = -d^+_{\rm mix}/\beta$, $\mathrm{APE}^+_z(x)$ decreases cubicly with decreasing water depth (top of Figure 3.14b). Integrating ape^- from $z = -h(x)$ to $z = -d^-_{\rm mix} \sim -d_{\rm mix}$ gives,

$$\mathrm{APE}^-_z(x) \;=\; \frac{1}{6}\rho N_0^2 d^3_{\rm mix}\left(\frac{h(x)}{d_{\rm mix}} - 1\right)^3 + O(\varepsilon_z), \tag{3.53}$$

and APE^-_z increases cubicly with water depth. Combining the upper- and lower-layer $\mathrm{APE}^\pm_z$ gives,

$$\mathrm{APE}_z \approx \begin{cases} \frac{1}{2}\rho N_0^2 d^3_{\rm mix}\left[\left(\frac{h(x)}{d_{\rm mix}}\right) - \left(\frac{h(x)}{d_{\rm mix}}\right)^2 + \frac{1}{3}\left(\frac{h(x)}{d_{\rm mix}}\right)^3\right] & \text{for } x > -d^+_{\rm mix}/\beta, \\ \frac{1}{6}\rho N_0^2 d^3_{\rm mix} & \text{for } -d^-_{\rm mix}/\beta < x < -d^+_{\rm mix}/\beta, \\ \frac{1}{6}\rho N_0^2 d^3_{\rm mix}\left[\left(\frac{h(x)}{d_{\rm mix}}\right) - 1\right]^3 & \text{for } -3d_{\rm mix}/\beta < z < -d^-_{\rm mix}/\beta, \end{cases} \tag{3.54}$$

Thus, $\mathrm{APE}_z(x)$ varies cubicly in terms of $(-\beta x)/d_{\rm mix}$ outside of the narrow region $-d^-_{\rm mix}/\beta \le x \le -d^+_{\rm mix}/\beta$ where APE_z is constant. Offshore of the well-mixed region, $x < -L_{\rm mix}$, $\mathrm{ape}^\pm$ are $O(\varepsilon_z^2)$ implying that the offshore area integrated $\mathrm{APE}_{(x,z)}$ is $O(\varepsilon_z)$. Hereafter, we neglect the offshore region. Cross-shore integrating $\mathrm{APE}_z(x)$ gives, $\mathrm{APE}^+_{(x,z)} + \mathrm{APE}^-_{(x,z)} = \rho N_0^2 d^4_{\rm mix}/\beta[1/8 + 1/3 + 2/3] = \mathrm{PE}^{\rm mix}_{(x,z)}/2$.

To compare the idealized cross-shore varying $\mathrm{APE}_z(x)$ to the modeled $\mathrm{APE}_{(z,t)}(x, \mathrm{d}T_0/\mathrm{d}z)$, the vertical front at $x = -L_{\rm mix}$ in Figure 3.14a is transformed into sloping fronts above and below $z = -d_{\rm mix}$ in Figure 3.14b, qualitatively consistent with model sloping far-field $\langle \bar{T} \rangle$ isotherms (Figure 3.3d-f). The depth of upper and lower sloping fronts are,

$$H^\pm = d_{\rm mix} \mp \beta^\pm_{\rm f}(x + L_{\rm f}), \tag{3.55}$$

with $H^+ = H^-$ at the offshore apex located at $x = -L_{\rm f}$ (Figure 3.14b). Upper/lower frontal slopes

$\beta_f^{\pm}$ may differ from one another to satisfy dynamics or conservation relations (*e.g.,* conserve area, mean temperature, or potential energy) or enforce that surface/bottom fronts occur offshore of the TRC region ($x > -4L_{sz}$) or surf-zone ($x > -L_{sz}$). For symmetric upper/lower frontal slope β_f, the idealized intrusion has vertical thickness,

$$H(x) = H^-(x) - H^+(x) = 2\beta_f(x + L_f), \tag{3.56}$$

varying with offshore length scale L_f and the frontal slope β_f. For simplicity, the values used in Figure 3.14b were determined by constraining the offshore apex depth to $z = -d_{mix}$ while conserving the initial area $A_{mix} = (9/2)\, d_s^2/\beta_{sz}$. Thus, Figure 3.14b is an adiabatic transformation of Figure 3.14b, neglecting the adjustment of isotherms initially offshore of $x = -L_{mix}$. Alternative constraints, *e.g.,* conserving the well-mixed fluid temperature, further complexify the derivation. As the adjustment does not conserve potential energy or potential vorticity, it is only meant as a qualitative illustration of the cross-shore APE_z structure. For brevity, derivation of L_f is only summarized. Integrating over the well-mixed intrusion and wedge of Figure 3.14b and equating to A_{mix} results in the quadratic polynomial,

$$aL_f^2 + bL_f - c = 0 \tag{3.57}$$

with variable coefficients,

$$a = \beta_f^2\beta, \tag{3.58}$$

$$b = 2d_{mix}\beta_f\beta, \tag{3.59}$$

$$c = d_{mix}^2(2\beta_f + \beta) + 9d_{mix}^2\beta_f(\beta_f + \beta)/\beta, \tag{3.60}$$

and taking the positive root

$$L_f = \frac{-b + \sqrt{b^2 + 4ac}}{2a}. \tag{3.61}$$

The relevant result being that the cross-shore length scale L_f is inversely proportional to β_f, *i.e.,* smaller β_f induces larger L_f. For very small β_f enforcing conservation of area can lead to surface front intersecting the surf-zone $x = -L_\mathrm{sz}$, this may be avoided by modifying $\beta_\mathrm{f}^{\pm}$.

Based on the leading order quadratic dependence ape$^{\pm}$ (3.51), the depth integrated $\mathrm{APE}_z(x)$ (3.54) varies cubicly in $(-\beta x)/d_\mathrm{mix}$. Similarly, in the transformed configuration in Figure 3.14b the far-field region where well-mixed fluid is bounded above and below by sloping $H^{\pm}$ (offshore of triangle, Figure 3.14b), APE_z also varies cubicly. Specifically, moving offshore from $x = 0$ to the APE_z maximum, which occurs where the lower sloping front H^{-} intersects the bottom (square, Figure 3.14b), APE_z is described by (3.54). Offshore of the maximum, the depth integrated $\mathrm{APE}_z(x)$ is given by,

$$\mathrm{APE}_z \approx \begin{cases} \frac{1}{6}\rho N_0^2 d_\mathrm{mix}^3 \left[1 + \left(\frac{\beta_\mathrm{f}}{d_\mathrm{mix}}\right)^3 (x + L_\mathrm{f})^3\right] & \text{for } \triangle < x < \square, \\ \frac{1}{3}\rho N_0^2 d_\mathrm{mix}^3 \left(\frac{\beta_\mathrm{f}}{d_\mathrm{mix}}\right)^3 (x + L_\mathrm{f})^3 & \text{for } x < \triangle, \end{cases} \tag{3.62}$$

where x ranges correspond to markers in Figure 3.14b. For $x < \triangle$, shifting the origin to the surface front at $x = \triangle = x_0$, where $(x + L_\mathrm{f}) = (x - x_0 + d_\mathrm{mix}/\beta_\mathrm{f})$, and substituting $\beta_\mathrm{f} = d_\mathrm{mix}/L_\mathrm{R} \approx f/N_0$ gives a far-field scaling,

$$\mathrm{APE}_z^{\mathrm{ff}}(x) = \frac{1}{3}\rho N_0^2 d_\mathrm{mix}^3 \left[1 + L_\mathrm{R}^{-1}(x - x_0)\right]^3. \tag{3.63}$$

Appendix C: Idealized Background Potential Energy

As the sorted temperature anomaly depends on the magnitude of ε_z, the idealized background potential energy change associated with the idealizations in Figure 3.14a must also depend on relative size of the zero-crossing depth d_mix to the full cross-shore domain L_x. Here, the change in background potential energy is derived based on (3.19) and (3.50). The vertical distribution of

specific background potential energy change is piece-wise continuous with,

$$\Delta\text{bpe}(z) = \begin{cases} -\rho N_0^2 \mathrm{C}_\varepsilon z^2 \left[1 + z/(6d_{\text{mix}})\right] & \text{for } z > -d_{\text{mix}}^+, \\ \rho N_0^2 z(z + d_{\text{mix}}) & \text{for } -d_{\text{mix}}^- < z < -d_{\text{mix}}^+, \\ -\rho N_0^2 \mathrm{C}_\varepsilon z \left[\frac{3}{2} d_{\text{mix}} + z(1 + z/(6d_{\text{mix}}))\right] & \text{for } -3d_{\text{mix}} < z < d_{\text{mix}}^-, \end{cases} \tag{3.64}$$

where $\mathrm{C}_\varepsilon = 3\varepsilon_z/(1-3\varepsilon_z)$. Although the upper and lower region Δbpe are $O(\varepsilon_z)$ the area integrated change is $O(1)$. The leading order $z > -d_{\text{mix}}^+$ area integrated Δbpe is,

$$\begin{aligned} \text{BPE}_{(x,z)}^+ &= -\rho N_0^2 (3\varepsilon_z L_x) d_{\text{mix}}^2 \int_{-d_{\text{mix}}}^0 \left[\left(\frac{z}{d_{\text{mix}}}\right)^2 + \frac{1}{6}\left(\frac{z}{d_{\text{mix}}}\right)^3 \right] \mathrm{d}z + O(\varepsilon_z), \\ &= -\frac{7}{24} \rho N_0^2 L_{\text{mix}} d_{\text{mix}}^3 + O(\varepsilon_z), \end{aligned} \tag{3.65}$$

where the substitution $L_{\text{mix}} = 3\varepsilon_z L_x$ was made from line 1-2. The negative sign indicates that the sorted background potential energy is more-negative than the initial potential energy, *i.e.,* denser fluid at same z-level relative to initial density profile. To leading order in the lower region,

$$\begin{aligned} \text{BPE}_{(x,z)}^- &= -\rho N_0^2 L_{\text{mix}} d_{\text{mix}}^2 \int_{-3d_{\text{mix}}}^{-d_{\text{mix}}} \left[\frac{3}{2}\left(\frac{z}{d_{\text{mix}}}\right) + \left(\frac{z}{d_{\text{mix}}}\right)^2 + \frac{1}{6}\left(\frac{z}{d_{\text{mix}}}\right)^3 \right] \mathrm{d}z + O(\varepsilon_z), \\ &= \frac{2}{3} \rho N_0^2 L_{\text{mix}} d_{\text{mix}}^3 + O(\varepsilon_z), \end{aligned} \tag{3.66}$$

and is > 0 due to a deepening in the sorted isotherms, *i.e.,* lighter water at depth. Over the unstratified region $-d_{\text{mix}}^- < z < -d_{\text{mix}}^+$, $\text{BPE}_{(x,z)}$ is $O(\varepsilon_z)$ and tends to zero with increasing L_x. Thus, for relatively large domain, the total change is $\text{BPE}_{(x,z)} = \text{PE}_{(x,z)}^{\text{mix}}/2$ and potential energy change is equipartitioned between background and available constituents.

Bibliography

Austin, J. A. and Lentz, S. J. (2002). The inner shelf response to wind-driven upwelling and downwelling. *Journal of Physical Oceanography*, 32(7):2171–2193.

Barbier, E. B., Hacker, S. D., Kennedy, C., Koch, E. W., Stier, A. C., and Silliman, B. R. (2011). The value of estuarine and coastal ecosystem services. *Ecological Monographs*, 81(2):169–193.

Boehm, A. B., Ismail, N. S., Sassoubre, L. M., and Andruszkiewicz, E. A. (2017). Oceans in peril: Grand challenges in applied water quality research for the 21st century. *Environmental Engineering Science*, 34(1):3–15.

Bolster, D., Hang, A., and Linden, P. F. (2008). The front speed of intrusions into a continuously stratified medium. *Journal of Fluid Mechanics*, 594:369377.

Booij, N., Ris, R. C., and Holthuijsen, L. H. (1999). A third-generation wave model for coastal regions: 1. model description and validation. *Journal of Geophysical Research: Oceans*, 104(C4):7649–7666.

Bowen, A. J. (1969). Rip currents: 1. theoretical investigations. *Journal of Geophysical Research*, 74(23):5467–5478.

Brink, K. (2016). Cross-shelf exchange. *Annual Review of Marine Science*, 8(1):59–78. PMID: 26747520.

Brown, J., MacMahan, J., Reniers, A., and Thornton, E. (2009). Surf zone diffusivity on a rip-channeled beach. *Journal of Geophysical Research: Oceans*, 114(C11).

Brown, J. A., MacMahan, J. H., Reniers, A. J. H. M., and Thornton, E. B. (2015). Field observations of surf zone-inner shelf exchange on a rip-channeled beach. *Journal of Physical Oceanography*, 45(9):2339–2355.

Burchard, H. and Bolding, K. (2001). Comparative analysis of four second-moment turbulence closure models for the oceanic mixed layer. *Journal of Physical Oceanography*, 31(8):1943–1968.

Castelao, R., Chant, R., Glenn, S., and Schofield, O. (2010). The Effects of Tides and Oscillatory Winds on the Subtidal Inner-Shelf Cross-Shelf Circulation. *Journal of Physical Oceanography*, 40(4):775–788.

Castelle, B. and Coco, G. (2013). Surf zone flushing on embayed beaches. *Geophysical Research Letters*, 40(10):2206–2210.

Castelle, B., Scott, T., Brander, R., and McCarroll, R. (2016). Rip current types, circulation and hazard. *Earth-Science Reviews*, 163:1 – 21.

Clark, D. B., Elgar, S., and Raubenheimer, B. (2012). Vorticity generation by short-crested wave breaking. *Geophysical Research Letters*, 39(24).

Clark, D. B., Feddersen, F., and Guza, R. T. (2010). Cross-shore surfzone tracer dispersion in an alongshore current. *Journal of Geophysical Research: Oceans*, 115(C10). C10035.

Clark, D. B., Feddersen, F., and Guza, R. T. (2011). Modeling surf zone tracer plumes: 2. transport and dispersion. *Journal of Geophysical Research: Oceans*, 116(C11). C11028.

Clark, D. B., Lenain, L., Feddersen, F., Boss, E., and Guza, R. T. (2014). Aerial imaging of fluorescent dye in the near shore. *Journal of Atmospheric and Oceanic Technology*, 31(6):1410–1421.

Dalrymple, R. A., MacMahan, J. H., Reniers, A. J., and Nelko, V. (2011). Rip currents. *Annual Review of Fluid Mechanics*, 43(1):551–581.

Davis, K., Lentz, S., Pineda, J., Farrar, J., Starczak, V., and Churchill, J. (2011). Observations of the thermal environment on red sea platform reefs: A heat budget analysis. *Coral Reefs*, 30:25–36.

Elgar, S. and Raubenheimer, B. (2020). Field Evidence of Inverse Energy Cascades in the Surfzone. *Journal of Physical Oceanography*, 50(8):2315–2321.

Elgar, S., Raubenheimer, B., Clark, D. B., and Moulton, M. (2019). Extremely low frequency (0.1 to 1.0 mhz) surf zone currents. *Geophysical Research Letters*, 46(3):1531–1536.

Farrar, J. T., Zappa, C. J., Weller, R. A., and Jessup, A. T. (2007). Sea surface temperature signatures of oceanic internal waves in low winds. *Journal of Geophysical Research: Oceans*, 112(C6).

Farrow, D. E. (2013). Periodically driven circulation near the shore of a lake. *Environmental Fluid Mechanics*, 13(3):243–255.

Farrow, D. E. (2016). A numerical model of periodically forced circulation near the shore of a lake. *Environmental Fluid Mechanics*, 16(5):983–995.

Farrow, D. E. and Patterson, J. C. (1993). On the response of a reservior sidearm to diurnal heating and cooling. *J. Fluid Mech.*, 246:143–161.

Feddersen, F. (2007). Breaking wave induced cross-shore tracer dispersion in the surf zone: Model results and scalings. *Journal of Geophysical Research: Oceans*, 112(C9).

Feddersen, F. (2012). Scaling surf zone turbulence. *Geophysical Research Letters*, 39(18). L18613.

Feddersen, F. (2014). The generation of surfzone eddies in a strong alongshore current. *Journal of Physical Oceanography*, 44(2):600–617.

Feddersen, F. and Guza, R. T. (2003). Observations of nearshore circulation: Alongshore uniformity. *Journal of Geophysical Research: Oceans*, 108(C1):6–1–6–10.

Feddersen, F., Olabarrieta, M., Guza, R. T., Winters, D., Raubenheimer, B., and Elgar, S. (2016). Observations and modeling of a tidal inlet dye tracer plume. *Journal of Geophysical Research: Oceans*.

Feddersen, F. and Trowbridge, J. H. (2005). The effect of wave breaking on surf-zone turbulence and alongshore currents: A modeling study. *Journal of Physical Oceanography*, 35(11):2187–2203.

Fong, D. A. and Stacey, M. T. (2003). Horizontal dispersion of a near-bed coastal plume. *J. Fluid Mech.*, 489:239–267.

Garrett, C. J. and Loder, J. W. (1981). Dynamical aspects of shallow sea fronts. *Philosophical Transactions of the Royal Society of London.*, A302:563–581.

Grant, S. B., Kim, J. H., Jones, B. H., Jenkins, S. A., Wasyl, J., and Cudaback, C. (2005). Surf zone entrainment, along-shore transport, and human health implications of pollution from tidal outlets. *J. Geophys. Res.*, 110(C10025):doi:10.1029/2004JC002401.

Grimes, D. J., Feddersen, F., Giddings, S. N., and Pawlak, G. (2020a). Cross-shore deformation of a surfzone-released dye plume by an internal tide on the inner shelf. *Journal of Physical Oceanography*, 50(1):35–54.

Grimes, D. J., Feddersen, F., and Kumar, N. (2020b). Data from: Tracer exchange across the stratified inner-shelf driven by transient rip-currents and diurnal surface heat fluxes. In Transient Rip-Currents on the Stratified Inner-shelf. UC San Diego Library Digital Collections.

Grimes, D. J., Feddersen, F., and Kumar, N. (2020c). Tracer exchange across the stratified inner-shelf driven by transient rip-currents and diurnal surface heat fluxes. *Geophysical Research Letters*, 47(10):e2019GL086501. e2019GL086501 10.1029/2019GL086501.

Grimshaw, R., Pelinovsky, E., Talipova, T., and Kurkin, A. (2004). Simulation of the transformation of internal solitary waves on oceanic shelves. *Journal of Physical Oceanography*, 34(12):2774–2791.

Hally-Rosendahl, K., Feddersen, F., Clark, D. B., and Guza, R. T. (2015). Surfzone to inner-shelf exchange estimated from dye tracer balances. *Journal of Geophysical Research: Oceans*, 120(9):6289–6308.

Hally-Rosendahl, K., Feddersen, F., and Guza, R. T. (2014). Cross-shore tracer exchange between the surfzone and inner-shelf. *Journal of Geophysical Research: Oceans*, 119(7):4367–4388.

Hench, J. L., Leichter, J. J., and Monismith, S. G. (2008). Episodic circulation and exchange in a wave-driven coral reef and lagoon system. *Limnology and Oceanography*, 53(6):2681–2694.

Hendershott, M. (1981). *Long waves and ocean tides. In "Evolution of Physical Oceanography" (B.A. Warren and C. Wunsch, eds.)*, chapter 10, pages 292–341. MIT Press, Cambridge, Mass.

Henderson, S. M. (2016). Upslope internal-wave Stokes drift, and compensating downslope eulerian mean currents, observed above a lakebed. *Journal of Physical Oceanography*, 46(6):1947–1961.

Herdman, L. M. M., Hench, J. L., and Monismith, S. G. (2015). Heat balances and thermally driven lagoon-ocean exchangeson a tropical coral reef system (moorea, french polynesia). *Journal of Geophysical Research: Oceans*, 120(2):1233–1252.

Holloway, P. E., Pelinovsky, E., and Talipova, T. (1999). A generalized Korteweg-de Vries model of internal tide transformation in the coastal zone. *Journal of Geophysical Research: Oceans*, 104(C8):18333–18350.

Horwitz, R. and Lentz, S. J. (2014). Inner-shelf response to cross-shelf wind stress: The importance of the cross-shelf density gradient in an idealized numerical model and field observations. *Journal of Physical Oceanography*, 44(1):86–103.

Johnson, D. and Pattiaratchi, C. (2004). Transient rip currents and nearshore circulation on a swell-dominated beach. *Journal of Geophysical Research: Oceans*, 109(C2).

Johnson, D. and Pattiaratchi, C. (2006). Boussinesq modelling of transient rip currents. *Coastal Engineering*, 53(5):419 – 439.

Jones, N. L., Lowe, R. J., Pawlak, G., Fong, D. A., and Monismith, S. G. (2008). Plume dispersion on a fringing coral reef system. *Limnology and Oceanography*, 53(5part2):2273–2286.

Kantha, L. H. and Clayson, C. A. (1994). An improved mixed layer model for geophysical applications. *Journal of Geophysical Research: Oceans*, 99(C12):25235–25266.

Klymak, J. M. and Moum, J. N. (2003). Internal solitary waves of elevation advancing on a shoaling shelf. *Geophysical Research Letters*, 30(20).

Kumar, N. and Feddersen, F. (2017a). The effect of Stokes drift and transient rip currents on the inner shelf. part i: No stratification. *Journal of Physical Oceanography*, 47(1).

Kumar, N. and Feddersen, F. (2017b). The effect of Stokes drift and transient rip currents on the inner shelf. part ii: With stratification. *Journal of Physical Oceanography*, 47(1):243–260.

Kumar, N. and Feddersen, F. (2017c). A new offshore transport mechanism for shoreline-released tracer induced by transient rip currents and stratification. *Geophys. Res. Lett.*, 44.

Kumar, N., Feddersen, F., Suanda, S., Uchiyama, Y., and McWilliams, J. (2016). Mid- to inner-shelf coupled ROMS-SWAN model-data comparison of currents and temperature: Diurnal and semi-diurnal variability. *J. Phys. Ocean.*

Kumar, N., Voulgaris, G., Warner, J. C., and Olabarrieta, M. (2012). Implementation of the vortex force formalism in the coupled ocean-atmosphere-wave-sediment transport (coawst) modeling system for inner shelf and surf zone applications. *Ocean Modelling*, 47:65–95.

Lamb, K. G. (1997). Particle transport by nonbreaking, solitary internal waves. *Journal of Geophysical Research: Oceans*, 102(C8):18641–18660.

Lei, C. and Patterson, J. C. (2002). Unsteady natural convection in a triangular enclosure induced by absorption of radiation. *Journal of Fluid Mechanics*, 460:181209.

Lemagie, E. P. and Lerczak, J. A. (2015). A comparison of bulk estuarine turnover timescales to particle tracking timescales using a model of the yaquina bay estuary. *Estuaries and Coasts*, 38(5):1797–1814.

Lentz, S. J. (2001). The influence of stratification on the wind-driven cross-shelf circulation over the North Carolina shelf. *Journal of Physical Oceanography*, 31(9):2749–2760.

Lentz, S. J. and Chapman, D. C. (2004). The Importance of Nonlinear Cross-Shelf Momentum Flux during Wind-Driven Coastal Upwelling*. *Journal of Physical Oceanography*, 34(11):2444–2457.

Lentz, S. J., Fewings, M., Howd, P., Fredericks, J., and Hathaway, K. (2008). Observations and a Model of Undertow over the Inner Continental Shelf. *Journal of Physical Oceanography*, 38(11):2341–2357.

Lentz, S. J. and Fewings, M. R. (2012). The wind- and wave-driven inner-shelf circulation. *Annual Review of Marine Science*, 4(1):317–343. PMID: 22457978.

Lerczak, J. A., Geyer, W. R., and Chant, R. J. (2006). Mechanisms driving the time-dependent salt flux in a partially stratified estuary. *Journal of Physical Oceanography*, 36(12):2296–2311.

Lerczak, J. A., Hendershott, M. C., and Winant, C. D. (2001). Observations and modeling of coastal internal waves driven by a diurnal sea breeze. *Journal of Geophysical Research: Oceans*, 106(C9):19715–19729.

Longuet-Higgins, M. S. (1970a). Longshore currents generated by obliquely incident sea waves: 1. *Journal of Geophysical Research*, 75(33):6778–6789.

Longuet-Higgins, M. S. (1970b). Longshore currents generated by obliquely incident sea waves: 2. *Journal of Geophysical Research*, 75(33):6790–6801.

Lucas, A. J., Franks, P. J. S., and Dupont, C. L. (2011). Horizontal internal-tide fluxes support elevated phytoplankton productivity over the inner continental shelf. *Limnology and Oceanography: Fluids and Environments*, 1(1):56–74.

MacCready, P. (2011). Calculating estuarine exchange flow using isohaline coordinates. *Journal of Physical Oceanography*, 41(6):1116–1124.

MacCready, P. and Giddings, S. N. (2016). The mechanical energy budget of a regional ocean model. *Journal of Physical Oceanography*, 46(9):2719–2733.

MacMahan, J., Brown, J., Brown, J., Thornton, E., Reniers, A., Stanton, T., Henriquez, M., Gallagher, E., Morrison, J., Austin, M. J., Scott, T. M., and Senechal", N. (2010). Mean lagrangian flow behavior on an open coast rip-channeled beach: A new perspective. *Marine Geology*, 268(1):1 – 15.

MacMahan, J., Thornton, E., Koscinski, J., and Wang, Q. (2018). Field observations and modeling of surfzone sensible heat flux. *Journal of Applied Meteorology and Climatology*, 57(6):1371–1383.

Mao, Y. (2019). Nearshore natural convection induced by a periodic thermal forcing at the water surface. *Physics of Fluids*, 31(8):086604.

Marmorino, G. O., Smith, G. B., and Lindemann, G. J. (2004). Infrared imagery of ocean internal waves. *Geophysical Research Letters*, 31(11).

Melville, W. K., Lenain, L., Cayan, D. R., Kahru, M., Kleissl, J. P., Linden, P. F., and Statom, N. M. (2016). The modular aerial sensing system. *Journal of Atmospheric and Oceanic Technology*, 33(6):1169–1184.

Molina, L., Pawlak, G., Wells, J. R., Monismith, S. G., and Merrifield, M. A. (2014). Diurnal cross-shore thermal exchange on a tropical forereef. *Journal of Geophysical Research: Oceans*, 119(9):6101–6120.

Monismith, S. G., Genin, A., Reidenbach, M. A., Yahel, G., and Koseff, J. R. (2006). Thermally driven exchanges between a coral reef and the adjoining ocean. *Journal of Physical Oceanography*, 36(7):1332–1347.

Monismith, S. G., Imberger, J., and Morison, M. L. (1990). Convective motions in the sidearm of a small reservior. *Limnol. Oceanogr.*, 37:1676–1702.

Moniz, R. J., Fong, D. A., Woodson, C. B., Willis, S. K., Stacey, M. T., and Monismith, S. G. (2014). Scale-dependent dispersion within the stratified interior on the shelf of northern monterey bay. *Journal of Physical Oceanography*, 44(4):1049–1064.

Morgan, S. G., Shanks, A. L., MacMahan, J. H., Reniers, A. J., and Feddersen, F. (2018). Planktonic subsidies to surf-zone and intertidal communities. *Annual Review of Marine Science*, 10(1):null. PMID: 28846492.

Nam, S. and Send, U. (2011). Direct evidence of deep water intrusions onto the continental shelf via surging internal tides. *Journal of Geophysical Research: Oceans*, 116(C5).

Omand, M. M., Leichter, J. J., Franks, P. J. S., Guza, R. T., Lucas, A. J., and Feddersen, F. (2011). Physical and biological processes underlying the sudden surface appearance of a red tide in the nearshore. *Limnology and Oceanography*, 56(3):787–801.

Paulson, C. A. and Simpson, J. J. (1977). Irradiance measurements in the upper ocean. *Journal of Physical Oceanography*, 7(6):952–956.

Pedlosky, J. (1978). A nonlinear model of the onset of upwelling. *Journal of Physical Oceanography*, 8(2):178–187.

Peregrine, D. (1998). Surf zone currents. *Theoretical and Computational Fluid Dynamics*, 10(1):295–309.

Pineda, J. (1999). Circulation and larval distribution in internal tidal bore warm fronts. *Limnology and Oceanography*, 44(6):1400–1414.

Pineda, J., Hare, J. A., and Sponaugle, S. (2007). Larval transport and dispersal in the coastal ocean and consequences for population connectivity. *Oceanography*, 20.

Rainville, L. and Pinkel, R. (2001). Wirewalker: An autonomous wave-powered vertical profiler. *Journal of Atmospheric and Oceanic Technology*, 18(6):1048–1051.

Reniers, A. J. H. M., MacMahan, J. H., Beron-Vera, F. J., and Olascoaga, M. J. (2010). Rip-current pulses tied to lagrangian coherent structures. *Geophysical Research Letters*, 37(5).

Rodriguez, A. R., Giddings, S. N., and Kumar, N. (2018). Impacts of nearshore wave-current interaction on transport and mixing of small-scale buoyant plumes. *Geophysical Research Letters*, 45(16):8379–8389.

Shchepetkin, A. F. and McWilliams, J. C. (2005). The regional oceanic modeling system (roms): a split-explicit, free-surface, topography-following-coordinate oceanic model. *Ocean Modelling*, 9(4):347–404.

Shroyer, E. L., Moum, J. N., and Nash, J. D. (2010). Vertical heat flux and lateral mass transport in nonlinear internal waves. *Geophysical Research Letters*, 37(8).

Sinnett, G. and Feddersen, F. (2018). The competing effects of breaking waves on surfzone heat fluxes: Albedo versus wave heating. *Journal of Geophysical Research: Oceans*, 123.

Sinnett, G., Feddersen, F., Lucas, A. J., Pawlak, G., and Terrill, E. (2018). Observations of nonlinear internal wave run-up to the surfzone. *Journal of Physical Oceanography*, 48(3):531–554.

Smith, J. A. and Largier, J. L. (1995). Observations of nearshore circulation: Rip currents. *Journal of Geophysical Research: Oceans*, 100(C6):10967–10975.

Smith, R. L. (1981). *A Comparison of the Structure and Variability of the Flow Field in three Coastal Upwelling Regions: Oregon, Northwest Africa, and Peru*, pages 107–118. American Geophysical Union (AGU).

Spydell, M. S., Feddersen, F., and Suanda, S. (2019). Inhomogeneous turbulent dispersion across the nearshore induced by surfzone eddies. *Journal of Physical Oceanography*, 49(4):1015–1034.

Stacey, M. T., Cowen, E. A., Powell, T. M., Dobbins, E., Monismith, S. G., and Koseff, J. R. (2000). Plume dispersion in a stratified, near-coastal flow: measurements and modeling. *Continental Shelf Research*, 20(6):637 – 663.

Suanda, S. H. and Feddersen, F. (2015). A self-similar scaling for cross-shelf exchange driven by transient rip currents. *Geophysical Research Letters*, 42(13):5427–5434. 2015GL063944.

Suanda, S. H., Feddersen, F., and Kumar, N. (2017). The effect of barotropic and baroclinic tides on coastal stratification and mixing. *Journal of Geophysical Research: Oceans*, 122(12):10156–10173.

Sundermeyer, M. A. and Ledwell, J. R. (2001). Lateral dispersion over the continental shelf: Analysis of dye release experiments. *Journal of Geophysical Research: Oceans*, 106(C5):9603–9621.

Sutherland, B. R., Barrett, K. J., and Ivey, G. N. (2013). Shoaling internal solitary waves. *J. Geophys. Res.*, 118:4111–4124.

Thomas, P. J. and Linden, P. F. (2007). Rotating gravity currents: small-scale and large-scale laboratory experiments and a geostrophic model. *Journal of Fluid Mechanics*, 578:3565.

Thorpe, S. A. (1999). The generation of alongslope currents by breaking internal waves. *Journal of Physical Oceanography*, 29(1):29–38.

Ulloa, H. N., Davis, K. A., Monismith, S. G., and Pawlak, G. (2018). Temporal variability in thermally driven cross-shore exchange: The role of semidiurnal tides. *Journal of Physical Oceanography*, 48(7):1513–1531.

van Heijst, G. (1986). On the dynamics of a tidal mixing front. In Nihoul, J., editor, *Marine Interfaces Ecohydrodynamics*, volume 42 of *Elsevier Oceanography Series*, pages 165 – 194. Elsevier.

Walsh, E. J., Pinkel, R., Hagan, D. E., Weller, R. A., Fairall, C. W., Rogers, D. P., Burns, S. P., and Baumgartner, M. (1998). Coupling of internal waves on the main thermocline to the diurnal surface layer and sea surface temperature during the tropical ocean-global atmosphere coupled ocean-atmosphere response experiment. *Journal of Geophysical Research: Oceans*, 103(C6):12613–12628.

Walter, R. K., Reid, E. C., Davis, K. A., Armenta, K. J., Merhoff, K., and Nidzieko, N. J. (2017). Local diurnal wind-driven variability and upwelling in a small coastal embayment. *Journal of Geophysical Research: Oceans*, 122(2):955–972.

Walter, R. K., Woodson, C. B., Arthur, R. S., Fringer, O. B., and Monismith, S. G. (2012). Nearshore internal bores and turbulent mixing in southern monterey bay. *Journal of Geophysical Research: Oceans*, 117(C7). C07017.

Warner, J. C., Armstrong, B., He, R., and Zambon, J. B. (2010). Development of a coupled ocean–atmosphere–wave–sediment transport (COAWST) modeling system. *Ocean Modelling*, 35(3):230–244.

Warner, J. C., Geyer, W. R., and Lerczak, J. A. (2005). Numerical modeling of an estuary: A comprehensive skill assessment. *Journal of Geophysical Research: Oceans*, 110(C5).

Washburn, L. and McPhee-Shaw, E. (2013). Coastal transport processes affecting inner-shelf ecosystems in the california current system. *Oceanography*, 26(3):34–43.

White, B. L. and Helfrich, K. R. (2008). Gravity currents and internal waves in a stratified fluid. *Journal of Fluid Mechanics*, 616:327356.

Winant, C. D. (1974). Internal surges in coastal waters. *Journal of Geophysical Research*, 79(30):4523–4526.

Winters, K. B. and Barkan, R. (2013). Available potential energy density for boussinesq fluid flow. *Journal of Fluid Mechanics*, 714:476488.

Winters, K. B., Lombard, P. N., Riley, J. J., and D'Asaro, E. A. (1995). Available potential energy and mixing in density-stratified fluids. *Journal of Fluid Mechanics*, 289:115128.

Wunsch, C. (1971). Note on some reynolds stress effects of internal waves on slopes. *Deep Sea Research and Oceanographic Abstracts*, 18(6):583 – 591.

Zhang, S., Alford, M. H., and Mickett, J. B. (2015). Characteristics, generation and mass transport of nonlinear internal waves on the washington continental shelf. *Journal of Geophysical Research: Oceans*, 120(2):741–758.

Zikanov, O. and Slinn, D. N. (2001). Along-slope current generation by obliquely incident internal waves. *Journal of Fluid Mechanics*, 445:235261.